ENDOSCOPE DESIGN FOR VOLUME HOLOGRAPHIC IMAGING

by

Isela D. Howlett

A Dissertation Submitted to the Faculty of the

COLLEGE OF OPTICAL SCIENCES

In Partial Fulfillment of the Requirements
For the Degree of

DOCTOR OF PHILOSOPHY

In the Graduate College

THE UNIVERSITY OF ARIZONA

2017

THE UNIVERSITY OF ARIZONA
GRADUATE COLLEGE

As members of the Dissertation Committee, we certify that we have read the dissertation prepared by Isela D. Howlett, titled *Endoscope Design for Volume Holographic Imaging* and recommend that it be accepted as fulfilling the dissertation requirement for the Degree of Doctor of Philosophy.

_____ Date: JULY 06, 2017
RAYMOND K. KOSTUK

_____ Date: JULY 06, 2017
JENNIFER K. BARTON

_____ Date: JULY 06, 2017
TOM MILSTER

Final approval and acceptance of this dissertation is contingent upon the candidate's submission of the final copies of the dissertation to the graduate college.

I hereby certify that I have read this dissertation prepared under my direction and recommend that it be accepted as fulfilling the dissertation requirement.

_____ Date: JULY 06, 2017
DISSERTATION DIRECTOR: RAYMOND K. KOSTUK

STATEMENT BY AUTHOR

This dissertation has been submitted in partial fulfillment of the requirements for an advanced degree at the University of Arizona and is deposited in the University Library to be made available to borrowers under rules of the Library.

Brief quotations from this dissertation are allowable without special permission, provided that an accurate acknowledgement of the source is made. Requests for permission for extended quotation from or reproduction of this manuscript in whole or in part may be granted by the head of the major department or the Dean of the Graduate College when in his or her judgment the proposed use of the material is in the interests of scholarship. In all other instances, however, permission must be obtained from the author.

SIGNED: ISELA D. HOWLETT

ACKNOWLEDGEMENTS

I would like to thank Dr. Raymond Kostuk, my adviser, for assisting my through my time as a PhD candidate. He provided guidance during a time when almost all paths seemed to go dark and supported me through the final stages of my research. I am appreciative of all of Ray's assistance and teaching over the past five years.

I also thank my dissertation committee members, Dr. Jennifer K. Barton and Dr. Tom Milster for their assistance and feedback during the final stretch of my research.

I would like to acknowledge the funding sources which have helped to make my graduate career possible: the Sloan Minority PhD fellowship, the NSF Bridge to the Doctorate fellowship, and the UA-NASA Space Grant fellowship.

Many thanks go to the current and past students of the Photonic Systems Laboratory. Dr. Juan M. Russo: thank you for always being a listening ear and helping to point me back in the right direction. Yuechen Wu, Silvana Ayala Pelaez, Shelby Vorndran, Michael Gordon, Wanglei Han, and Benjamin Chrysler: Although some days were crazier than others, and sometimes there wasn't much communication over the cubicle walls, I appreciated our research discussions, rants, raves, and encouragement.

I thank my fellow graduate students for their friendship and support throughout my time at the College of Optical Sciences. I specifically want to recognize Kelsey Miller, Alicia Swain, and Emily Finan for being there while I studied for the written prelim and supporting my efforts through coffee and tea refueling.

I thank my sister, Iris C. Howlett, for encouraging me and sometimes putting my back into my place. You were the first Howlett PhD, now we will have a second.

Finally, I thank my husband, Christopher M. Shanor, for keeping me positive, being there during all the hard times, and reminding me that together we would get through it all.

DEDICATION

For my parents, Garlin and Christine Howlett, who have always been there and encouraged me to keep learning, keep dreaming, and never give up.

TABLE OF CONTENTS

LIST OF TABLES

LIST OF FIGURES

ABSTRACT

Early stage detection of cancerous tissue is critical to increasing the 5-year survival rate for patients. The development of devices capable of accessing and visualizing these tissue sites plays an important role in this process. Many cancer types have existing screening methods however many have proven ineffective in large clinical trials. Since early stages of cancer development often has subtle changes from normal tissue, traditional non-invasive imaging techniques such as ultrasound or magnetic resonance imaging are not able to detect them. The following work evaluates the feasibility of miniaturization of Volume Holographic Imaging (VHI) systems into laparoscopic endoscopes for tissue and cancer screening.

The work is divided into two main sections discussing the design and evaluation of each imaging system. The first system is a Reflectance VHI Endoscope designed for simultaneous imaging of two imaging depths within a tissue sample. The system is evaluated for resolution and contrast through imaging of resolution bar targets and soft tissue samples. The second system is a Wavelength Coded VHI Endoscope which combines the Reflectance VHI Endoscope imaging properties with axial chromatic dispersion effects of Gradient Index (GRIN) optics to improve the volume holographic element performance and reduce excess background light. Both Reflectance and Wavelength Coded VHI systems utilize a sub-4 mm diameter rigid relay probe which has been approved for in-vivo applications.

The sub-4.4 μm/lp resolution produced by both VHI Endoscope systems and tissue depth separations of 50 μm and 100 μm for the Reflectance and Wavelength Coded designs, respectively, make VHI systems a candidate for clinical evaluation of early stage cancer development.

Chapter 1
Introduction

Microscopic imaging systems are widely used in the biological science field to provide invaluable data to researchers and scientists. Microscopes have been revolutionizing medicine since the late 16th century by allowing direct visualization of plant and animal cellular structures. Advanced imaging techniques, such as optical coherence tomography (OCT)[1] and confocal microscopy[2], have allowed for microscopy to move away from single surface imaging by capturing cellular information from a multitude of depths. These systems are capable of spatial and spectral data collection from an object giving a 4-D (x,y,z,λ) representation of an object. One particular drawback of these systems is the required use of mechanical scanning devices to gather the full 4-D data set. The development of Volume Holographic Imaging (VHI) systems has allowed for biomedical imaging without mechanical scanning components, creating a simultaneous image collection method.

1.1 Motivation

The miniaturization of imaging modalities for in-vivo use is critical for the push of early detection of cancerous tissue through pre-screening methods of high risk patients. Systems capable of having low system cost while being able to provide fast image collection times are highly sought after in the medical field. Currently OCT and Confocal imaging systems have been developed for both ex-vivo and in-vivo applications. With VHI systems demonstrating promising results during ex-vivo trials[3], miniaturization into a laparoscopic endoscope system is the next logical step towards implementing a viable clinical instrument.

The challenges of miniaturization include decreased system field of view (FOV) and the availability of small diameter optics with desired properties. Additionally, medical device safety restrictions need to be considered when selecting materials. This includes consideration of potential problems with the glasses used in lenses which may come into contact with the patient, the total light source power output, the ability for the system to pass medical device sterilization procedures, and weight limitations to keep the system handheld.

1.2 Research Objectives

In this work, a rigid laparoscopic endoscope is designed for use in VHI systems. Two design concepts are explored: a single source reflectance endoscope and a two source wavelength coded endoscope design. The objectives for these designs include:

1. Small endoscope probe size to be used with a standard 5 mm diameter laparoscopic trocar.
2. Ability to image two depths simultaneously, with the image planes of interest being separated by a minimum of 50 µm.
3. Ability to visualize cellular structure at a resolution of 2 µm, 4 µm/lp features on 2D USAF Bar Targets.

1.3 Dissertation Contributions

The contributions of this dissertation are:

1. Design, fabrication, and characterization of a reflectance VHI endoscope system utilizing a gradient index optic endoscope. The system is compatible with hydrogen peroxide

vapor sterilization procedures and passes the medical safety guidelines of the Medical Center.

2. Development and characterization of a wavelength coded VHI endoscope utilizing axial chromatic effects that are characteristic of Gradient Index optics.

Both systems are evaluated for imaging performance through system resolution measurements and imaging capabilities using USAF 1951 resolution charts and volumetric targets, such as tissue phantoms and soft tissue samples.

The research in this dissertation has resulted in the following journal and conference publications:

1. I. D. Howlett, M. Gordon, G. Orsinger, J. Brownlee, K. Hatch, M. Romanowski, J. K. Barton, and R. K. Kostuk, "Evaluation of Volume Holographic Images Obtained Through an Endoscope for in-vivo Medical Applications," in *Frontiers in Optics 2014*, OSA Technical Digest (online) (Optical Society of America, 2014), paper FTu4F.7.
2. I. D. Howlett, M. Gordon, J. W. Brownlee, J. K. Barton, and R. K. Kostuk, “Volume Holographic Reflection Endoscope for In-Vivo Ovarian Cancer Clinical Studies.” *Proceedings of SPIE* 2014 (2014): 10.1117/12.2037859. *PMC*. Web. 11 Apr. 2017.
3. I. D. Howlett, M. Gordon, G. Orsinger, J. Brownlee, M. Romanowski, J. Barton, and R. K. Kostuk, "Design and Implementation of a Volume Holographic Imaging Endoscope," in *CLEO: 2015*, OSA Technical Digest (online) (Optical Society of America, 2015), paper ATh4J.3.

4. I. D. Howlett, W. Han, J. Barton, and R. Kostuk, "Wavelength Coded Volume Holographic Imaging Endoscope Utilizing Axial Chromatic Dispersion," in *Optics in the Life Sciences Congress*, OSA Technical Digest (online) (Optical Society of America, 2017), paper BoW4A.6.
1. Isela D. Howlett, Wanglei Han, Michael Gordon, Photini Rice, Jennifer K. Barton, Raymond K. Kostuk, "Volume holographic imaging endoscopic design and construction techniques," J. Biomed. Opt. 22(5), 056010 (2017), doi: 10.1117/1.JBO.22.5.056010.
2. I. D. Howlett, W. Han, P. Rice , J. K. Barton, R. K. Kostuk, "Wavelength coded volume holographic imaging endoscope for multi-depth imaging," J. Biomed Opt Letters, Submitted July 2017

1.4 Dissertation Outline

In Chapter 2, background on illumination configurations and an introduction to benchtop Volume Holographic Imaging (VHI) system designs are discussed. Chapter 3 discusses the design and development of the reflectance VHI endoscope system. This chapter includes background discussion, system development for handle and endoscope design, fabrication, and testing. Chapter 4 introduces the wavelength coded VHI endoscope utilizing axial chromatic dispersion. Included in this chapter are background topics, a description of the chromatic effects, the design of the illumination set-up, and testing. A summary of the two systems is provided in Chapter 5. The summary will compare the two systems in terms of performance, contrast and resolution capabilities. Lastly, Chapter 6 will provide conclusion of the dissertation work.

Chapter 2
Background

2.1 Illumination Designs

Provided in this section are the types of illumination methods used in optical systems. These will be broken into general illumination systems and illumination systems typically used for microscopy.

2.1.1 Illumination Systems

The illumination set-up used in an optical system determines the type of image which can be collected. For microscopy systems, the illumination can be categorized as diffuse, critical, or specular configurations[4]. Diffuse illumination is obtained by placing a diffuser into the system so that light reaching the object will have a large angular spread allowing for greater uniformity but results in inefficient light collection. Critical illumination places the source such that the illumination optics image the source directly onto the object. This style of illumination is not desirable in cases where uniform imaging is required since any detailing of the source, such as small filaments, are superimposed onto the object causing variations in brightness. Specular illumination images the source into the entrance pupil of the objective resulting in planar illumination of the object. Specular illumination has high light efficiency and is the most commonly used arrangement for optical systems. Köhler style illumination is a form of specular illumination which places an iris diaphragm at the condenser lens to limit the illumination spot size and a second iris diaphragm at the intermediate image of the source to allow adjustment of light level.

2.1.2 Illumination for Microscopes

Illumination of an object in a microscope system can be designed for transmission imaging or reflection imaging. As the names suggest, transmission systems transmit light through a sample into the imaging optics while a reflection systems rely on the reflectivity of a sample to reflect light back into the imaging optics. Transmission microscopes primarily rely on thin samples while the thickness of a sample in reflection microscope is not critical.

Transmission style microscopes place the object between the light source and the viewing optics. Light which is transmitted is able to be collected, resulting in an image that is bright when there is low reflection and absorption in the object and dark when the object has more reflection and absorption characteristics. This set-up is not useful for in-vivo applications or the ex-vivo evaluation of thick samples.

Reflectance microscopy places the light source and viewing optics on the same side of the object, such that light which is reflected from the sample is collected by the viewing optics. This configuration is more useful for in-vivo tissue imaging. A few of the different reflectance microscopy illumination styles are Bright field, Dark field, Polarized Light, and Differential Interference Contrast (DIC) configurations[5]. In the standard reflectance microscope set-up, a bright field configuration is used. In this case, light from the source is brought into the visualization path by a beam splitter and directed through the objective, which is acting as the condenser, onto the object. Light which is reflected by the object is collected by the same objective and directed toward the imaging optics. The bright field configuration has the problem that not all objects provide enough contrast to be imaged clearly due to low index of refraction

variations in a sample. To improve contrast in reflectance microscopy dark field, polarized light, and DIC configurations are used. The dark field configuration separates the path of illumination from the visualization path. Light is directed in a ring along the outer edge of the visualization path through the objective. The light, after exiting the objective, is not perpendicular to the sample but has a higher angle of incidence. In the case of a perfect mirror, the surface will reflect no light into the visualization path. However, for an object with surface structures, light can be collected by the objective into the visualization path. The Polarized light and DIC configurations make use of polarization or phase information, respectively, from the samples to be differentiated by a set of polarization optics in the visualization path. These methods are used when an object has low contrast in a standard reflected light set-up.

In addition to the illumination configurations described above, endoscope systems can operate in many configurations based on the sample being imaged. Imaging methods range from non-contact systems which have a forward looking objective with a well-defined working distance to side viewing systems which use fold-mirrors to look 90° from a forward looking design to in-contact imaging configurations which place the sample in direct contact with the endoscope. For the specific application of this dissertation, the in-contact imaging method will be evaluated.

2.2 In-Contact Imaging

Of particular interest for volume holographic imaging development is the design of in-contact confocal endoscope systems. Confocal imaging is a high resolution optical sectioning technique used for optical biopsy[6,7]. Confocal systems typically image a point source to a point on the

sample and re-images light emitted from that point back through a pinhole aperture in front of a detector. The pinhole is placed such that light from out-of-focus positions are blocked. The system is operated in a scanning method to collect images from across a region of interest. The collection of images is later stitched in post processing to form a high resolution image map of the region. A schematic of a scanning confocal microscope is provided in Figure 2.1.

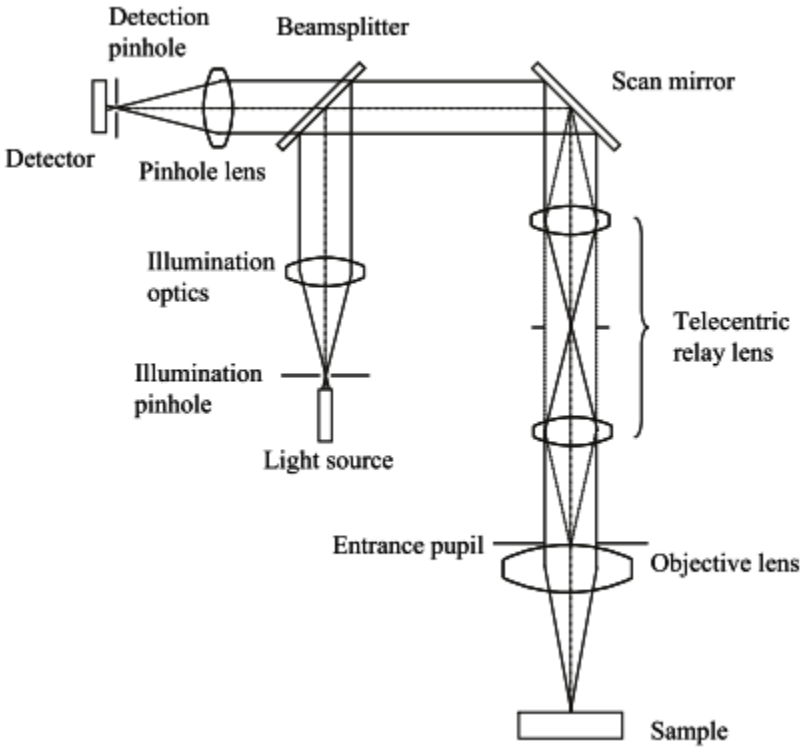

Figure 2.1: General layout of a confocal scanning microscope, as printed in Chapter 7 of Optical Design for Biomedical Imaging.[7]

The endoscopic versions of confocal systems have a desired resolution range of 1-3 μm in order to compare to pathologic inspection and diagnosis[8]. When placed in-contact with a sample, a fluorescence mode confocal system is used to increase image contrast. In fluorescence mode, a short wavelength source is used to excite fluorescence in the tissue that is stained with a dye. The fluorescence emission is at a longer wavelength and allows the short excitation

wavelength to be filtered from the imaging path of the system. This allows a common path illumination and imaging to be used in the endoscope since back reflections are eliminated.

Gradient-index (GRIN) laparoscopic endoscope[8] and slit scanning microendoscopes[9,10] designs have been reported. One of the earliest cases of a full clinical confocal microendoscope was published in 1999[9]. The clinical system was capable of in-contact sample imaging with a lateral resolution of 3 μm. This style of system is analogous to the volume holographic imaging method that is discussed in the next section.

2.3 Volume Holographic Imaging Technique

The volume holographic imaging (VHI) technique is a method of rejecting out-of-focus light from a sample through the use of a holographic filter. The holographic filter is a multiplexed volume hologram that selects light with a specific wavelength and wavefront curvature and rejects light which does not match the recorded specifications. The multiplexed volume hologram contains multiple holograms in a single optical element. Each hologram diffracts an image from a specified object depth at a different angle allowing separate depth images to be displayed on the camera plane. Multiple tissue depths are captured on the camera in real time without mechanical scanning using the multiplexed holographic optical element. Since the hologram is a dispersive element, it also disperses light along the x-axis of the image, allowing each field point to correspond to a discrete wavelength. The relative image brightness along this x-axis is proportional to the power spectral density of the light source used for illumination. Angular selectivity of holographic elements is analogous to the slit width of a slit scanning confocal microscope. The VHI method shown in Figure 2.2 allows for spatial and

spectral imaging of an object. The light collected by the objective lens will provide a planar wavefront onto the multiplexed volume hologram for an in-focus plane and a curved wavefront for an out-of-focus plane located ΔZ from the surface. The multiplexed volume hologram is recorded with two holograms, one which corresponds to the planar wavefront and one for the curved wavefront. Light with a planar wavefront will be perfectly matched to the planar hologram and rejected by the curved hologram, and vice-versa, causing the beams to diffract at different angles as selected during the recording process. The angle between the two diffracted beams is indicated in the figure as Δθ'.

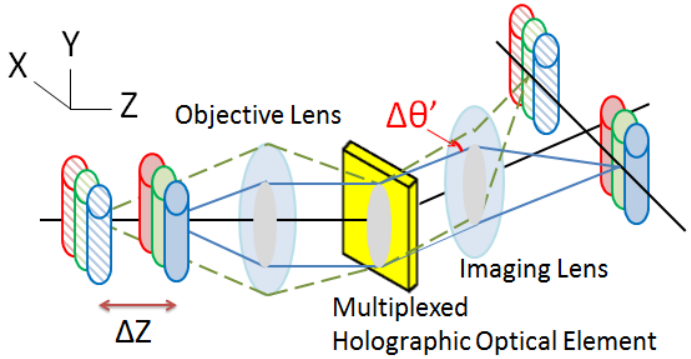

Figure 2.2: Schematic of the general VHI operation. Light from surface and depth regions are imaged by an objective lens. The wavefront of the light, in the case shown, will be planar for the surface region and curved for the depth region, since the surface is located at the focus of the objective lens. The multiplexed holographic optical element selects the specified wavefronts from the different imaging planes and diffracts the signals to the appropriate region on the camera with a given angular separation, Δθ'.

2.3.1 Hologram Design

The holograms used in the VHI systems are volume holograms. Volume holograms are used as they are capable of providing high diffraction efficiency in a single diffraction order and high angular and wavelength selectivity. Volume holograms, as described by Kogelnik, achieve these specifications through the use of a volume Q parameter with a value ≥10 ($Q = \frac{2\pi\lambda d}{n\Lambda^2}$), where Λ is the period of the volume grating, λ is the reconstruction wavelength, d is the thickness of the hologram, and n is the index of refraction[11].

The resulting holograms have high diffraction efficiency, η, in a single diffraction order and high angular and wavelength selectivity. The diffraction efficiency for volume phase transmission holograms used in the VHI system is given by

$$\eta = \frac{\sin^2\left(\nu^2+\xi^2\right)^{\frac{1}{2}}}{\left(1+\frac{\xi^2}{\nu^2}\right)} \qquad \text{Equation 1}$$

where $\nu = \frac{\pi n_1 d}{\lambda c_r c_s}; \xi = \frac{\vartheta d}{2c_s}; c_r = \cos(\theta_r)$ and $c_s = \cos(\theta_s)$[11]. In these equations the reconstruction and diffracted beam angles are represented by θ_r and θ_s, respectively. The hologram angular and wavelength selectivity are determined from the detuning parameter

$$\vartheta \approx \frac{2\pi}{\Lambda}\left[\Delta\theta \sin(\phi - \theta_o) - \frac{\Delta\lambda}{2n\Lambda}\right], \qquad \text{Equation 2}$$

calculated using the angular deviations (Δθ) and wavelength deviations (Δλ) from the hologram Bragg condition that causes the diffraction efficiency to decrease to zero. Typical angular selectivity values for the holograms are Δθ ~0.02° and the wavelength selectivity, Δλ < 0.4 nm.

The multiplexed volume holograms are fabricated through an interference process using object and reference beams, as shown in Figure 2.3. Object beams are formed by focusing a collimated beam through a microscope objective to form a point source. The microscope objective is translated a distance of Δz between each exposure, relating to the desired depth. The collimated reference beam is rotated for each exposure relative to the object beam to form a distinct grating within the multiplexed volume hologram. The angles for the object and reference beams are determined using the K-vector or Bragg matching relation: $\vec{K} = \vec{k}_{ref} - \vec{k}_{obj}$. The reference and

object propagation vectors are defined by $\vec{k}_{ref}$ and $\vec{k}_{obj}$ and the grating vector, $\vec{K}$, has a magnitude of $\frac{2\pi}{\Lambda}$.

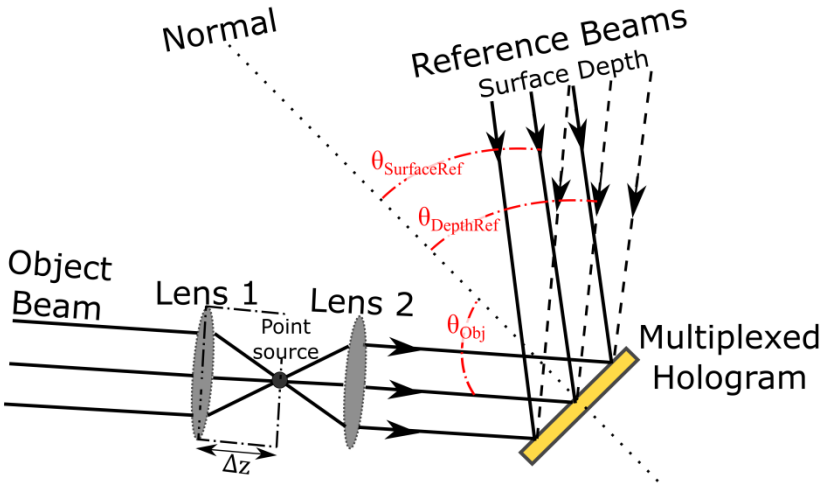

Figure 2.3: Recording geometry of a two channel multiplexed hologram. The recording angle of the object beam, θ_{obj}, is constant for each recording. The reference beam angle, θ_{ref}, changes for each depth position to correspond to different replay angles which will be imaged onto the camera during imaging.

2.3.2 Further VHI Development

Research on the VHI technique has led to the development of specialized imaging set-ups to improve the imaging characteristics of the volume holographic method. In the standard VHI system, imaging is degenerate, meaning that the wavelengths from the source illuminating the object are not spatially separated and multiple, unwanted, Bragg matching conditions are met. This degeneracy allows light from multiple depths to be diffracted into each image channel, resulting in high background levels. Techniques to improve the imaging abilities of VHI systems include phase contrast imaging[12,13], advancements in illumination techniques through dispersive elements[14–16], fluorescence imaging[3,17,18], and depth selectivity based on a wavelength coded design[19].

2.3.2.1 Phase Contrast

Weak phase features in many objects of interest give rise to the need of contrast enhancing systems. Phase contrast methods are able to visualize samples while intact, living, and unlabeled[20]. The cause of phase variations in transmission samples occurs as light diffracts and scatters through the sample. In a homogeneous sample, the index of refraction of a material will change uniformly as light travels through it. However for non-homogeneous samples, like organic tissues, varying indices of refraction will occur in the sample due to the presence of materials such as lipids and proteins. The type of phase information from a sample will vary for coherent and incoherent illumination.

For coherent light systems, light traversing through the sample will continue to have a similar amplitude structure to that of light which passes around the object but the phase of the wave becomes shifted by the tissue structures. Light reflecting from a sample can be collected through a set of polarization filters and sheared using a birefringent prism[21]. The overall change can be determined as a phase shift and a difference in optical path length. Optical Path Length (OPL) is the thickness of a sample multiplied by the index of refraction of the surrounding material, $OPL = n * t$. The difference between the optical path for light traveling through an object and for light traveling through the surrounding material is calculated using the Optical Path Difference equation, $OPD = \Delta = \left(n_{sample} - n_{surround}\right) * t$. The phase shift caused by an object can be calculated from the OPD value and the wavelength of interest. The relationship is provided: $Phase\ Shift = \frac{2\pi\Delta}{\lambda}$. When observing a sample in bright field mode, the phase shift is not large enough to enhance contrast.

An example of an incoherent phase system was the knife edge method presented in the mid-19th century by Leon Foucault. The introduction of the knife edge method was originally used for characterization of astronomical telescopes[22]. August Toepler demonstrated that the technique was also applicable to microscopy. The Schlieren illumination technique places a knife edge at the back focal plane of the microscope objective to reveal improved imaging properties of transparent objects. The knife edge aperture acts as filter to block half of the low spatial frequency light. The transmittance of the light, in Fourier space, is now defined as $t_{knife}(f_y) = \frac{1}{2}[1 + sgn(f_y)]$[23]. This method is not as widely used as phase contrast and interference methods due to restrictions of having a 4f-imaging set-up. However, the 4f-imaging set-up is commonly used in VHI systems.

In 2011, Yuan Luo introduced a knife edge into the optical path of a benchtop version of a VHI system, creating a simple phase contrast imaging system[12]. The set-up in this paper, shown in Figure 2.4, utilizes 4f relay systems which allows for the knife edge to be placed at a focal plane conjugate to the volume holographic pupil. This placement of the knife edge provides enhancement of weak phase information leading to an improvement of edge detection and an increase in the contrast ratio.

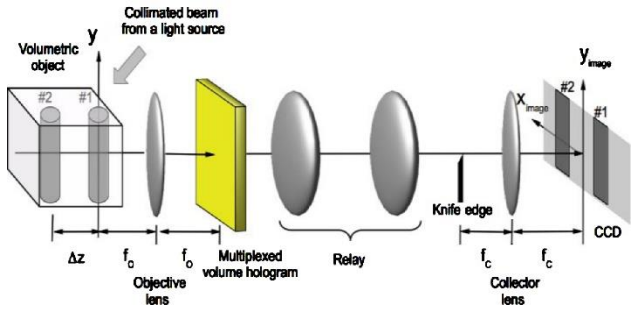

Figure 2.4: Placement of a knife edge into a VHI imaging system, as published by Luo et. al.[12]

Later in 2013, Oh et. al., designed a VHI system which designed a spatial filter-encoded volume hologram which removed the need of placing a knife edge at a conjugate plane to the holographic element pupil[13]. During the recording of the hologram, the knife edge filter was relayed onto the hologram during the recording process, placing the knife edge directly at the pupil of the system. The spatial filter-encoded VHI system, shown in Figure 2.5, was tested using unstained samples to match the conditions of a non-phase coded VHI set-up. The results from the spatial filter-encoded VHI provided higher contrast ratio images when compared to the system using a non-phase coded hologram. Overall, this system combines wavefront filtering for spectral and spatial images and adds a phase element to enhance phase features, such as edges.

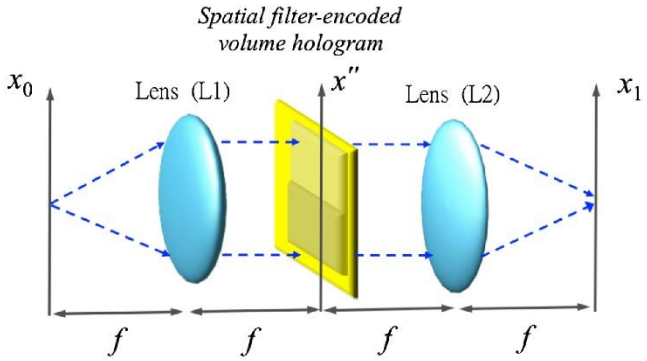

Figure 2.5: Spatial filter-encoded volume hologram simplified optical set-up as published by Oh et. al.[13]

2.3.2.2 Dispersive Illumination

Structured illumination is a technique of modifying the illumination to improve image contrast. The use of structured illumination has provided improved microscopy ability in the areas of optical sectioning, and phase imaging[24,25]. VHI systems utilizing broadband illumination result in volume holographic images which do not display the same depth selectivity as the monochromatic system. The depth selectivity degradation is due to the source having multiple wavelengths imaging an object, but only one wavelength being capable of matching the Bragg condition. Discussed below is the implementation of dispersive illumination methods in a VHI system. Dispersive illumination is a means of changing the structure of a broad source into an array of light that is sorted by wavelength.

The first design utilizing dispersive illumination is the Rainbow Volume Holographic Imaging (RVHI) system, demonstrated in 2005 by Wenyang Sun and Gerorge Barbastathis[14]. The system, shown in Figure 2.6, starts with a collimated white light source which is diffracted and collected by a cylindrical lens. The cylindrical lens forms a line focus for each wavelength of light onto the sample. Light reflecting from the sample is collected with a standard VHI system and the volume hologram is able to reject out-of-focus light having a Bragg mismatch. All of the in-focus portions of the object are Bragg matched and can be imaged. The design is capable of imaging with a 15° field of view with 250 μm VHI depth selectivity. Since this method of illumination requires that the light be external from the imaging path, this illumination method is not ideal for in-vivo endoscopic use.

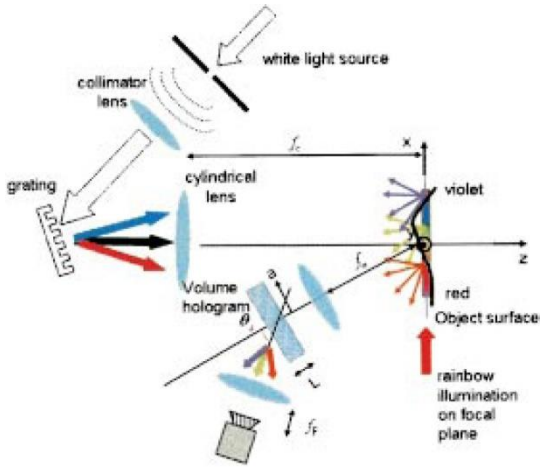

Figure 2.6: Rainbow Volume Holographic Imaging (RVHI) system layout as published by Sun et. al.[14]

Further development of the rainbow illumination led to the implementation of a confocal-rainbow VHI (CR-VHI) system which utilizes common optical paths for illumination and imaging[15]. In the confocal rainbow VHI design, light is brought into the system by a beam splitter and is sent through a holographic element toward the objective lens, the light is focused onto the sample with a dispersion effect related to the angular bandwidth of the hologram. Light is reflected off the sample and collected by the objective and sent through the same holographic element. The diffracted light is collected by a lens and focused onto the camera. A schematic of the system is provided in Figure 2.7 The experimental results show that as the object is moved through focus the image sharpness and energy decrease whereas in a standard VHI set-up the energy would not decrease, only the image sharpness. The CR-VHI reported a ten times greater depth resolution compared to VHI prototypes[15].

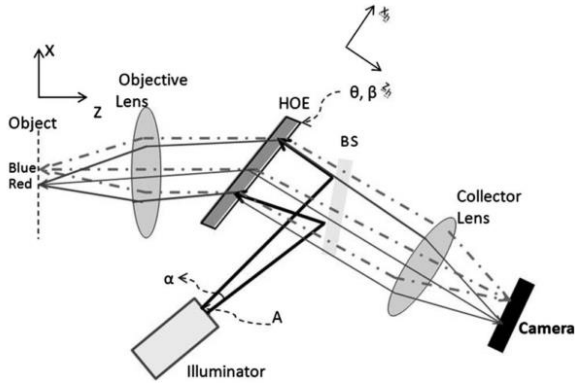

Figure 2.7: Layout of the CR-VHI presented by Castro et. al. in 2011[15]

A modification of the CR-VHI system was presented by de Leon et. al. in 2012[16]. The dual-grating confocal rainbow VHI system utilizes a secondary volume holographic element as used in the Sun et. al. VHI design but makes use of the common illumination and imaging paths of the Castro et. al. confocal-rainbow system. The dual-grating CR-VHI depends highly on the dispersion effects of the illumination hologram aligning to the imaging hologram. Any mismatch of the dispersion can results in a reduction in the FOV of the image. A schematic of the dual grating CR-VHI is provided in Figure 2.8.

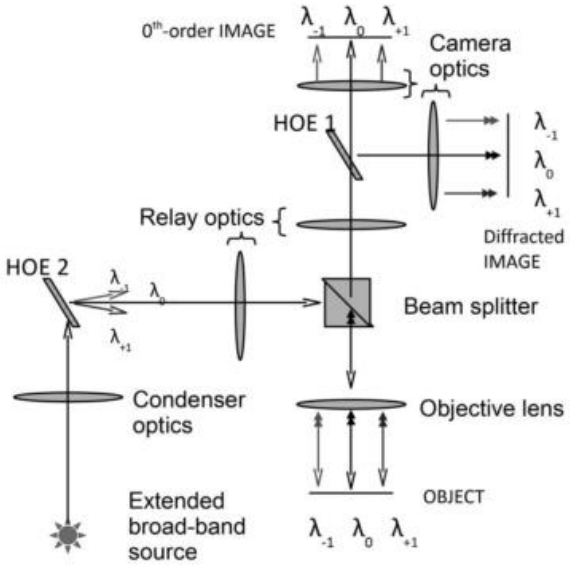

Figure 2.8: Generalized schematic of the dual grating CR-VHI as presented by de Leon et. al.[16]

The above three papers on dispersed illumination demonstrates the different methods in which the structured illumination can improve VHI depth selectivity. One drawback of dispersive illumination systems, the non-common path set-up, was corrected for in the Castro et. al and de Leon et. al. systems. Another drawback is from alignment and grating matching complications that arise in a two diffraction grating system. The system presented by de Leon et. al. showed that a mismatch of the gratings resulted in a vignetted FOV.

2.3.2.3 Reflectance and Fluorescence

Building upon the VHI benchtop systems of D. Psaltis[26] and G. Barbastathis[27], Yuan Luo et. al. developed a laser-induced fluorescence VHI system[17]. The fluorescence mode imaging presented by Luo et. al. uses a tripled Nd:YAG laser (355 nm) as the illumination source. The laser emission is at the correct wavelength to cause fluorescence of tissue stained with acridine orange dye. This fluorescence dye has an emission peak at 550 nm and a bandwidth of 100 nm. The hologram is designed to diffract light emitted at the fluorescence wavelengths. The excitation wavelength is significantly different from the emission wavelength and passes through the hologram since it is not Bragg matched.

A version of the VHI system that can image in both reflectance and fluorescence mode was used in a clinical trial to image ovarian cancer[3]. This system operates at two imaging depths to maximize the FOV of the imaged region on the camera. The depth separation is 50 μm for imaging of epithelial and stromal microarchitecture. This system utilized a 690 nm LED in reflectance mode and a 635 nm laser source for excitation in fluorescence mode. Two contrast enhancing agents were used in this trial, a nuclear dye (HCS NuclearMask™ Deep Red Stain)

and a membrane dye (Vibrant® DiD Cell Labeling Solution). Both dyes have an emission peak near 670 nm. The samples used for this experiment were biopsied human ovary and fallopian tube samples. During the course of the trial, approximately 100 samples were collected and imaged, providing data in both reflectance and fluorescence modes. Image processing methods were applied to the raw images and compared to histological slides prepared by a pathologist. This paper concluded that the VHI system provided clear images of surface changes for the reflectance case. For the case of the fluorescence images, the signal returned by the sample was much lower than the reflectance image, but was still sufficient to enhance cell membrane features. The conversion from this benchtop model to a handheld endoscopic version is discussed in Chapter 3.

2.3.2.4 Wavelength Coded

An issue which arises in VHI systems is a reduction of contrast resulting from the use of a single broadband source and the degeneracy of the hologram and holographic channel crosstalk. Contrast reduction due to hologram degeneracy can be corrected though the use of dispersive illumination, as previously discussed. The reduction of contrast reduction from holographic channel crosstalk can be corrected by using two sources with large spectral separation. Holographic channel crosstalk arises in reflectance systems utilizing a single source for object illumination. Light reflecting off an object from surface and depth planes will have the same wavelength when interacting with the hologram. Although the hologram is designed to accept light only from particular planes, background light from scatter can affect the expected wavefront curvature and result in excess background light.

In 2010, Yuan Luo et. al. introduced a wavelength coded design for multifocal microscopy[19]. A schematic of this design is provided in Figure 2.9. The wavelength coded design uses a blue (488 nm) wavelength to illuminate surface structures and a red (633 nm) wavelength for depth images. The hologram is encoded such that one wavelength and wavefront will be directed toward one half of the camera, while the other wavelength and wavefront will be directed toward the other half of the camera.

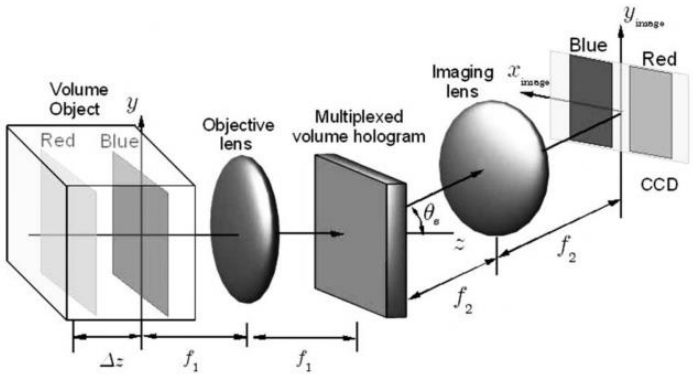

Figure 2.9: Wavelength coded multifocal microscope set-up as provided by Luo et. al.[19]

This method provides images of two different depths without crosstalk between image channels since the two gratings are designed to have Bragg matched conditions for very specific wavelengths. The wide separation of the peak wavelengths leads to complete rejection of light at wavelengths well outside the designed range. Chapter 4 describes the adaptation and miniaturization of the wavelength coded VHI technique for use in an endoscope.

Chapter 3
Reflection VHI Endoscope System

3.1 Introduction

The motivation for the VHI benchtop system and the fabrication and testing of a miniaturized VHI endoscope is the high rate at which ovarian cancer is diagnosed in a late and more deadly stage. According to the American Cancer Society, ovarian cancer was the cause of an estimated 14,240 deaths in the United States in 2016[28]. In the realm of gynecological cancers, ovarian cancer leads with 22,280 estimated new cases over the course of a year. Ovarian cancer is problematic since there is a low occurrence of symptoms while the cancer is still in a localized stage. When the cancer is found early, the 5-year survival rate is as high as 92%, however only 15% of new diagnoses are found in this stage.

There is a critical need for the development of an accurate screening method for early detection. Many imaging modalities, such as confocal microscopy and optical coherence tomography, have been working to assist with this challenge[8,29–34]. The VHI imaging method, as introduced in Chapter 2.3, was used successfully for ex-vivo evaluation of ovary and fallopian tube samples[3]. The benchtop VHI system simultaneously imaged two tissue depths by utilizing a multiplexed volume holographic element. The development of a reflectance VHI endoscope system will allow for in-vivo evaluation of tissue samples.

The VHI endoscope designed for this dissertation will not utilize fluorescent markers, as seen in the benchtop version, due to a low number of clinically approved dyes in the desired wavelength range. The following sections contain an outline of the optical design, fabrication,

and testing of the reflectance VHI endoscope reported in the 2017 publication, see Appendix A.1.

3.2 Optical Design

When considering the miniaturization process for the VHI endoscope, it is critical to take into account the physical requirements in addition to the optical requirements. When reducing system size, there is a tradeoff between optical element diameters and system field of view (FOV). Obtaining the proper balance between requirements and geometric constraints is a large part of the optical design.

3.2.1 Design Requirements

Using ovarian cancer as our sample of interest, design requirements for the system began by considering that irregularities in the epithelial layer is an indicator of early stage cancer[35]. This means that for the desired VHI endoscope system, a feasible clinical requirement is the ability to image not only the surface of the epithelial layer but also a 3-cell-depth region (approximately 50 μm) deeper to capture the majority of the epithelial layer thickness. The field of view was maximized for the case of two multiplexed elements in the volume holographic element. A field of view of 500 μm x 1000 μm was determined to be an ideal condition to ensure a total imaging time of 1 minute to evaluate a tissue region of 5mm x 5mm in size. The optical resolution of the endoscope was chosen based on the need to visualize 2 μm features within the sample, relating to 250 lp/mm on a USAF 1951 resolution chart. Mechanically, the design required that the protruding section of the rigid endoscope be a minimum of 250 mm as measured from the distal tip to the handle attachment. This length allows the probe section to reach the necessary tissue

sites during laparoscopic observation for a larger range of body shapes and compositions. Additionally, the system needed to be able to be used in a standard operating room environment with a 5 mm laparoscopic trocar. A full summary of the system requirements can be found in Table 3.1

Table 3.1: Desired Endoscope Specifications for In-Vivo Use

Field of View	500 μm x 1000 μm
Resolution	2 μm
Length of Endoscopic End	250 to 300 mm
Total Endoscopic Diameter	3 to 5 mm
Separation of Image Planes	50 to 75 μm

3.2.2 Design and Modeling

The original design for the endoscope, conceived by Erich de Leon, consisted of a 9-element objective segment and four 7-element relays. Although this design was well modeled, mechanically and optically, the desired imaging performance was not achieved. Taking into consideration the availability of lens diameters and reducing the complexity of the original design, a gradient index (GRIN) based system was developed. The endoscope probe is connected to a handle which contains the holographic component and the camera. The design process is broken down into smaller sections for each of the following: handle, illumination, and endoscope assembly.

3.2.2.1 Handle Optics

The handle section of the endoscope system is a modification from the benchtop VHI system presented by Orsinger et. al. in 2014[3]. The goal of this section of design was to take the benchtop design and condense the main components down into a portable system. In the benchtop version, two relays were used; one for pupil matching the objective to the hologram plane and the second

relay to extend the system which allowed room for placement of a large camera. In the handheld system the second relay was not required and was removed to reduce the number of optical elements. The camera for the handheld was chosen to be a Thorlabs DCC3240N to accommodate weight restrictions.

The same microscope objective used in the benchtop is used in the handheld system. The microscope objective is an Olympus Ultra Long Working Distance (ULWD) MSPLAN 50X with a numerical aperture (NA) of 0.55. Since the pupil of the objective needs to be matched to the hologram plane, the relay lenses are updated to have a larger focal length (>40 mm) to accommodate the modified illumination geometry. To achieve this, the lenses used in the relay are achromatic doublets with focal lengths of 100 mm and 75 mm, which have an overall focal length of ~43 mm. The camera lens is a 50 mm focal length achromatic doublet and the camera lens is a Thorlabs DCC3240N with a 1280x1024 pixel array of 5.3 μm square pixels[36].

The camera lens focal length was determined by the camera pixel size and the Nyquist criterion. This design allows for the camera sampling to not limit the system for future designs when improving the optical components without requiring a change in magnification. In order for Nyquist criterion to be met, two pixels of the camera are required per resolvable point in object space. The smallest feature on a high resolution bar target with a width of 0.78 μm (1.55 μm per line pair) is used to set the magnification. Following the Nyquist calculation, 2 pixels on the camera (10.6 μm) is required for a single line from the bar target (0.78 μm). The magnification is calculated to be 13.59 to achieve this condition. The focal length of the high NA objective lens is fixed at 3.6 mm, thus the camera lens is chosen through back calculation of the

magnification equation, $|f_{camera}| = |m * f_{objective}| = 48.92\,mm$. The selection of the 50 mm focal length allowed for the selection of an off-the-shelf lens, resulting in a system magnification of 13.9.

Prior to adding the volume holographic element, the system is modeled in the optical design software, ZEMAX. The lenses are input into the software using a paraxial lens as the microscope objective and real lenses for the relay and camera lenses. The system is set-up in a straight-through configuration to assess the expected optical performance. Once the lenses are roughly placed, initial optimization is performed using a standard RMS spot size merit function. The system layout, spot diagram, and MTF plots are provided below in Figure 3.1-Figure 3.3. The MTF value at a 10% cutoff is 128 cycles/mm and the RMS spot radius is shown to be 3.351 μm.

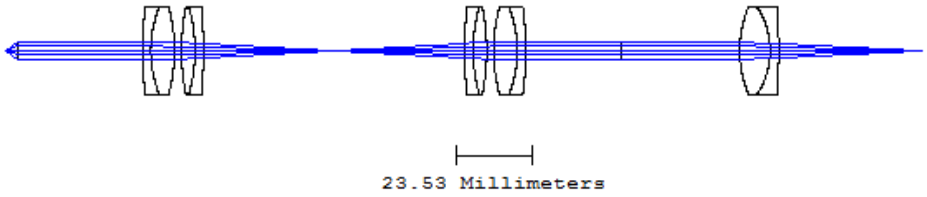

Figure 3.1: Straight through layout of the handle. The microscope objective is set as a paraxial lens element, one focal length away from the object position. The hologram will be placed at a pupil plane between the camera lens and the relay lens.

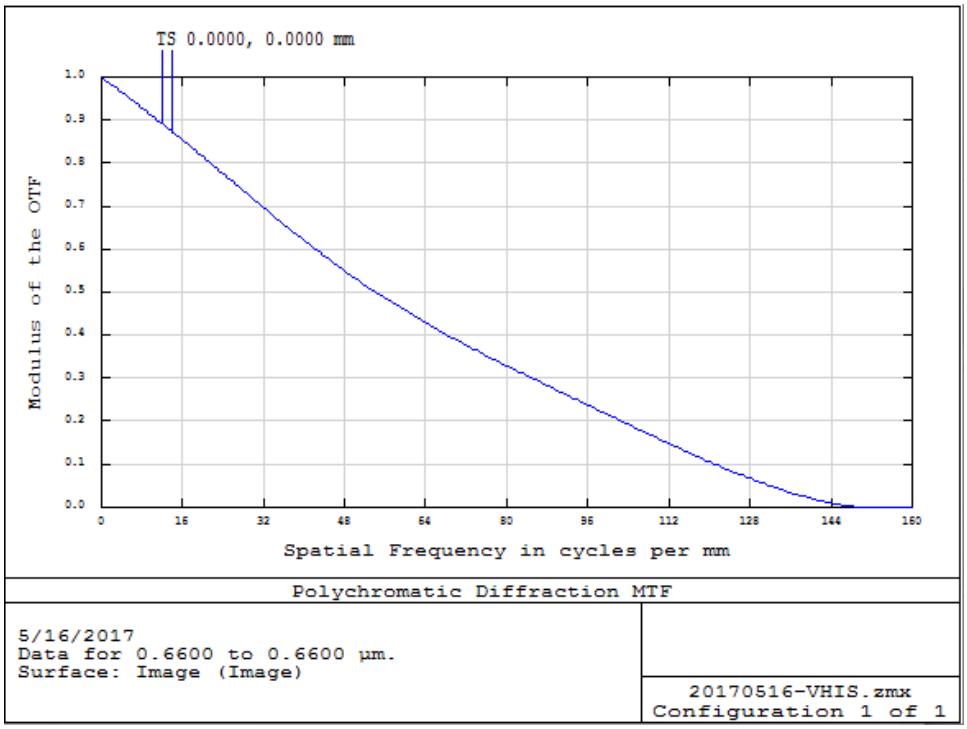

Figure 3.2: The MTF provided by ZEMAX shows a 10% cut off of 128 cycle/mm

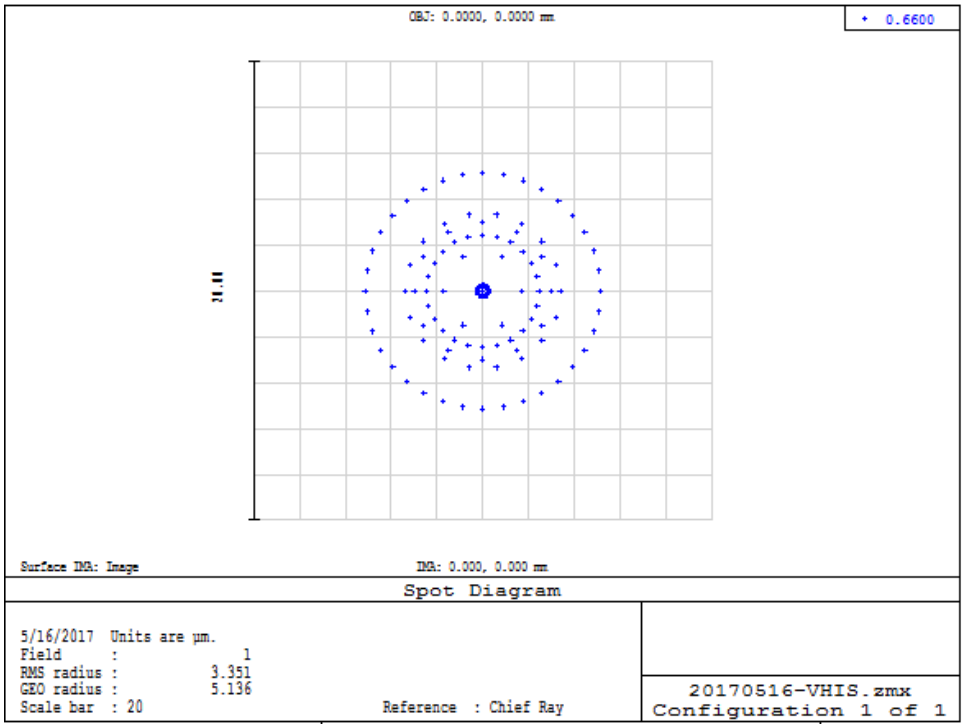

Figure 3.3: The spot radius at the image plane is 3.351 µm RMS and 5.136 µm Geometric.

At the output of the relay, the volume holographic element is placed. The hologram is enclosed in a standard ThorLabs beam splitter cube with a custom 3D printed holder for the hologram. The holder is designed to give minor degree of freedom for adjustment of the hologram height, tip, and tilt. The camera lens is placed a focal length away from the hologram and is followed by the camera. All components are connected via ThorLabs 30 mm cage plate systems for 1 inch optical components. A list of the optics used for the design of the handle is shown in Table 3.2 and a schematic of the mechanical and optical design is provided in Figure 3.4.

Table 3.2: List of optics used in the handle assembly

Optic	**Company**	**Type**	**Focal Length**	**Quantity**
ULWD MSPLAN50	Olympus	Objective	3.6 mm	1
AC254-100-A	ThorLabs	Achromatic Doublet	100 mm	2
AC254-075-A	ThorLabs	Achromatic Doublet	75 mm	2
AC254-050-A	ThorLabs	Achromatic Doublet	50 mm	1
DCC3240N	ThorLabs	CMOS Camera	N/A	1

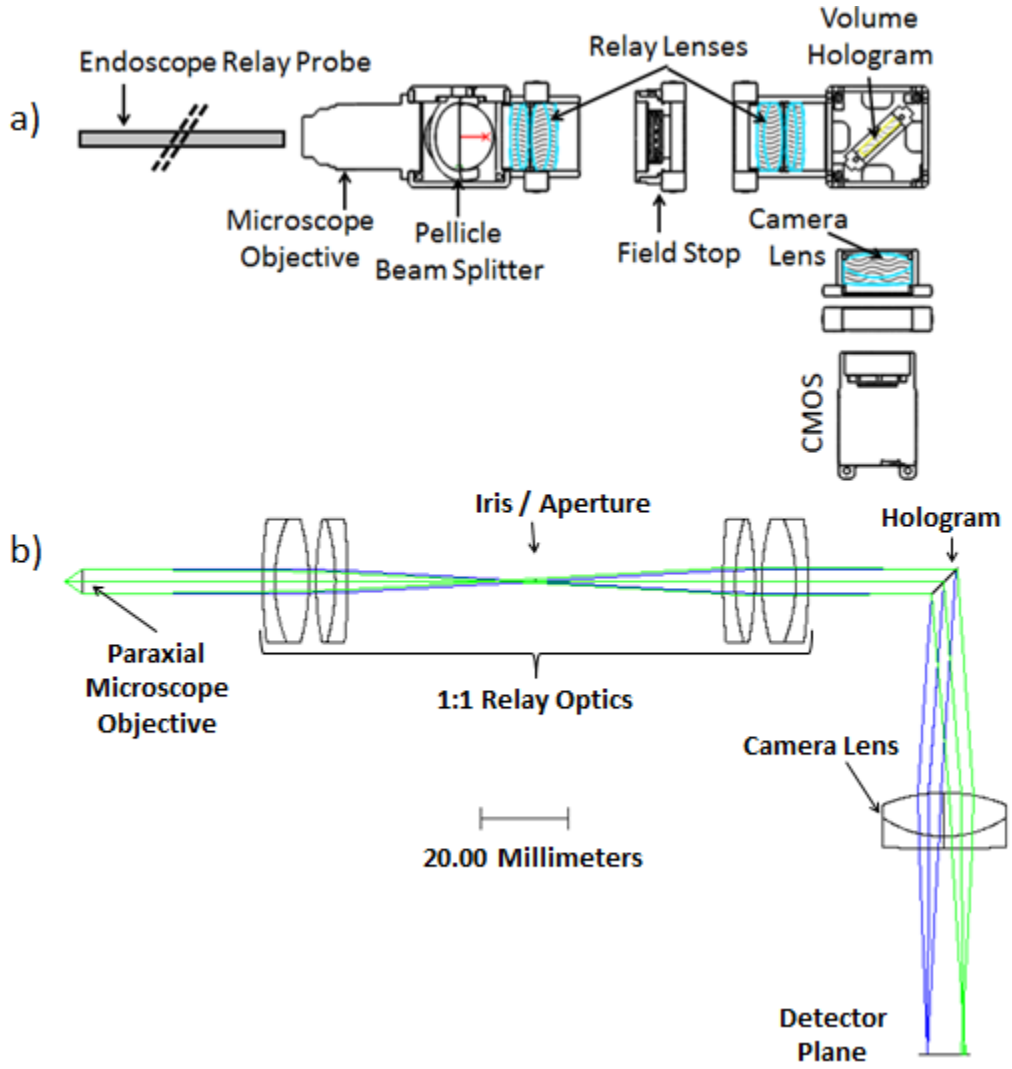

Figure 3.4: a) SolidWorks cross section rendering of the handle component layout b) Zemax Model of the handle components with the objective being modeled as a paraxial lens and the pellicle not shown.

The volume holographic element used in the handle of the endoscope is recorded in a 1.8 mm thick piece of phenanthraquinone doped poly methacrylate (PQ-PMMA, n=1.49) using a 514.5 nm Coherent Innova 300 Argon laser. Each hologram in the multiplexed element is recorded to sample light from a different object depth in the tissue sample, with a total separation of 50 µm. In previous versions of hologram design, the depth channel was assigned to a planar holographic element relating to a collimated wavefront and the surface to a curved wavefront. However, in this hologram, both the surface and depth channels are recorded with curved

wavefronts that have the total curvature split with equal but opposite direction of curvature for the two imaging depths. This recording configuration results in a multiplexed hologram that achieves 50 μm channel separation, Δz, with equal amounts of induced hologram aberration which occurs from the difference between the recording and reconstruction wavelength (e.g.514.5 nm for recording and 660 nm for reconstruction).

During recording of the hologram, the object beam is set to 33.4° in air relative to the normal of the hologram surface. The reference beam angles for the surface and depth channels are 34.92° and 31.88°, respectively. These angles create an inter beam angle of 90° between the object and reference beams in replay. The diffraction efficiency for volume phase transmission holograms is given by $\eta = \frac{\sin^2(\nu^2+\xi^2)^{\frac{1}{2}}}{(1+\frac{\xi^2}{\nu^2})}$ (with $\nu = \frac{\pi n_1 d}{\lambda c_r c_s}; \xi = \frac{\vartheta d}{2c_s}$) where $c_r = \cos(\theta_r)$ and $c_s = \cos(\theta_s)$ where θ_r and θ_s are respectively the reconstruction and diffracted beam angles[11].

After recording, the diffraction efficiencies are measured using a 633 nm laser. The surface hologram had a diffraction efficiency of 42% and the depth hologram had a diffraction efficiency of 50%. A list of hologram specifications are provided in Table 3.3.

Table 3.3: Reflectance hologram design specifications and post-recording parameters

Design Specifications		
Recording Wavelength	514.5 nm	
Material	PQ-PMMA	
%PQ	0.7%	
Thickness	d = 1.8 mm	
Index of Refraction	n = 1.49	
Grating Period	$\Lambda_{surface} = 458.6$ nm	$\Lambda_{depth} = 476.0$ nm
Q parameter	$Q_{surface} = 23817$	$Q_{depth} = 22110$
Object Beam Angle	$\lvert\theta_{Obj}\rvert = 33.4°$	
Reference Beam Angles	$\lvert\theta_{SurfaceRef}\rvert = 34.92°$	$\lvert\theta_{DeothRef}\rvert = 31.88°$
Post-recording Parameters		
Replay Wavelength	660 nm	
Inter Beam Angle	90°	
Exposure Density	2765 ms/cm^2	2488 ms/cm^2
Diffraction Efficiency (η) at 633 nm	$\eta_{surface} = 42\%$	$\eta_{depth} = 50\%$
Calculated η at Reconstruction λ	$\eta_{surface} = 41\%$	$\eta_{depth} = 47\%$

3.2.2.2 Illumination System

Illumination for the system is provided by a 660 nm LED with a 20 nm bandwidth. The LED is coupled into a 600 µm core fiber which is able to be attached to the handle. The fiber coupling is achieved through the use of a fiber SMA connector in contact with the LED dome lens as shown in Figure 3.5.

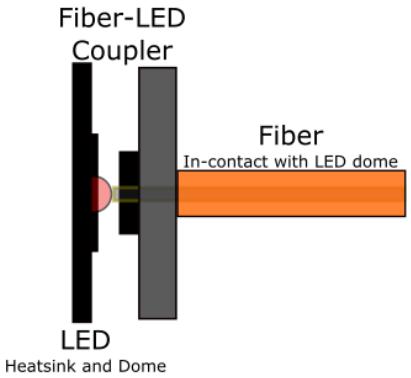

Figure 3.5: LED to fiber coupling schematic. The Thorlabs fiber is connected to a SMA adaptor and placed such that the fiber end and the LED done are in contact.

In order to achieve Köhler style illumination, the end of the fiber is imaged onto the pupil of the microscope objective, which focuses incident planar light at the sample. The imaging and magnification of the fiber is achieved with a lens pair consisting of a 10 mm focal length aspheric lens and a 50 mm achromatic lens (Thorlabs, ACL1210-A and AC127-050-A respectively).

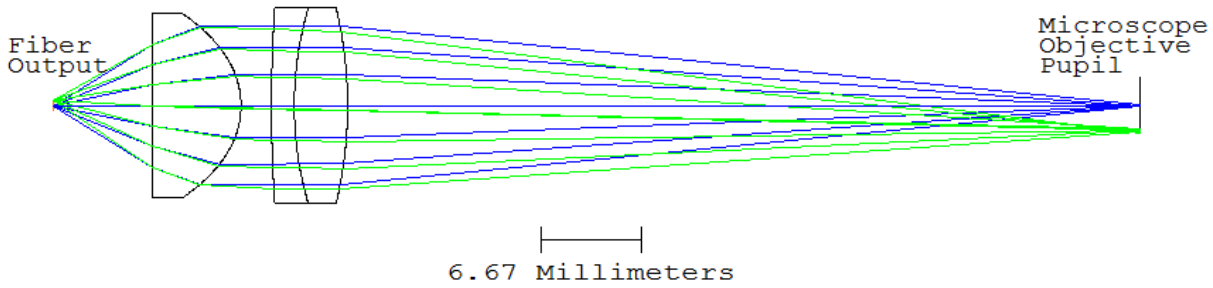

Figure 3.6: Fiber illumination lenses. Thorlabs, ACL1210-A and AC127-050-A expand the fiber from 600 μm diameter to fill a 4 mm aperture at the microscope objective pupil

A fold mirror is placed after the lenses to direct the light toward the pellicle beam splitter and then to the objective. A SolidWorks rendering of the handle, with the illumination path, is provided in Figure 3.7. The solid line represents a central ray entering the system through the illumination lenses, fold mirror and pellicle. The dashed line represents a central ray from the microscope objective through the relay to the holographic element. The part list for the illumination path is given in Table 3.4. The pellicle beam splitter is a designed to have 50:50 R/T when operating at 635 nm (Thorlabs, CM1-BP150). Alignment of handle components is fully discussed in the alignment and fabrication section for the handle in section 3.3.1.

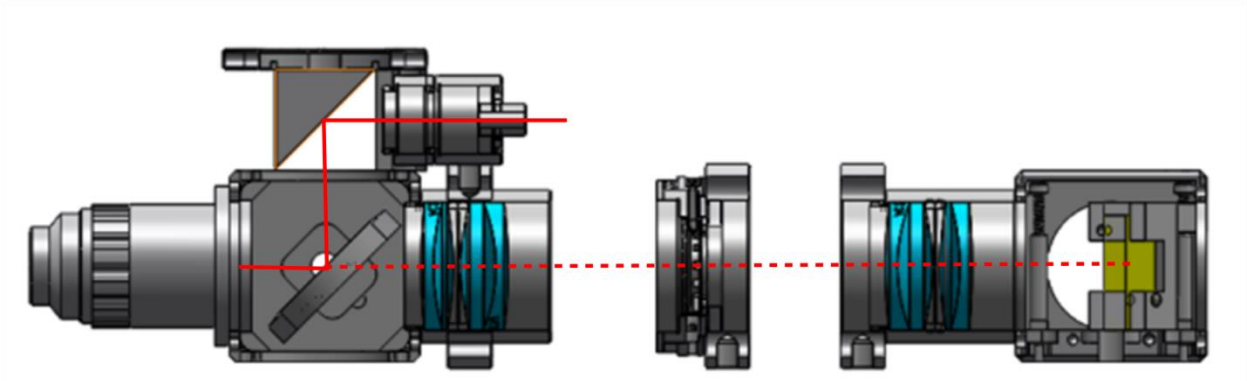

Figure 3.7: Cross section slice of the handle showing the placement of the illumination lenses, fold mirror and pellicle relative to the objective holder and relay components. The solid line represents a central ray path through the illumination optics while the dash line represents a central ray path through the imaging optics to the hologram.

Table 3.4: List of materials for the illumination set-up

Optic	Company	Material	Diameter	Quantity
ACL1210-A	Thorlabs	B270	12 mm	1
AC127-050-A	Thorlabs	N-BK7/SF2	12.7 mm	1
M29L05	Thorlabs	Multimode Optical Fiber	600 µm Core	1
CM1-BP150	ThorLabs	50:50 Pellicle 635nm	N/A	1

3.2.2.3 Endoscope Probe

Endoscope Probe: General Design

The endoscopic probe design is developed from a triplet Gradient Index (GRIN) lens system used for multiphoton and fluorescence endoscopes[37–39]. The triplet-GRIN design is a modification of a single GRIN design utilizing an element with a pitch of P=1.5[40]. In the triple-GRIN two higher NA GRIN lenses are used to for imaging and coupling into an optical system. The GRIN lenses used are defined as radial GRIN components having a material index of refraction that changes radially inside the optic. The lenses are typically defined to have a central index, n_o, and a gradient constant, g [mm^{-1}], which are then used to calculate the index for each radial layer of the GRIN. This index variation causes a sinusoidal path within the optic, which is leads to the characterization of pitch, P=1, which is a full sinusoidal path. Equations for GRIN calculations are provided in Table 3.5**.**

Table 3.5: Summary of key GRIN parameters and equations

Pitch Length	P	$\frac{2\pi}{g}$
Index of Refraction	N(r)	$n_o * (1 - \frac{g^2}{2} * r^2)$

GRIN lenses are fabricated in lengths relating to P=0.5. An integer number of P will provide no image parity change and acts as a 1:1 relay optic. A half period (P=0.5, P=1.5) will cause a parity change at the output of the system and the image will be inverted. When using GRIN lenses with P=0.25, the lenses act as collimating lenses for an object at the focus. When used in a triplet design, the P=0.25 lenses are selected based on the higher numerical aperture (NA) to improve imaging spatial resolution capabilities and better coupling with a conventional high NA microscope objective[38]. Focused light collected by the P=0.25 lens is collimated and enters the integer pitch GRIN lens. Since the integer pitch lens is a relay, the collimated light entering the system leaves at the opposite face collimated. The third GRIN lens, P=0.25, then is able to focus the light from the relay down to form an image. The standard lengths for the shorter GRIN lenses ranges from P=0.25 pitch to P=0.22 depending on the application and where the object of interest would be placed. When P=0.25 this causes perfect focus at the face of the GRIN while 0.22 pitch designs are used when a small working distance is required.

The triplet systems referenced during the design and fabrication of the GRIN probe all used a single pitch grin as the relay component with diameters ranging from 0.35 mm to 1.0 mm. When considering the triplet design for the VHI Endoscope, these diameters would have limited the system length as these relay rods are typically 20 mm to 100 mm in length. Since a probe length of 250 mm to 300 mm is desired for laparoscopic use, a larger diameter GRIN relay from GoFoton[41] was selected to accommodate this requirement. The relay lens has a diameter of 2.7

mm, length of 281 mm, and is of P=2 design. This keeps the relay at an integer multiple of P while further increasing the system length. The NA of the relay lens is 0.1 with a central gradient index of 1.610. The 0.4 NA imaging and coupling lenses are chosen to have the same diameter and are also purchased from GoFoton. These lenses are ordered at non-standard lengths of P=0.204 and P=0.202 for the imaging and coupling lens respectively after discussing the design with GoFoton design engineers. The non-standard lengths are used to accommodate the addition of BK7 windows capping the GRIN arrangement. The windows are placed for two reasons, the first being that the system requires that the optical system can be used for in-vivo applications where the laparoscopic probe is in contact with the patient. Since the production of the GRIN lens adds dopants to the glass which may be harmful to the patient, a glass window is placed between the object and the GRIN imaging lens. The second reason is due to the common path illumination being used. In the reflectance set-up, the same wavelength illuminating the sample is the same wavelength being collected. Thus an AR coated window is placed between the coupling GRIN lens and the microscope objective to reduce any back reflections from the illumination. The full system, once assembled is encased in hypodermic needle tubing with an outer diameter of 3.8 mm which is connected to a threaded retainer for attachment to the handle of the system. A schematic of the endoscope probe is shown in Figure 3.8a and the threaded system in Figure 3.8b. The optical elements used for construction of the endoscope are provided in Table 3.6. The fabrication technique used for the endoscope probe is discussed in detail in section 3.3.1.

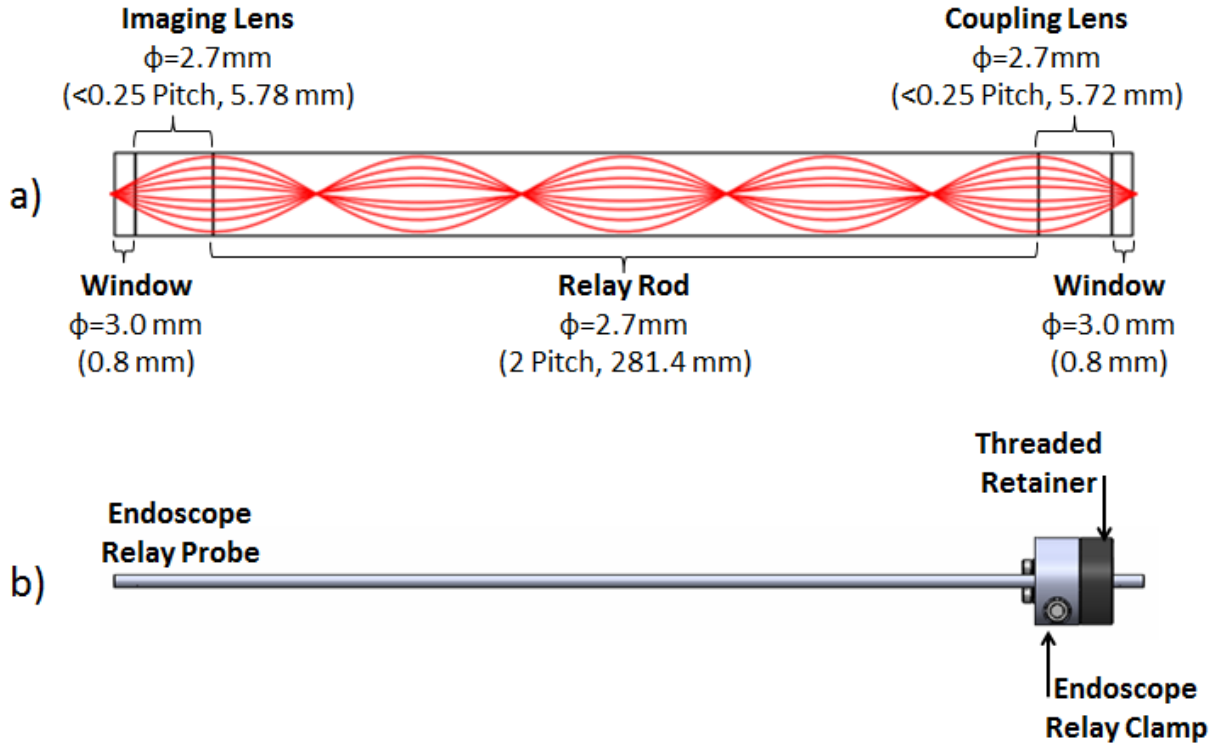

Figure 3.8: a) Schematic of endoscopic probe composed of Gradient Index (GRIN) lenses. Grin components have diameters of 2.7 mm. b) Endoscope assembly showing the endoscope probe and threaded retainer positioning. The threaded retainer allows for quick connection to the handle section.

Table 3.6: List of optics used in the endoscope assembly

Optic	Company	Material	Diameter	Index (n)
SRL-2.7	GoFoton	GRIN	2.7 mm	1.610 on axis
ILW-2.7	GoFoton	GRIN	2.7 mm	1.643 on axis
#45-272	Edmund Optics	N-BK7	3 mm	1.517

Endoscope Probe: Gaussian Beam Modeling

Once the design was reviewed based on the theoretical vales an additional check of the system was performed for the case of on-axis paraxial rays using Gaussian beam modeling. This model used Matrix methods and Gaussian parameters to determine beam waist sizes and working distance for OCT systems[42]. The methods are modified from the single mode fiber, no core fiber, and grin fiber design of an OCT system to match the design of the Triplet GRIN.

The ABCD Matrices used for the design are based on the matrices for free space propagation, refraction at an interface, and propagation through the gradient index material. These matrices are provided in Table 3.7. These matrices will calculate the exiting height and angle at the exit face when given parameters for the ray height and angle at the entrance face.

Table 3.7: ABCD Matrices used for the Gaussian beam propagation method

Free Space Propagation	$\begin{bmatrix} 1 & L \\ 0 & 1 \end{bmatrix}$
Refraction at an interface	$\begin{bmatrix} 1 & 0 \\ 0 & \frac{n_1}{n_2} \end{bmatrix}$
Gradient Index Material	$\begin{bmatrix} \cos(gL) & \frac{1}{g}\sin(gL) \\ -gsin(gL) & \cos(gL) \end{bmatrix}$
L = distance traveled in a material, g = gradient constant, n = index of refraction	

When tracing a ray through the gradient index material, the MATLAB code used 15 μm steps through the GRIN material to give an approximation of a complete ray trace. The MATLAB code for the triplet GRIN system is provided in Appendix B. The original code, created by Dr. Tyler Tate for his OCT system, was modified with permission to model the triplet-GRIN lens design[43]. The following paragraphs break down the code parameters to describe the system performance as a paraxial ray is traced through the system.

The first section of the endoscope system is the distal window and the imaging GRIN lens. The code is assuming that the light at the desired depth inside a tissue, d=0 for this example of surface imaging, is the location of the beam waist of the illumination. The beam waist of the system is determined based on the wavelength (660 nm) and the Numerical Aperture (NA=0.4) of the endoscope[44]. The beam waist of $w_o = 0.5105$ is calculated and used for the derivation of the spot size at the start of the calculation. The index of the starting material is that of water,

n=1.333, since water is used as the index matching fluid during resolution testing and is near the expected index of refraction of tissue samples. The beam waist is located at the surface of the distal window with an index of refraction, n=1.517 (N-BK7) and thickness t=0.8 mm. The beam entrance/exit heights and angles are calculated using ABCD matrices for propagation and refraction. The beam is traced, as shown in Figure 3.9, as a linear propagation through the window which is expected for a standard propagation material. The ray then propagates though the imaging GRIN lens. This GRIN has a central index of 1.643 and total length of 5.780 microns. Using this and the gradient index, g =0.222 mm^{-1}, of the material a trace is provided. The trace is achieved by taking 15 μm segments through the material and calculating the expected ABCD matrix values. It is seen that the ray in this material is not linear, but has a curvature to it, which matches what is expected for a <P=0.25 lens.

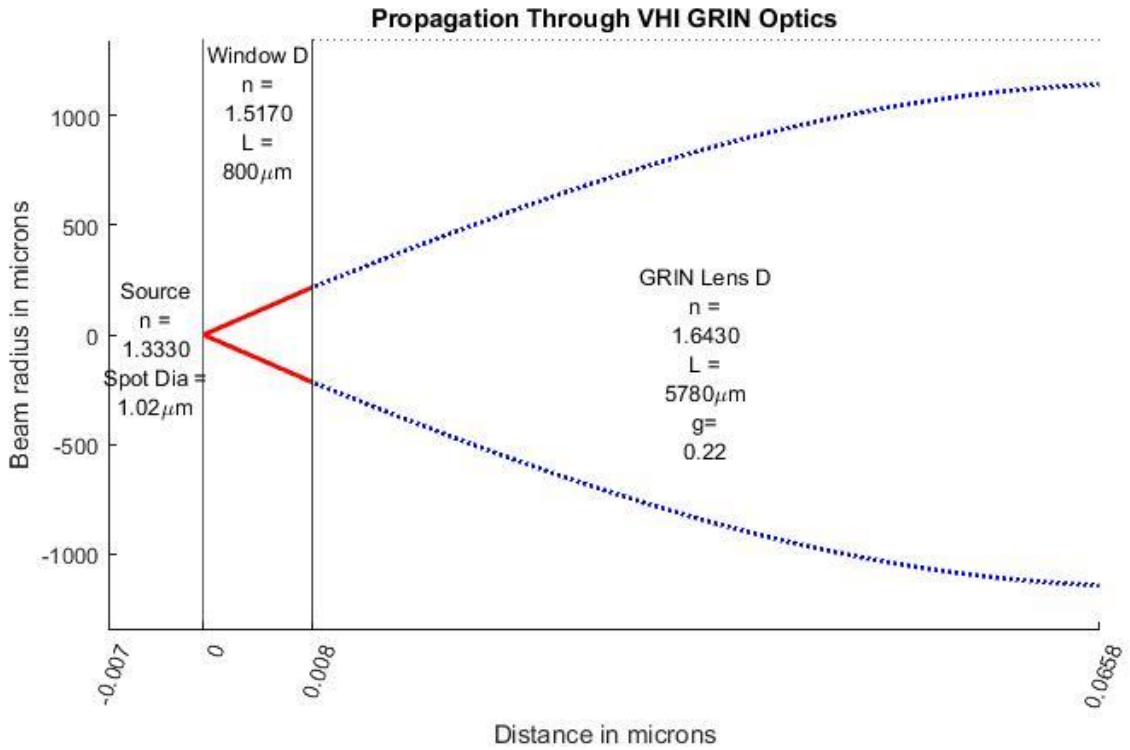

Figure 3.9: Gaussian beam modeling assuming focus of the light is in contact with the distal window of the system. The ray is traced through the window (solid line) and through the imaging lens (dotted line). As expected the light leaving the GRIN lens is close to the peak of the sinusoidal transition related to collimated light. The starting spot diameter is 1.02 μm, as derived from the assumed beam waist using the 0.4 NA property of the GRIN imaging lens.

Upon exiting the imaging GRIN lens, light enters a GRIN rod with a central index of refraction of 1.610 and length of 281.4 mm. The gradient index parameter is not provided for this lens. However, since this lens was ordered at a set pitch length of P=2, the gradient index is back calculated from the known values using the Pitch equation in Table 3.5. The calculated gradient index g- value, g=0.0446 mm^{-1}, is entered and used for the MATLAB calculations. This value is an approximation since the lens has a length variation of ±8 mm. The overall sensitivity of design to the gradient index value is unknown, however any errors would be seen if the expected sinusoidal path inside the GRIN does not fit the P=2 shape. After running the program, the ray trace shown in Figure 3.10 is obtained. The trace shows that 2 sinusoidal periods are traced within the material.

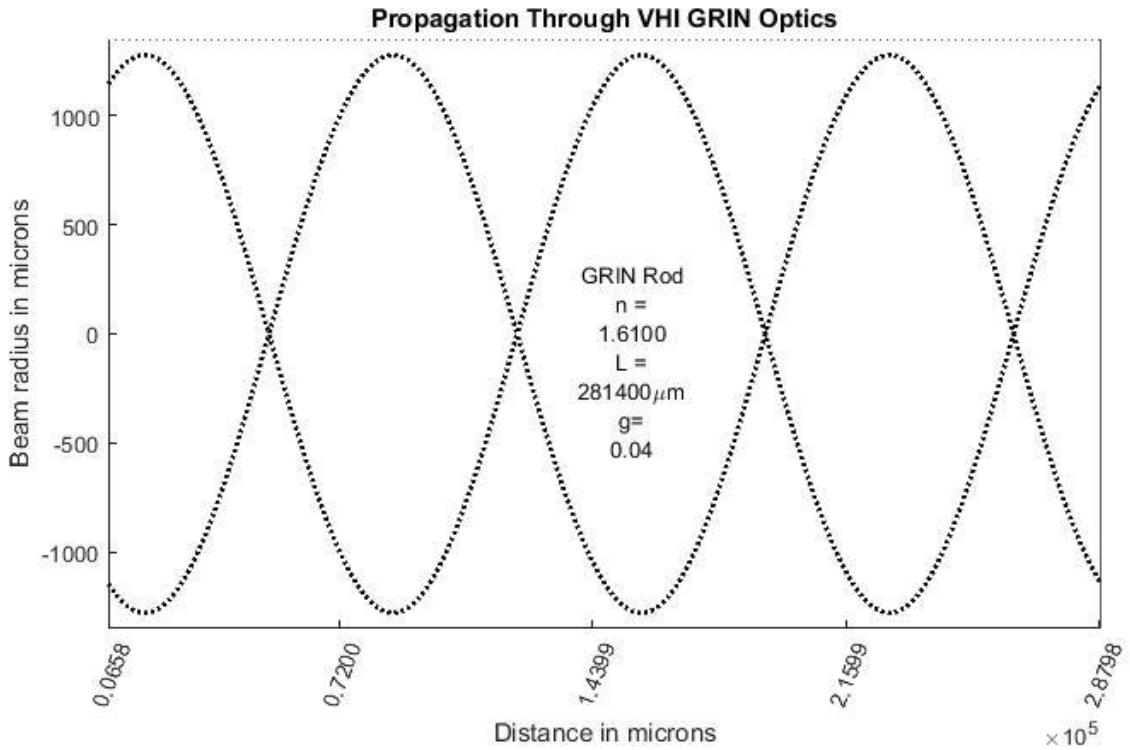

Figure 3.10: Gaussian beam modeling through the GRIN relay rod. Light from the GRIN imaging lens was not perfectly collimated, but two full sinusoidal paths are traced over the total distance of the GRIN optic.

Lastly, the system is traced through the coupling GRIN lens and the proximal window. The coupling GRIN lens has the same central index and gradient constant of the imaging lens, but a length of 5.72 mm. The proximal window matches the parameters of the distal window. The final trace, shown in Figure 3.11, shows the curved light from the coupling GRIN lens enter the window, which travels in a linear fashion, and exiting the window into air. The MATLAB code calculates an expected spot size at the output and the working distance from the last optical surface. In this case the beam is focused 640 μm from the surface of the window with a diameter of 1.10 μm.

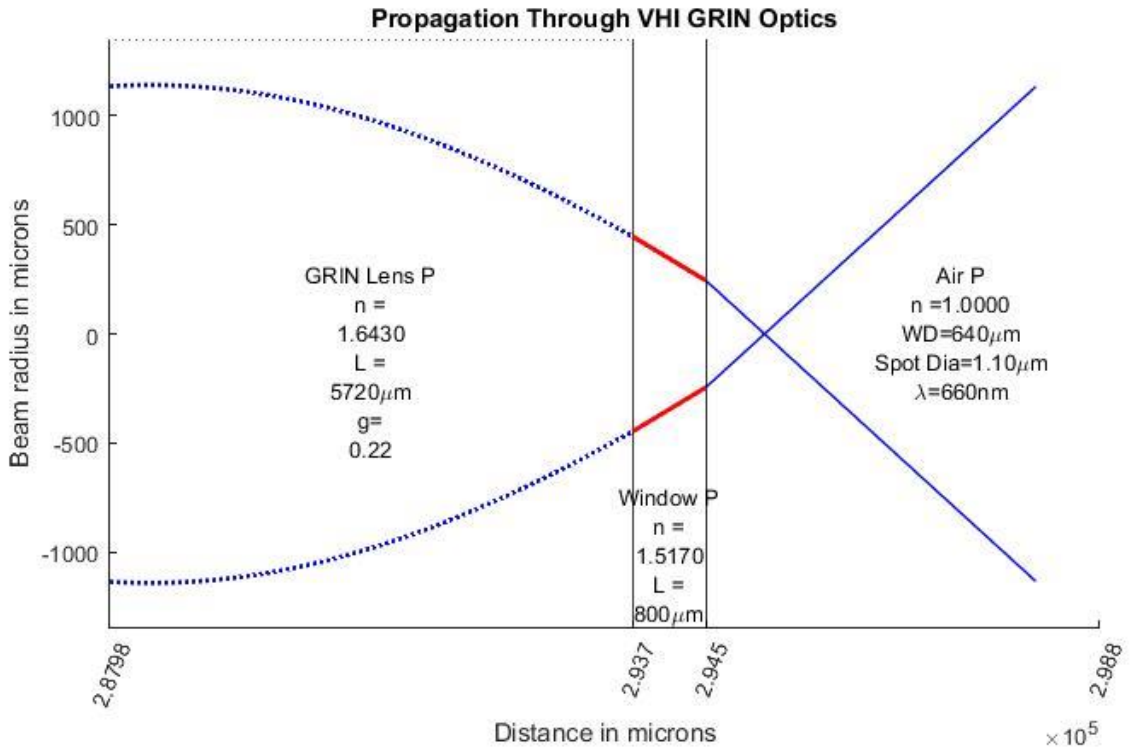

Figure 3.11: Gaussian beam modeling through the GRIN coupling lens (dotted line) and the Proximal window (solid bold line) The final intersection shows the focus of the total system 640 µm from the last surface with a spot diameter of 1.1 µm.

The modeled system allows for the magnification to be calculated by comparing the spot size of the output beam to that of the beam waist, $m = \frac{1.10}{1.02} = 1.08$. The calculated value is relatively close to the expected m=1 of a perfect system. There were a few assumptions made for this approximation, such as the back calculation of the GRIN rod gradient index parameter. This model also neglects the effect of the epoxy used to assemble the system. This model can provide simple tolerance guidelines based on the variation of parameters provided by the manufacturer, such as lens length. However, this does provide a visual representation of the system, which would not have been possible to model fully in an optical ray trace programs due to lack of information when using the GRADENT 9 profile information in ZEMAX.

3.3 Fabrication and Alignment

With the design of the system in place, the fabrication and alignment of each portion of the system is started. An overview of this process is provided in the following sub-sections.

3.3.1 Endoscope Probe

The endoscope assembly consists of three GRIN optics and two optical windows. During assembly, epoxy is used to affix the optical components together and also bond the optics to the stainless steel hypodermic needle tubes. The epoxy chosen is required to be compatible with a Hydrogen Peroxide Plasma sterilization process used at the medical center for sterilization of clinical devices.

3.3.1.1 Selection of the Epoxy

The epoxy chosen for the fabrication is Epoxy Technology (EpoTek) 301[45]. When uncured, EpoTek 301 has an index of 1.519 at 589 nm. After curing, the epoxy index will increase by ~0.03 giving an index of ~1.549 at 589 nm, as provided via discussions with EpoTek support. Compatibility with the sterilization process is not as highly ranked as a few of the other EpoTek epoxies, such as EpoTek 353ND, however the optical clarity of this epoxy is not as high as that of the EpoTek 301[46].

The reflectance values at the optical surfaces using the epoxy at the interfaces are calculated using the reflectance equation: $R = \left|\frac{n_2 - n_1}{n_2 + n_1}\right|^2$. The calculations are provided in Table 3.8 using the approximate value of EpoTek 301 at 589 nm. The surface with the greatest reflectance value is the proximal window at 4%. The total endoscope reflectance is 5.094% without the AR coating. An AR coating is applied to the proximal window surface to prevent

excess background light from reaching the camera. The total amount of light reaching the object is maximized through alignment of the fiber to the source and illumination optics. Once maximized, the power at the output of the endoscope is measured with 1 mW of power. Considering an assumed 2% reflectance from the tissue and 5.094% reflectance from the non-AR coated endoscope, the microscope objective is collecting approximately 1 μW of power from the tissue.

Table 3.8 Calculation of Reflectance values at interfaces between optical components

	Index of Refraction (n)	Reflectance (R)
Air	1.000	
Interface		4.219%
Window	1.517	
Interface		0.011%
EpoTek 301	1.549	
Interface		0.087%
GRIN Lens	1.643	
Interface		0.087%
EpoTek 301	1.549	
Interface		0.037%
GRIN Rod	1.61	
Interface		0.037%
EpoTek 301	1.549	
Interface		0.087%
Grin Lens	1.643	
Interface		0.087%
EpoTek 301	1.549	
Interface		0.011%
Window	1.517	
Interface		0.431%
Water	1.330	
Total Reflectance		5.094%

3.3.1.2 Selection of the GRIN Components

The techniques noted in the 2012 Nature Protocol of Kim et. al. were used during the assembly of the endoscope[39]. A v-groove was recommended for assembly, however due to the length of the GRIN rod, an approximate v-groove spaced guide was created using 10 inch and 3 inch cage assembly rods. The spaced guide is used to keep the GRIN components in place during the epoxy process. The assembled v-groove holder is shown in Figure 3.12.

Figure 3.12: V-groove assembly created out of 10 inch and 3 inch cage rod components from ThorLabs

The surfaces of the GRIN optics were cleaned using an optical lens cloth and methanol prior to starting the epoxy procedure. The surfaces were viewed through a microscope set-up to check for residual dust particles. The GRIN rod was placed into the v-groove with slight pressure applied using tape to keep the optic in contact with the holder. The GRIN lens was placed near the GRIN rod so both surfaces are visible through the microscope (Figure 3.13a). A small drop of EpoTek 301, mixed according to manufacturer procedures, was placed on the GRIN rod surface. Slowly the GRIN lens was pushed toward the GRIN (Figure 3.13b).

a)
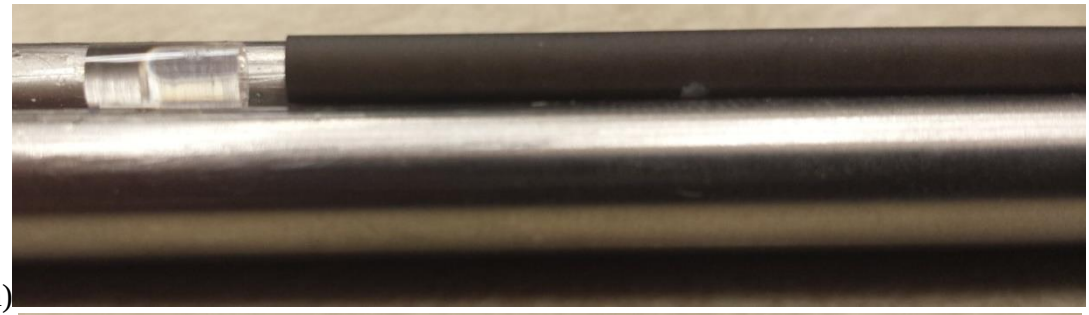
b)
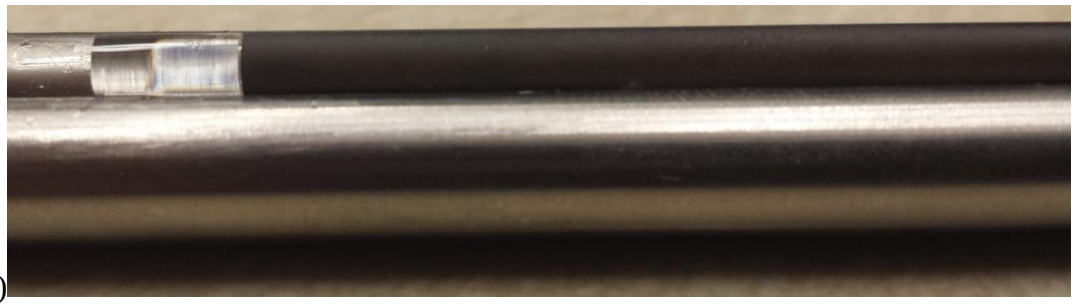
Figure 3.13: Placement of the GRIN lens and GRIN rod a) prior to placing epoxy droplet b) after applying epoxy droplet

This endoscope was placed under UV light for an hour then the process was repeated for the second GRIN lens on the opposite end. After the second UV pass, and visual assessment of alignment, a small amount of epoxy is added to the outer edges of the assembly and the 11 gauge hypodermic needle tubing (Microgroup, 304H11XX) was slid over the optic. The length of the 11 gauge tubing was shorter than that of the grin assembly with ~ 2 mm of lens accessible on each side for placement of the windows. The endoscope was placed into a 65° C oven for 2 hours, per EpoTek 301 datasheet information.

After the oven cure, the system was allowed to cool, before affixing the N-BK7 windows. The windows and GRIN surfaces are cleaned using methanol as discussed previously. The proximal window was placed such that the AR coating is the outer surface. Both windows can be applied at the same time. After the windows were in place, the system was placed again in a 65° C oven for 2 hours. After this process, the system was affixed into a 9.5 gauge hypodermic needle tubing (Microgroup, 304H09.5) cut to be the same length as the assembled system. The

same epoxy and curing method used for the 11 gauge needle tube was used. The fully cured system was attached to the threaded retainer and clamp system shown in Figure 3.8b with approximately half an inch of the probe protruding from the rear of the clamp.

3.3.2 Handle Optics

Starting with the ZEMAX model of the handle components, lenses were placed into lens barrels with the proper orientation and attached to cage plate segments as needed. The alignment began with the camera and camera lens to ensure best camera placement.

To align the camera to the camera lens, attach the camera to a cage plate and two 3-inch rods. Ensure that the 3-inch rods are in contact with the camera corners and lock the rods in place with the camera cage plat set screws. Add the camera lens and cage plate to the 3-inch rods and add two 2-inch rods in the lower sections, again having the rods touch the camera case corners and lock the camera set screws. The base set-up will look like Figure 3.14.

a) 

b) 

Figure 3.14 a) side view of the camera lens and camera alignment set-up and b) top view of the camera lens and camera alignment set-up

In this configuration the camera lens is still free to slide on the rods. Using the camera software, initiate a live view. Aim the camera and the lens at an object in the distance, this works best if the object has words or a grating pattern. Slide the camera lens until the object is in focus on the camera. When a good focus position is found, tighten the set screws on the camera lens cage plate and re-check the focus. If the focus has shifted, untighten the set screws and align

again. When the alignment is set these two components are not separated. This is kept true during the alignment of the system by keeping the 2-inch rods locked in place when attaching the 3-inch rods of the camera and camera lens assembly to the hologram holder.

Before adding the holographic element, the relay section is attached. To achieve this alignment, the camera assembly is placed in-line with the relay optics. Only the top two rods are used for the initial alignment of the relay. The relay segment closest to the hologram is placed in the lens barrel so the lens is closer to the cage place than the hologram cube. Then the lens barrel is placed in contact with the hologram cube and locked down. An adjustable aperture is added after the first relay segment and before the second segment, shown in Figure 3.15. Both of these will remain moveable during this process.

a)  b) 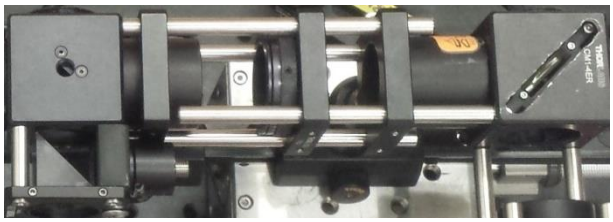

Figure 3.15: Relay Alignment documentation: a) rear relay lens locked in place and stationary to the hologram cube during alignment b) complete relay alignment showing the relays, aperture, and cubes.

Using the camera, a procedure similar to that used with the camera lens is performed for the relay. While observing an object at a distance, slide the relay lens segment furthest from the hologram cube until a focused image is achieved. Lock the lens in place using the set-screws. Verify that the position is correct and adjust the position as necessary if shifting occurs. Now the adjustable aperture can be placed. While viewing an object, slide the aperture until a focused image of the aperture edge is in focus then lock the aperture down. Two rods are attached to the bottom two holes in the pellicle holder and slid through the relay cage plates. The pellicle cube is

placed in contact with the lens barrel of the relay. When everything is locked down, the system will look like what is seen in shown in Figure 3.15b.

A right angle mirror is affixed to a thin cage plate section and placed so the edge is in contact with the pellicle cube. A custom holder for the fiber and illumination lenses was 3D printed to fit on 1 inch cage rods attached to the pellicle cube. This component is shown in Figure 3.16 and on the top plane of the handle assembly. The illumination lens barrel assembly is abutted to the right angle mirror. The location of the fiber input can be adjusted using the treaded adapter and a retaining ring. The location is set when the image of the fiber is approximately 4 mm in diameter and in-focus at the exit face of the pellicle cube after reflection.

Figure 3.16: Placement of the illumination fiber and optics into the pellicle cube.

The objective is then placed into the pellicle cube face, and locked in place with an outer diameter retaining ring to keep the objective from shifting, as shown in Figure 3.17. The objective is placed, so the visible aperture is at the focus of the illumination light. The fiber/lens barrel can be adjusted slightly and locked down such that the light entering the objective is not being clipped by the aperture.

Figure 3.17: Placement of the objective into the pellicle cube.

Lastly the hologram can be aligned. The hologram is placed into the hologram holder with the front (labeled) surface facing the relay and the back surface touching the adjustment screws as shown in Figure 3.18. The hologram holder is designed to allow for minor adjustments to the height and tip/tilt of the holographic element. When the hologram is in the holder, the holder is placed into the hologram cage cube and secured with the cage cube screws. Access to the lower two tip/tilt screws is available through the cube face openings. Alignment of the hologram can be checked using the camera software and a test target placed at the focus of the objective.

a) 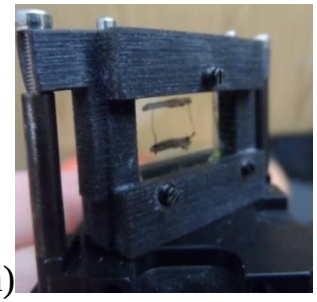 b) 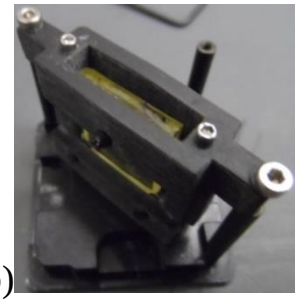 c) 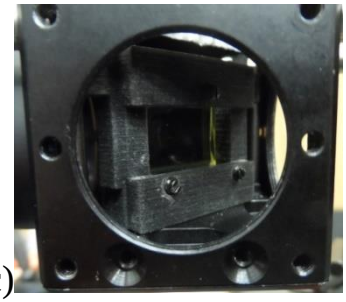
Figure 3.18: Hologram Holder a) back adjustment knobs b) top height adjustment screws c) holder in the cube with the back face toward the camera giving access to the tip/tilt adjustment screws

The endoscope probe is placed into a ThorLabs XY slip plate to allow for better alignment and centering of the endoscope probe to the microscope objective. The slip plate is mounted into a static post holder and remains stationary during the alignment process. Initial

alignment is performed by aligning the slip plate with two cage rods through the pellicle cube and the slip plate. Fine tuning of the x-, y-, and z-axis alignment is performed using the handle XYZ stage shown in Figure 3.19.

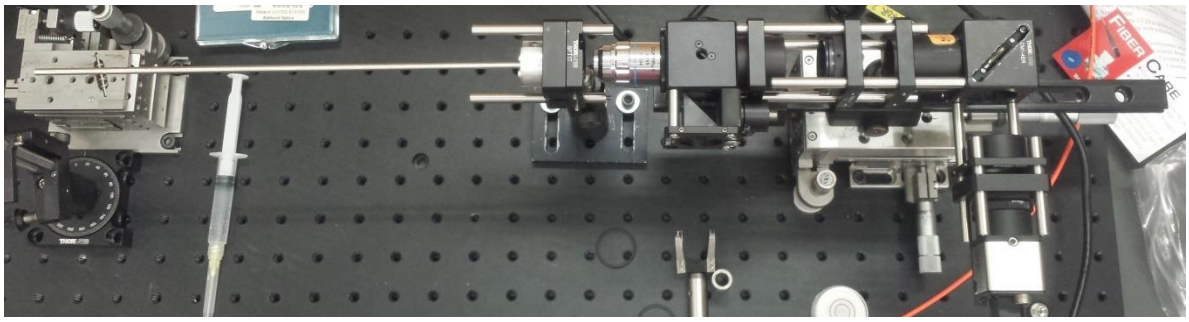

Figure 3.19: Endoscope placement in an XY Slip Plate in a static optical post and mount. The rest of the handle components are allowed to move using a Z-axis stage. The set-up above has the pellicle and illumination fiber rotated 90 degrees, however this does not affect the full noted alignment procedure.

The z-axis stage is used for optical focusing. First, a 1951 USAF resolution chart is placed to be in contact with the distal tip of the probe as shown in Figure 3.20a. The target is on a separate XYZ stage, keeping the probe static as was noted in the previous paragraph. Once the target is placed in contact, the camera is used to check for x-axis and y-axis adjustment of the probe. The diameter of the probe is larger than the view of the system, the adjustments to the XY stage is placed such that the edges of the probe are not seen and some light through the system can be detected.

After this initial adjustment, the focus can be adjusted by moving the objective relative to the probe with the z-axis stage. If an element on the bar target is not detected, the bar target may need to be moved to place a target in the field. Once a target is seen, the z-axis stage is adjusted until best focus is reached. Full alignment will take some time as placement of the probe is adjusted and well centered. Group 7 on the target is used for fine tuning and is later used for resolution characterization. The full system and set-up is shown in Figure 3.20b.

a B

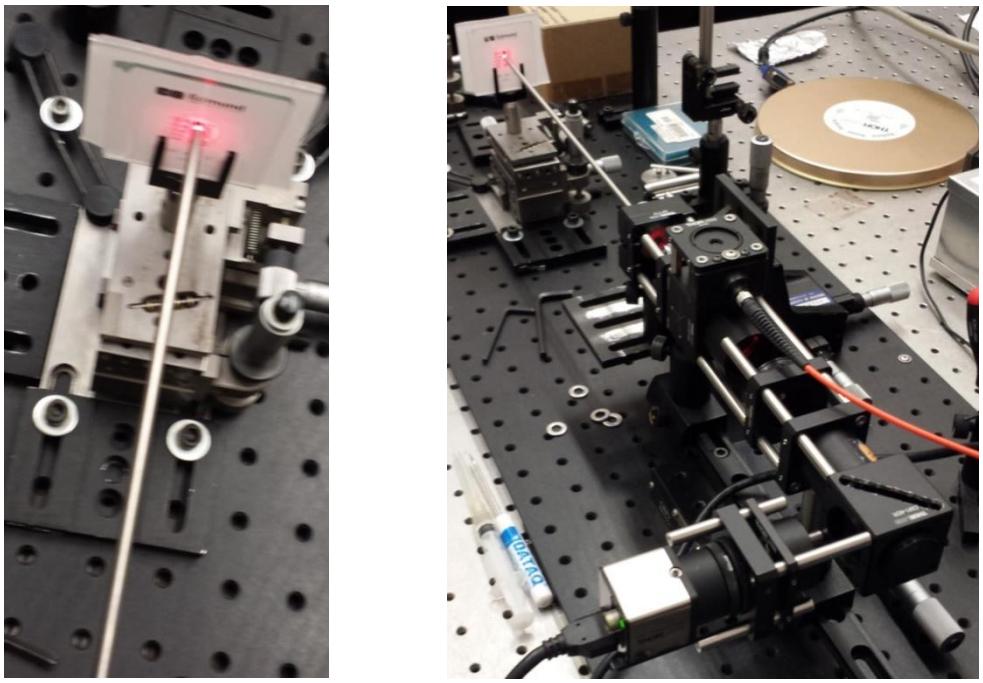

Figure 3.20: a) placement of the bar target in contact with the probe b) full system showing access to the z-position knob for all components to the right of the endoscope probe.

3.4 Optical Testing

Several steps were taken to determine the image quality and resolution of the system. In the following sections the image resolution is evaluated by a visual assessment of a UASF 1951 resolution chart and through contrast measurements.

3.4.1 Evaluation of Image Performance

The first test of the system was performed with a USAF 1951 resolution chart. This style of target is a series of lines with varying widths. The bar targets are generally constructed as chrome features on glass, but can also be provided in negative or fluorescent formats. The negative configuration uses chrome plating on a glass substrate and the targets are areas without chrome plating. The fluorescent targets are chrome features on a glass substrate coated with a fluorescent paint. The feature sizes are broken down into group numbers, with each group

consisting of 6 elements. The resolution, provided in line pair per mm is calculated using the following equation: $Resolution\left(\frac{lp}{mm}\right) = 2^{Group+\frac{element-1}{6}}$. The width of each line is related to the resolution by taking the inverse. Table 3.9 provides the resolution (lp/mm) and line pair width in microns for Group 6 through Group 9.

Table 3.9: 1951 USAF Resolution Chart. Values for the target are provided in resolution units of line pair (lp) per mm and size in microns per line par

Group→	**6**		**7**		**8**		**9**	
Element ↓	**lp/mm**	**µm/lp**	**lp/mm**	**µm/lp**	**lp/mm**	**µm/lp**	**lp/mm**	**µm/lp**
1	64.0	15.63	128.0	7.81	256.0	3.91	512.0	1.95
2	71.8	13.92	143.7	6.96	287.4	3.48	574.7	1.74
3	80.6	12.40	161.3	6.20	322.5	3.10	645.1	1.55
4	90.5	11.05	181.0	5.52	362.0	2.76		
5	101.6	9.84	203.2	4.92	406.4	2.46		
6	114.0	8.77	228.1	4.38	456.1	2.19		

The USAF resolution chart is widely used to provide the resolution criteria for optical systems using various determination criteria. The main evaluation used for this process is a visual evaluation though other methods exist, such as the slanted edge or contrast transfer function (CTF) methods. The CTF method calculates a contrast value and related this value to the modulation transfer function (MTF) through a conversion proportional to $\pi/4$ [47].

The handle was the first part of the system to be measured for resolution performance, without aberration introduction from the hologram or endoscope assembly. This measurement provided the baseline for the best possible imaging situation and evaluated the alignment of the handle optics. Figure 3.21 shows a handle resolution of Group 9, Element 3 with a line width of 0.78 µm (1.55 µm/lp). This shows that the system was functioning as designed for the Nyquist criteria for the chosen magnification.

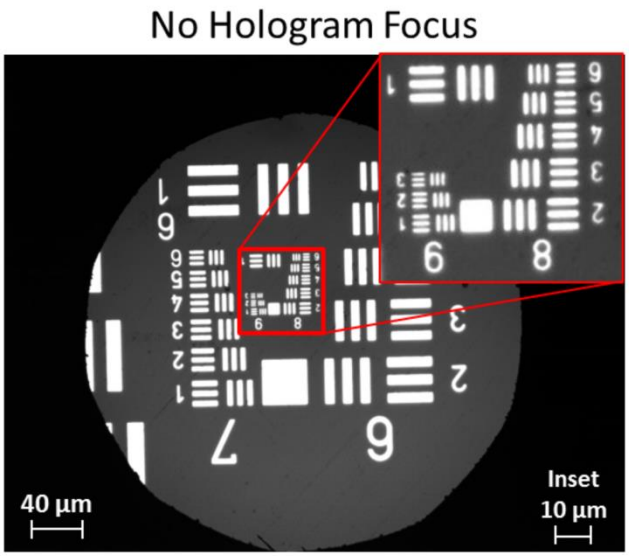

Figure 3.21: Image test of the handle components to verify system alignment before placement of the hologram and endoscope probe

The endoscope and handle components were then introduced to the system and aligned for image acquisition. The images collected by the assembled system are shown in Figure 3.22. The surface channel focus was set while the target was in contact with the endoscope probe. Water was used as an index matching fluid to mimic the operating environment. With the focus set, the target was moved away from the probe using the target z-axis stage. Repeated measurements of the focus from surface to depth provide a depth separation measurement of 50 µm as expected based on the hologram recording geometry.

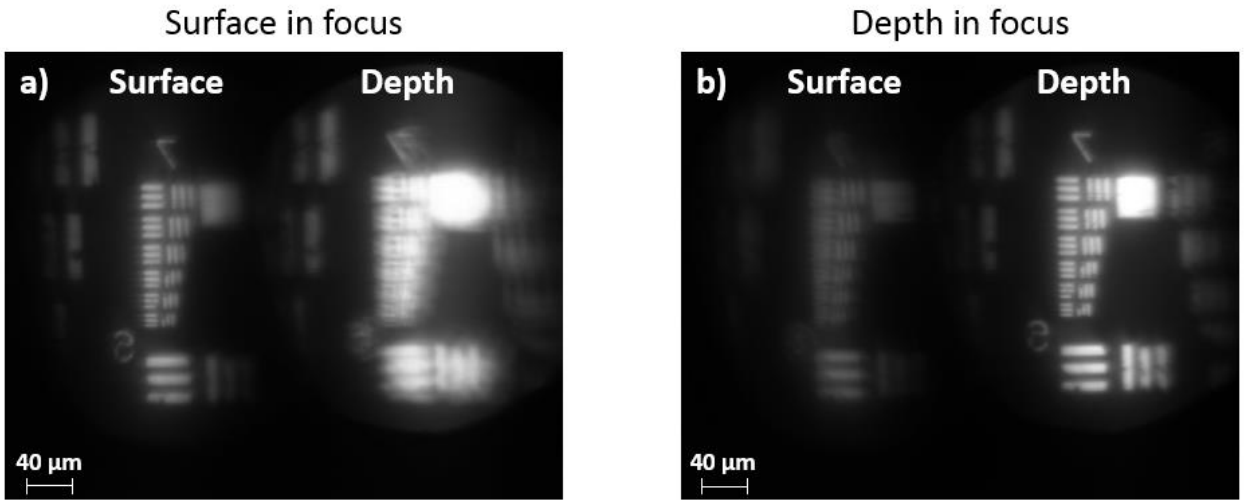

Figure 3.22: US Air Force Bar Target – Surface and Depth focus regions showing 4.4 µm or better resolution a) Surface channel is in focus b) depth channel (Δ = 50 µm) is in focus

Using visual determination of resolution, the image in Figure 3.22 provides 228.1 lp/mm resolutions (Group 7, Element6) for both the surface and depth channels. When evaluating with a high resolution bar target, the next highest resolution of 256 lp/mm (Group 8, Element 1) is not able to be visually resolved. The resolution of the system was stated to fall between 228.1 lp/mm and 256 lp/mm. Although the 228.1 lp/mm resolution relates to 4.38 µm per line pair, since we do not know the exact cut off, we were able to say that the resolution is close enough to fitting the system requirements of 4 µm per line pair (2 µm features).

The bar targets in Figure 3.22 were also evaluated using contrast measurements through the degenerate (y-) axis. The bar target is determined to be resolved when the contrast value of the bar target is above 10%. Contrast, $C = \frac{I_{max} - I_{min}}{I_{max} + I_{min}}$, values for the Group 7 elements are shown in Figure 3.23. The contrast was determined from an average of slices through the bar target, such that anomalies and stray values are less critical on the measurement. The values for the image provided here, are based on the measurement of the y-axis targets only, this is done since the

level of visual resolution is similar for both vertical and horizontal bar targets. When imaging the next group of targets, the elements in Group 8 were not able to be visually resolved and were not tested for contrast measurements. The lowest contrast is 14% meeting the 10% criteria for resolution.

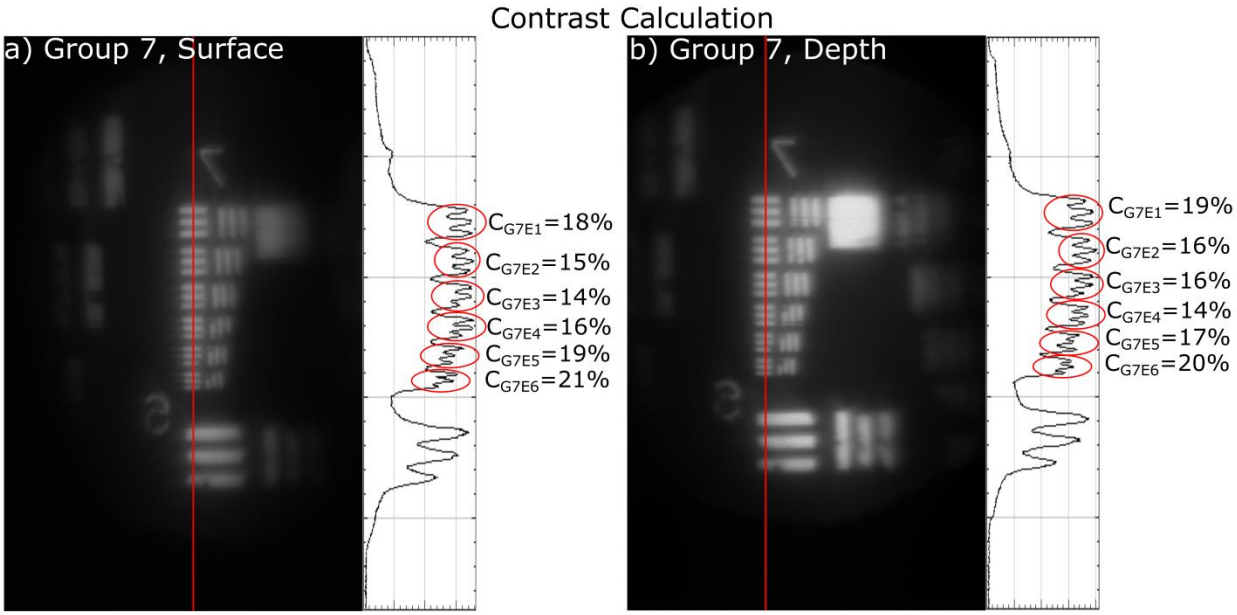

Figure 3.23: Contrast calculation measurements for the Group 7 elements for the a) surface and b) depth channels.

3.4.2 Evaluation of System Aberrations (Tilt and FC)

During evaluation of the system images, it was noticed that the image of the bar target was not in focus for all positions across the x-axis. The focus of the system was adjusted to provide the best focus at the center of the field. Looking across the x-axis of the image, defocus can be seen.

A test to determine the amount of focus change across the x-axis was performed by setting the best focus position at the far right of the image and then translating the test target across the x-axis and readjusting the focus. The data in Figure 3.24 shows an average for the micrometer value that gave the best focus at different locations in the image plane. This plot

shows that the focus position is not constant and has a 55 µm shift across the image plane. The source of this error is a combination of the dispersion of the holographic element and chromatic dispersion from the GRIN assembly.

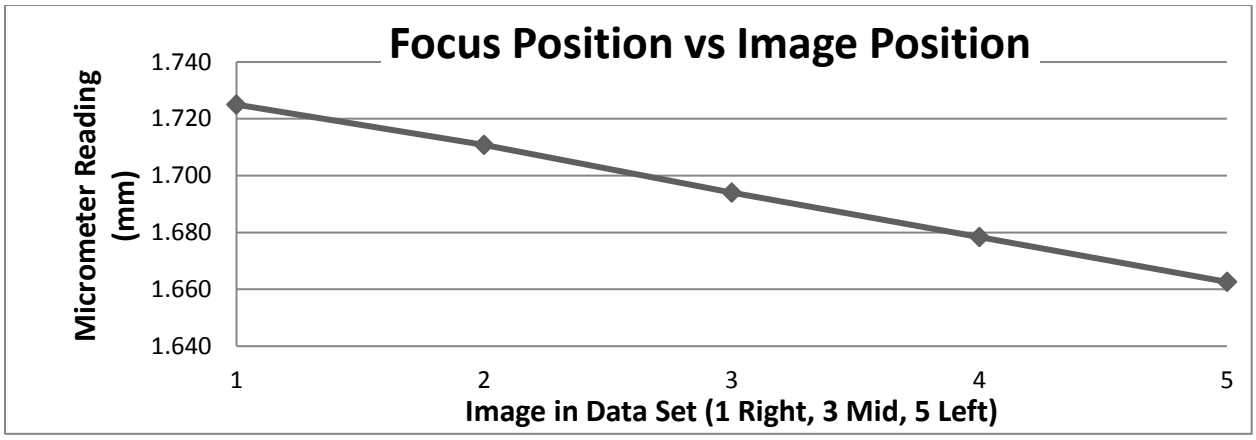

Figure 3.24: Tilt Data measured by moving the test target from the right of the image to the left of the image and evaluating focus change. A total focus shift of 55µm is measured.

The hologram angular and wavelength selectivity are determined from the detuning parameter, calculated using $\vartheta \approx \frac{2\pi}{\Lambda}\left[\Delta\theta \sin(\phi - \theta_o) - \frac{\Delta\lambda}{2n\Lambda}\right]$[11]. In this equation, Δθ and Δλ are the angular and wavelength deviations from the hologram Bragg condition that causes the diffraction efficiency to decrease to zero.

The GRIN assembly produces an axial chromatic focal shift for the spectrum of the LED source. However, it was determined that although there is a relatively large effect with a 2D planar target, the 3D tissue structure will have enough variation within the field that the focus change is not a major concern in practical viewing situations.

3.5 Ex-Vivo Imaging

Prior to utilizing the system for in-vivo procedures, a series of imaging tests were performed to verify image quality. The ex-vivo testing was performed with phantom tissue structures, organic

tissue samples and biological specimens. Each target type provides information on how well the system will work during in-vivo evaluation. All images are post-processed using a rolling ball radius background subtraction method with sliding paraboloid design in the ImageJ software[48].

3.5.1 Tissue Phantom Materials

The phantom tissue structure is a lab made sample consisting of a polyvinyl alcohol (PVA) substrate with embedded polystyrene spheres. The PVA substrate, after preparation using a freeze-thaw method, has an approximate index of refraction of 1.36[49]. The polystyrene spheres, purchased from Invitrogen, have an approximate index of refraction of 1.55. Two types of beads are embedded, half with fluorescence at 670 nm and the other have at 515 nm, both having a diameter of 15 μm. The preparation of the sample allows for the scattering coefficient and stiffness to increase through a repetitive freeze/thaw cycling procedure, for this case a structure resembling the scattering behavior of ovarian tissue.

When imaging with the tissue phantoms, it is necessary to consider the random placement of the polystyrene beads within the PVA material. The bead placement led to different imaging configurations, such as when the bead is at the surface and is in focus, when the bead is at a mid-plane and equally out of focus for both imaging channels, and when the bead is at the depth focus, these conditions are depicted in Figure 3.25.

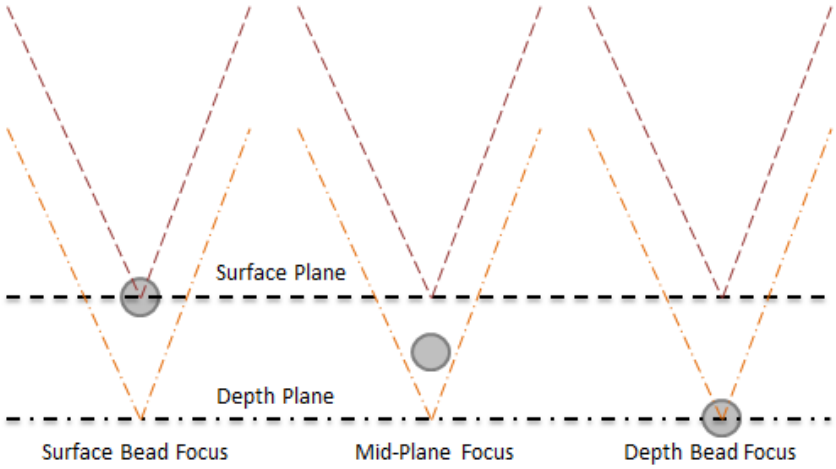

Figure 3.25: Demonstration of bead locations for surface focus, mid-plane, and depth focus.

An example of an image when the beads are located at the Mid-Plane is shown in Figure 3.26. The differences between the surface and depth channels are not well defined with only minor changes in edge sharpness but no ideal edge imaging conditions.

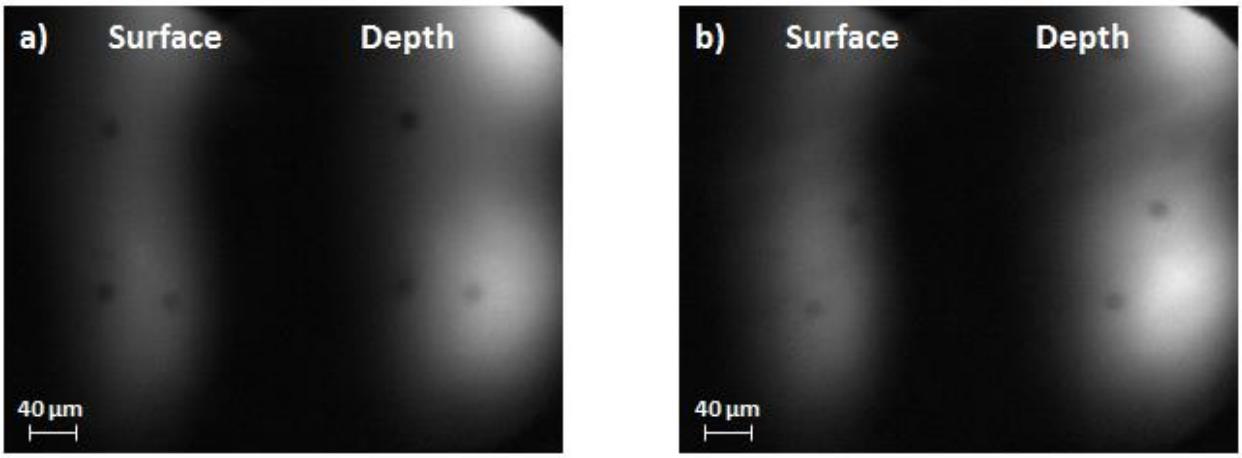

Figure 3.26: Two sites on a Poly-Vinyl Alcohol scattering target with 15 µm polystyrene microspheres showing minimal change in the view due to beads being equally out of focus for both surface and depth focus.

To see the changes between the surface and the depth channels, the focus of the system was adjusted to show variations in bead depths in the PVA sample. This is shown in Figure 3.27. The sample was positioned and the focus of the microscope objective relative to the endoscope probe was adjusted to achieve focus for a specific bead in the image. Figure 3.27 shows that the

bead in the red circle was in focus for the surface but not seen in the depth red circle. The beads in the green ellipse in the surface and depth were closer to being in focus for the depth channel but can be faintly seen in the surface image. The focus was then adjusted to focus for the depth channel. Figure 3.27b shows the same bead from Figure 3.27a now in focus in the red circle in the depth channel. Now the green ellipse in the depth channel has two beads in slightly better focus and the surface channel has no visible beads. These variations show the depth selectivity of the hologram more clearly than relying solely on the bead phantom location as discussed in Figure 3.26.

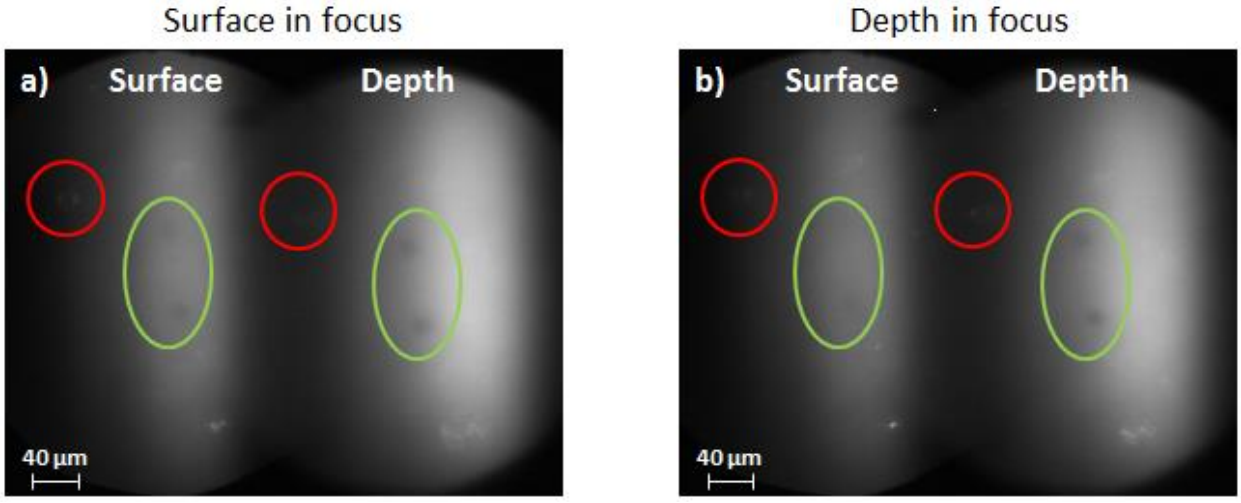

Figure 3.27: The same site of the Poly-Vinyl Alcohol scattering target material and 15 µm polystyrene microspheres.

The bead phantom imaging allowed for testing of depth selectivity and imaging of a known sample with ideal feature size and shape. To test the functionality of the imaging system with cellular structures, onion skin and biopsied human fat were selected. The following sections will detail this imaging method and the results of the image collection.

3.5.2 Plant Imaging

A test of plant tissue was performed to identify the VHI characterization of cellular structures. The plant sample of choice was onion (Allium cepa L.) due to large cell structures with a recognizable elongated rectangular shape. Onion cells are roughly 75 µm in width and 150 µm in length. The index of refraction of the onion sample is assumed to be in the range of 1.3345 to 1.3450 based on studies of onion skin absorption and scattering properties and other plant cell wall studies[50,51].

When evaluating the image of the onion skin shown in Figure 3.28, the two images both show a well imaged cellular wall for the focused region. The variation is not significantly different between the surface and depth channel image. The change in structure is assumed to be due to the depth of the onion cell being greater than 50 µm which means the depth separation is not enough to reach the next layer of cells. The intensity variation of the edges in the depth channel is due to the hologram efficiency in the depth channel being higher than that of the surface channel.

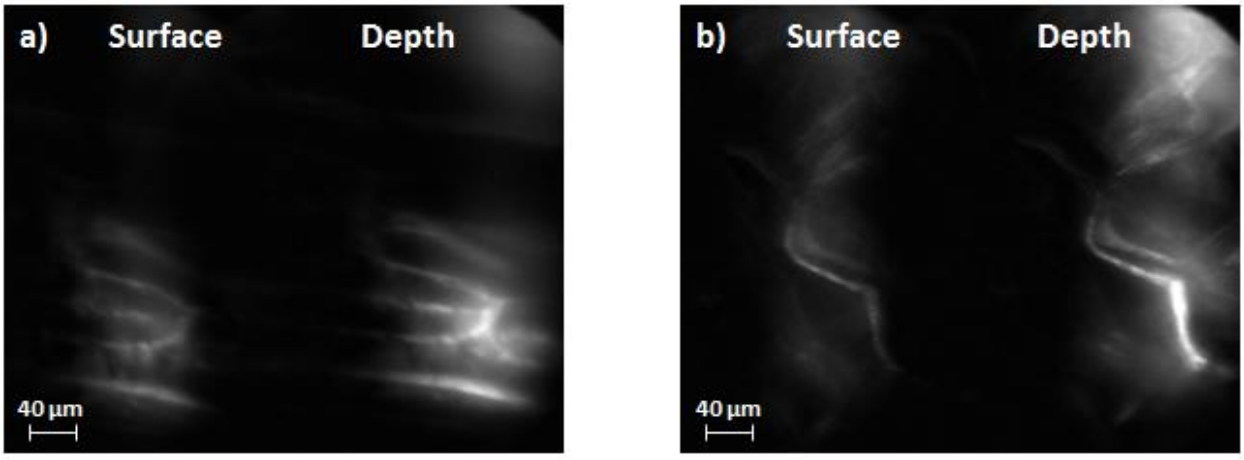

Figure 3.28: Onion Skin images taken at two locations on the onion sample using the endoscope probe

Measurement of contrast along the y-axis of Figure 3.28b provides additional imaging characterization of the system. The main features selected, demonstrated by the red vertical line in the surface and depth channels, have contrast values between 26% and 58% in the surface image and 45%-46% in the depth image.

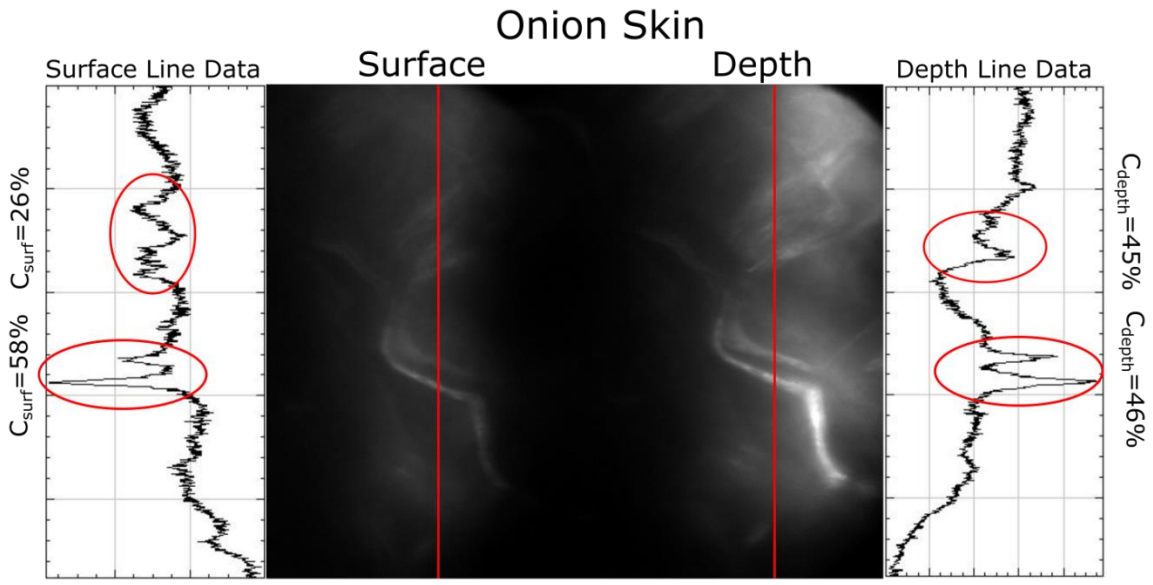

Figure 3.29: Onion Skin Contrast Measurement

3.5.3 Human Tissue Samples

The last ex-vivo evaluation was performed on human samples. Although many types of tissue structures were attempted to be imaged, the best images were obtained from adipose (fat) tissues. The index of refraction of the adipose tissue is assumed to be near 1.45 which is the noted index of refraction for lipids[49].

Figure 3.30 is able to show the identifiable circular cellular structure of fat cells. On average, fat cells are between 80 µm and 200 µm in diameter. The variation from surface to depth is again minimal which can be attributed to the thickness of the cells. However, due to the

round shape of the cells, more change may be expected in the overall diameter as the image would transverse 50 µm within the sample.

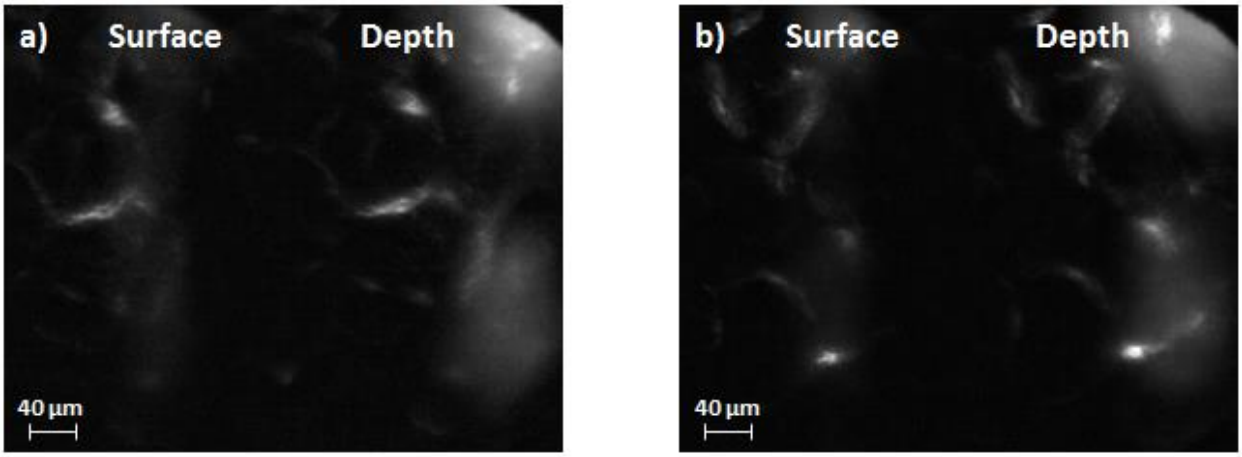

Figure 3.30: Images of a Human Ovary sample, images show high contrast and definition of the adipose tissue

Measurement of contrast along the y-axis of Figure 3.30b, shown in Figure 3.31, measures contrast values between 34% and 72% in the surface image and 50%-64% in the depth image.

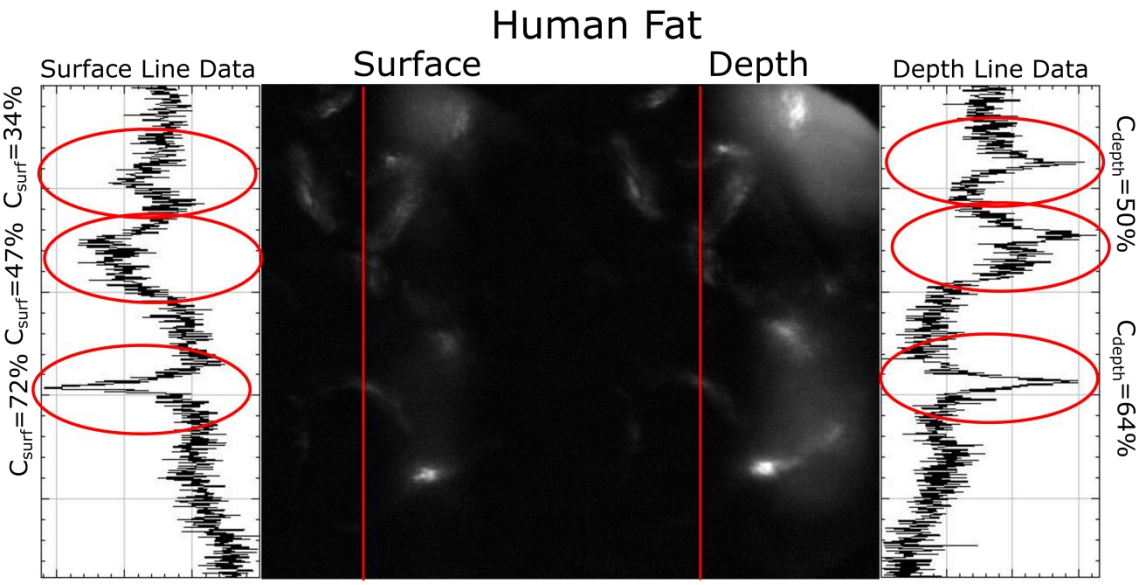

Figure 3.31: Human Fat Contrast Measurement

3.5.4 System Limitations

The end goal for the development of endoscopic VHIS devices was to allow for visualization of targeted in-vivo imaging during laparoscopic procedures. The current reflectance endoscope system was utilized in two in-vivo patient studies. However, system limitations required that the in-vivo analysis be cancelled and the research focus be turned to system modifications to improve the imaging performance. There were two main limitations with the imaging performance of the reflectance endoscope. The first is minimal visual differentiation between surface and depth channel images. The second is the inability to image low contrast tissue structures.

Although the depth separation of the two holographic imaging channels was quite clear at 50 μm using a 2D resolution chart, the depth separation becomes less apparent when imaging a 3D sample. When testing the imaging capabilities with the bead phantom samples, the random location of the beads within the media caused some evaluation concerns. The random placement of the beads allowed imaging conditions where beads of interest were equally out of focus for both channels. This yielded an image that was not significantly different for the two channels. For the organic samples, both the onion and the fat tissue provided large cell sizes, however the depth of these samples is greater than 50 μm. Many of the issues of the lack of change between the channels may be able to be attributed to small changes over this short separation distance within the cell body since the cells have thicknesses of 100 μm or larger.

A method to test the theory that a 50 μm depth separation is too minimal to be able to see large depth variation is to increase the hologram channel depth separation. This can be done

through the recording of different wavefronts in the hologram or through a means of separating the focus of the endoscope probe through the use of axial chromatic dispersion and multiple light sources. This latter method is explored in Chapter 4.

The second challenge of the system is a decreased ability to image tissues with low contrast. The imaging contrast has a larger relationship to the index mismatch of the cell walls and bulk material, than to the absorption and bulk scattering of the tissue[52–55]. The bead phantoms, onion skin, and fat tissue are all examples of high contrast materials. For these cases the cell edges and features were easy to see and determine from the resulting images. When imaging low contrast tissues the signal variation between a feature and the surrounding tissue is similar in reflectance values. Additionally, the background light from the system was also washing out detail of the collected sample image.

There are various methods to improve the contrast, some which involve contrast agents. Since the system would ideally be used in an in-vivo clinical setting, the use of approved dyes would be preferred; however few dyes and stains are available at the wavelength of 660 nm. A previous method used in VHI technique is a wavelength coded method which utilized two wavelengths in the system, where each peak wavelength would have a corresponding holographic multiplexed channel[19,56]. This method will eliminate crosstalk between the holographic channels and reduce some of the background light caused by the channel crosstalk. With this background signal removed, it could be possible to see features which may have been hidden in the background noise of the image. This will be tested as part of the wavelength coded endoscope design in Chapter 4.

3.6 Summary

In this chapter, a reflectance volume holographic endoscope system was described. The endoscope was designed to use Gradient Index optical components using a triplet design. The overall diameter of the volume holographic imaging endoscope was 3.8 mm, meeting the less than 5 mm requirement. The optical evaluation of the system, revealed the capability of clearly imaging a 228.1 lp/mm resolution bar target with 660 nm Köhler illumination. The design requirement was to image a 250 lp/mm target (2 µm features). After conversion into feature size, 228.1 lp/mm relates to a 2.2 µm feature, which is reasonably close to the 2 µm size. The FOV requirement was not met, with the system falling short of the 500 µm x 1000 µm original requirement with an actual FOV of 394 µm x 246 µm tissue section. System performance is assessed through imaging of USAF resolution charts and both fabricated and organic soft tissue targets. This initial test of the system shows limitations in the ability to image low contrast tissue structures. Further development of the technique and modifications to the illumination and holographic methods can lead to improved imaging capabilities.

Chapter 4
Wavelength Coded VHI Endoscope

4.1 Introduction

The reflectance mode VHI system presented in Chapter 3 uses a single illumination source in combination with a multiplexed volume hologram. The hologram in this case is recorded with an object beam that originates from different tissue depths and results in a different grating curvature for each depth. Since the holograms are recorded at 514.5 nm and are reconstructed at 660 nm, increased aberration content is observed for the curved hologram grating profiles. These aberrations limit lateral resolution. One approach to correcting this problem is to use a different optical mechanism to separate the object depths and planar grating holograms to separate the two images. Planar grating holograms can be perfectly matched across the aperture when reconstructed at a wavelength that differs from the construction wavelength by adjusting the reconstruction angles. In this Chapter the design of a wavelength coded VHI system that uses axial chromatic aberration to separate light coming from two object depths in combination with two optical LEDs with different nominal wavelengths is presented. As will be shown this allows planar grating volume holographic elements to be used that lower lateral aberration. In addition, the output power of each source can be separately adjusted to compensate for intensity differences of the two imaging channels. A journal publication on wavelength coded volume holographic imaging (WC-VHI) system is given in Appendix A.2.

4.1.1 Wavelength Coded Design in Benchtop Systems

The wavelength coded VHI (WC-VHI) endoscope uses the same endoscope and handle optics as described in Chapter 3. The main modifications to the design were made to the holographic

element. The updated operating parameters made use of the chromatic behavior of the GRIN probe to achieve the image depth separation. The WC-VHI relies on planar holographic elements to separate the depths spatially and spectrally onto the camera.

This method is an adaptation of a wavelength coded volume holographic imaging approach developed by Luo et. al.[19,56] for benchtop systems. The design uses two or more light sources with wavelengths separated for minimal overlap of the spectra. This wavelength separation allows for separation of the two imaging channels at the camera plane resulting in improved image contrast. In the cases provided by Luo et. al. in 2010 and 2011, the hologram design utilized two multiplexed holograms with curved grating profiles that sampled light with wavefront curvatures that originate from different object depths. In this case all depth selectivity was performed by the holographic element.

4.1.2 Axial Chromatic Dispersion

In this work, the WC-VHI was modified to use the axial chromatic dispersion of the GRIN elements in the endoscope probe to provide depth separation of the images. Typically, axial chromatic dispersion is corrected to remove wavelength dependent focus effects. However, some confocal systems have started to utilize axial chromatic dispersion as a mechanism for imaging at specific tissue depths. Lane et. al. and Olsovsky et. al. have both presented miniature GRIN lenses which introduce chromatic sectioning behavior into confocal imaging systems[57,58]. The chromatic sectioning behavior occurs as light propagates through the GRIN element. As the wavelength of the source changes, the focal point shifts within the tissue sample. Making use of

this focal shift provides some depth selectivity for confocal imaging systems and removes the requirement for mechanical axial scanning from these systems.

4.2 Wavelength Coded VHI Endoscope Design

The combination of wavelength coded volume holographic system techniques and axial chromatic dispersion is a logical next step for the development of the reflectance VHI endoscope. The WC-VHI endoscope system utilizes the same principles as used in the chromatic confocal imaging systems. This was able to be performed since the existing GRIN probe displayed axial chromatic focus effects. The wavelength coded methods in VHI benchtop systems have provided a means of better contrast and less wavelength crosstalk. Merging these two techniques will give a partial solution to the system limitations of the reflectance VHI endoscope described in Chapter 3. This section will highlight the changes made during the conversion from the reflectance VHI endoscope to the wavelength coded VHI endoscope.

4.2.1 Optical Source Selection

Two LED sources with a FWHM spectral bandwidth of 20 nm with peaks wavelength values of 660 nm and 730 nm were selected for use in the WC-VHI system. The peak wavelengths of these two sources were sufficiently separated to minimize spectral overlap (Figure 4.1) so that the Bragg selectivity of each hologram only diffracts light from one source. Both sources were rated to have 1 to 3 Watts of output power from the LED.

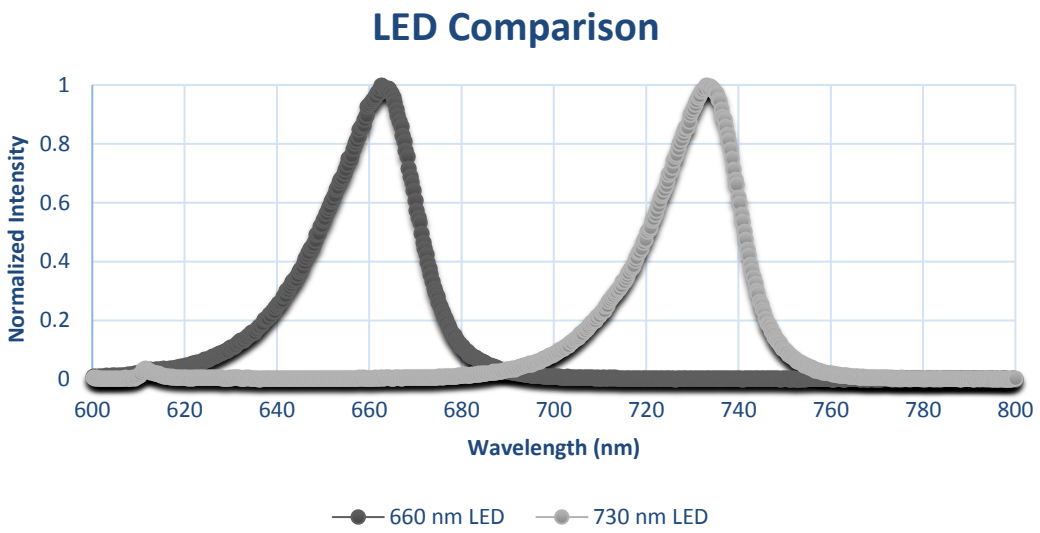

Figure 4.1: LED Source Comparison of FWHM and Peak Values. Dark data has a peak of 662 nm, Light data has a peak of 732 nm. Both sources have a FWHM of 20 nm.

4.2.2 Measurement of Axial Chromatic Dispersion

The endoscope probe, as discussed previously, was built using three GRIN elements in addition to distal and proximal windows. After propagating through the system, the 660 nm light was set to image light from the surface of an object while the 730 nm light was used for imaging the depth layer of the object. The measured separation between the 660 nm and 730 nm foci due to axial chromatic dispersion is 100 µm which is twice the depth separation of the reflectance VHI endoscope.

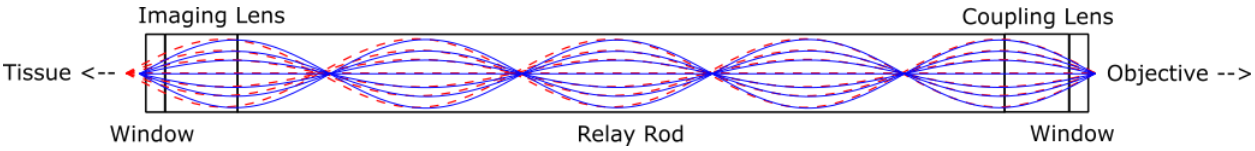

Figure 4.2: Schematic of the GRIN endoscope behavior of focused light at two wavelengths. Red corresponding to 730 nm light and blue corresponding to 660 nm light.

It is important to note is that light from the two focal points for light at each wavelength will focus at the same axial position prior to the microscope objective. This results from the axial

chromatic dispersion of the probe. After passing through the microscope objective, the light from both depths is collimated but at separate wavelengths. The depth information can now be separated with two multiplexed planar gratings: one for the 660 nm light and one for the 730 nm light. The wavelength selectivity of the volume holograms is high enough to unambiguously separate the two fields without the need for curvature in the hologram. In addition, since the planar holograms have a single K- vector across the aperture, they can be reconstructed at a wavelength that differs from the construction wavelength without aberration. This results in higher lateral resolution of the system.

4.2.3 Hologram Design

The volume holographic element used in the wavelength coded VHI endoscope system was designed for use with planar wavefronts for the 660 nm and 730 nm source wavelengths. This is a simplification compared to the reflectance VHI endoscope design which required a change in the point source location for each imaging channel.

The WC volume holographic element was recorded in a 1.8 mm thick piece of PQ-PMMA with 514.5 nm light from a Coherent Innova 300 Argon laser. During the recording process, the object beam was set to 33° and 30° in air relative to the normal of the hologram surface for the surface and depth recordings respectively. The reference beam angles for the surface and depth channels were 34.8° and 28.6°, respectively. These construction angles resulted in an inter beam angle of 90° between the object and reference beams during reconstruction. The measured diffraction efficiencies, at 633 nm, were 27% and 50% for the surface and depth holograms respectively. After converting this value to the design wavelengths

of 660 nm and 730 nm the diffraction efficiencies become 26% and 39% for the surface and depth channels, respectively. To ensure equal channel intensities on the camera, the individual LED power can be adjusted, this is discussed in the next section. A list of hologram specifications are provided in Table 4.1.

Table 4.1: Wavelength Coded hologram design specifications and post-recording parameters

Design Specifications		
	Surface	**Depth**
Recording Wavelength	514.5 nm	
Material	PQ-PMMA	
% PQ	0.5%	
Thickness	d = 1.8 mm	
Index of Refraction	n = 1.49	
Grating Period	$\Lambda_{surface}$ =460.8 nm	Λ_{depth} = 525.2 nm
Q parameter	$Q_{surface}$ = 23592	Q_{depth} = 18164
Object Beam Angle	$\lvert\theta_{DepthObj}\rvert$ = 33°	$\lvert\theta_{DepthObj}\rvert$ = 30°
Reference Beam Angles	$\lvert\theta_{SurfaceRef}\rvert$ = 34.8°	$\lvert\theta_{DeothRef}\rvert$ = 28.6°
Post-recording Parameters		
Replay Wavelength	660 nm	730 nm
Inter Beam Angle	90°	
Exposure Density	2765 ms/cm^2	2488 ms/cm^2
Diffraction Efficiency (η) at 633 nm	$\eta_{surface}$ = 27%	η_{depth} = 50%
Calculated η at Reconstruction λ	$\eta_{surface}$ = 26%	η_{depth} = 39%

4.3 Illumination Optics

The WC-VHI endoscope system requires that two LED sources be coupled into a single fiber source in order to use the illumination path of the reflectance VHI system. Keeping the illumination path, as described in Chapter 3.2.2.2, allows for the fiber output to be imaged to the microscope objective pupil for Köhler illumination. The challenge with the WC-VHI fiber illumination is the coupling of the sources into the input of the fiber. There is expected to be a large loss of light during the process. Since the LEDs are rated for 1W - 3W of power at the face

of the LED, the light loss of coupling into the fiber will aid in the reduction of power to acceptable clinical levels.

The dual wavelength illumination system is shown in Figure 4.3. The LED positions relative to the lenses were adjusted while viewing the light through the system on the camera. Initial alignment was to achieve equal intensity in both the surface and depth channels using the USAF resolution charts as an object. Due to scattering effects and expected signal loss from tissue samples, the system is able to be adjusted to change the source powers individually. By adjusting the LED module settings and/or adjusting the lens to fiber alignment the power of the sources reaching the sample was able to be adjusted to achieve equal illumination for tissue samples. Once the sources were adjusted, the system was tested in the same manner as the reflectance endoscope system using resolution test targets, tissue phantoms, and organic tissue samples.

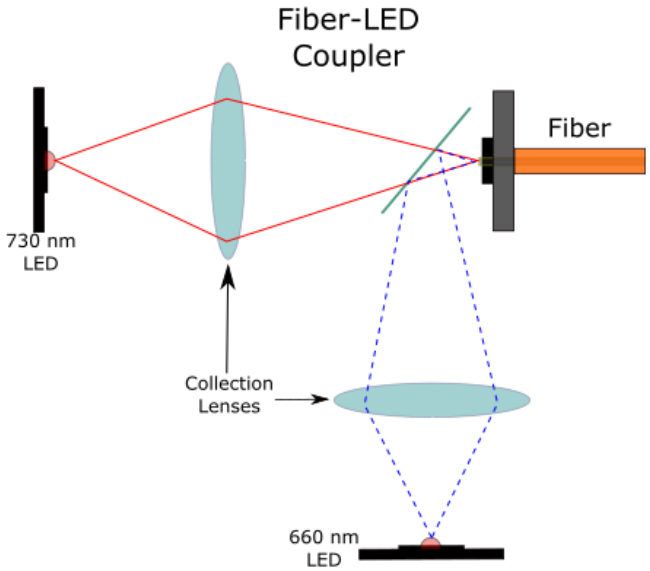

Figure 4.3: LED to fiber coupling using lenses and a beam splitter for the two source wavelength coded VHI endoscope

The calculation of the power being collected by the microscope objective was similar to that of the reflectance VHI in Chapter 3.3.1.1. The power reaching the sample was measured with a power meter to be 140μW and 100μW for the 660 nm and 730 nm sources, respectively. Using these values and the expected reflectance values, used in Chapter 3, the expected power at the microscope objective was 0.14 μW and 0.1 μW for 660 nm and 730 nm sources.

4.4 Optical Testing

The first test of the wavelength coded VHI endoscope system was to verify that the hologram was operating at optimum conditions. This included a test for the field of view, observed channel image shift, and optical resolution.

The observed channel image shift is a property of the hologram reconstruction. If the hologram is not recorded properly a shift in the focused image position in each channel can be detected. If the in focus image at the surface channel is not matched with the focused image in the depth channel the images cannot be well correlated. When a shift in the image focus is present it becomes difficult to determining cellular changes. This was tested by stopping down the aperture between the relay lenses in the handle and imaging a test target. The smaller field created by the stopped down aperture provides a better assessment of focused image positions. Adjusting the focus between the surface and the depth channel showed where each image was focusing axially and laterally for image shift. Figure 4.4 shows how the two channel images shared the same field of view with minimized lateral shift.

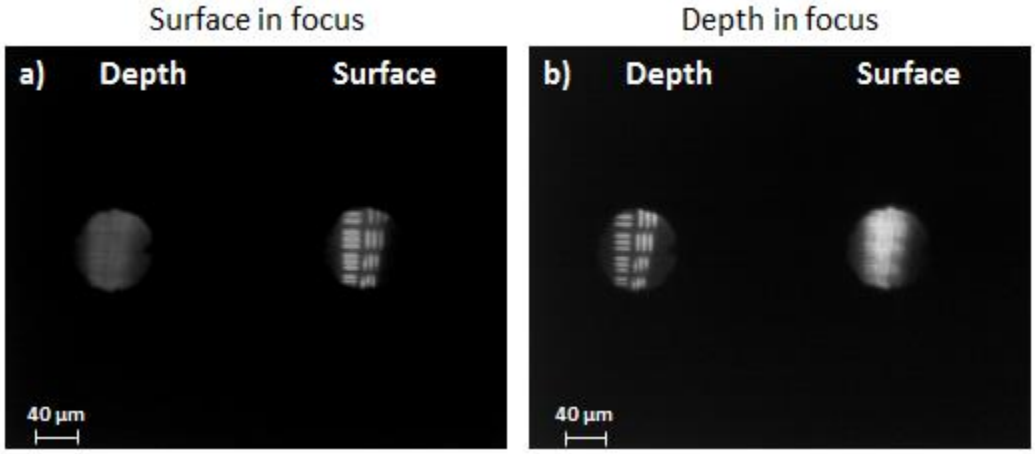

Figure 4.4: Field aperture is narrowed to show that the surface and depth channels are imaging the same region of the sample.

A wavelength coded system is designed to minimize channel crostalk. To verify the hologram's ability to select the wavelengths of interest and reject the undesired wavelengths each source was separately turned on and the images were vieweed individually. Figure 4.5a shows the image of the USAF resolution chart when the 660 nm LED was turned on for the surface channel and Figure 4.5b shows the depth channel image with the 730 nm LED turned on. In both cases the holograms appear to be fully rejecting light from the other channel, which was expected due to the high wavelength selectivity of the 1.8 mm thick volume holograms.

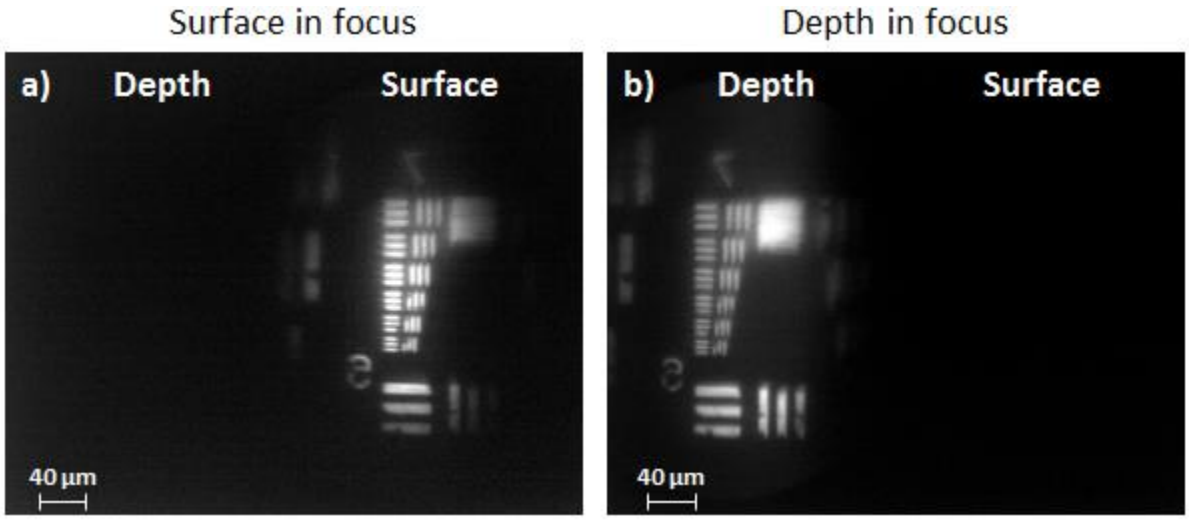

Figure 4.5: Standard 1951 USAF Bar Target Imaging to assess illumination and compare imaging channel illumination. a) 660 nm light source is on the surface in focus only b) 730 nm light at a depth of 100 microns.

4.4.1 Evaluation of Image Performance

A 1951 USAF resolution chart was used to measure the resolution capabilities of the system. As shown in Figure 4.6 a visual resolution of 3.10 µm per line pair (322.5 lp/mm) can be resolved for both the vertical and horizontal bars.

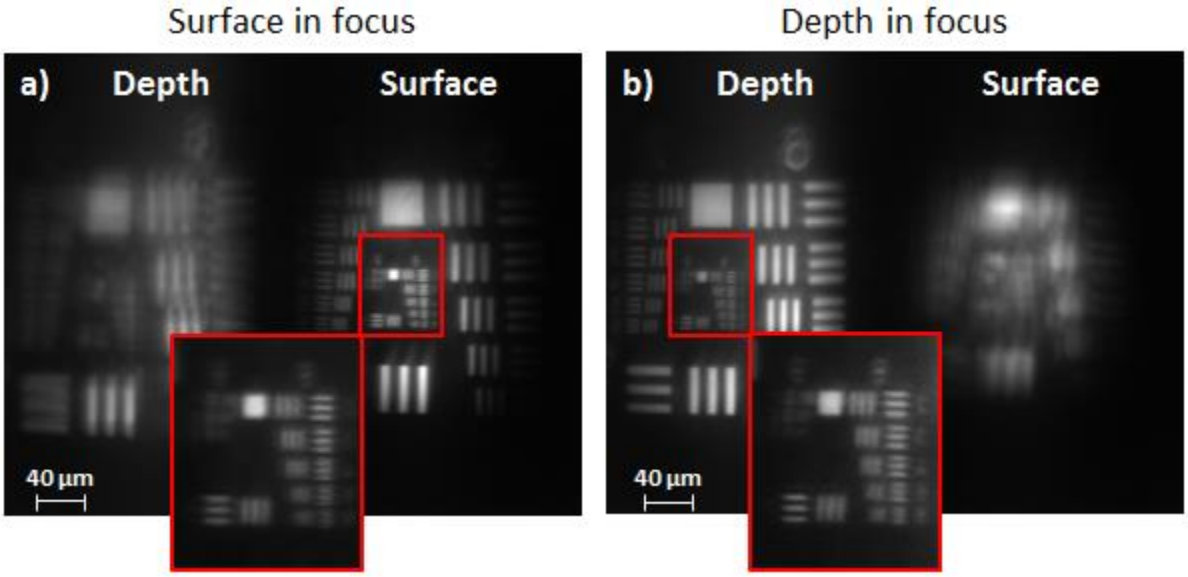

Figure 4.6: Resolution Testing a) 660 nm light on the surface in focus only b) 730 nm light at a depth of 100 microns. Both sources are turned on with the c) surface in focus d) depth in focus. The inset of c) and d) show the detail of the target in the Group 8 elements. The smallest elements are in Group 2, with 3.1 µm/lp (322.5 lp/mm).

A more quantitative evaluation of the resolution was also performed using image contrast of the features in the USAF resolution chart. For this evaluation, both the vertical and horizontal bar targets were evaluated for contrast data since there was a visual difference between the resolution of the Group 8, Element 3 vertical and horizontal targets. The surface and depth contrast calculations are provided in Figure 4.7 which show 10% contrast or higher for the vertical and horizontal bars in the bar target elements of interest. This shows a 1.28 µm/lp (94.5 lp/mm) improvement in the resolution from the reflectance VHI endoscope system. The improvement to lateral resolution results from using planar grating holograms which do not suffer from chromatic aberration when the reconstruction wavelength differs from the construction wavelength.

Surface Contrast Calculation

Surface Contrast		
Group 8	Vertical Bars	Horizontal Bars
Element 1	28%	38%
Element 2	12%	32%
Element 3	10%	20%

Depth Contrast Calculation

Depth Contrast		
Group 8	Vertical Bars	Horizontal Bars
Element 1	22%	58%
Element 2	15%	32%
Element 3	19%	26%

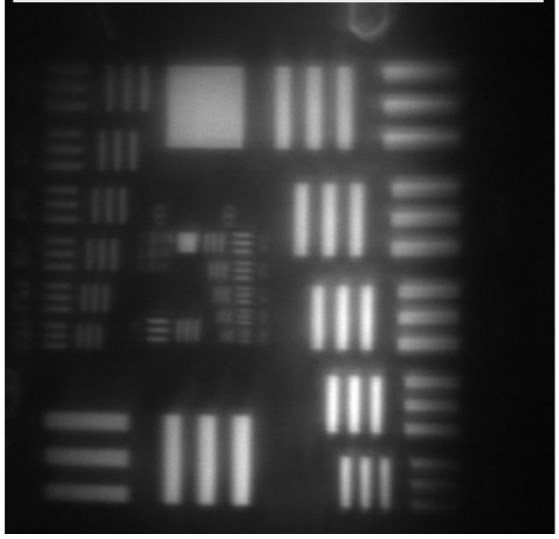

Figure 4.7: Surface and depth contrast measurements for Group 8 elements 1 through 3. The surface and depth images meet the contrast criteria of 10% or higher for Group 8, Element 3, confirming the visual resolution assessment of 3.10 µm per line pair (322.5 lp/mm).

4.5 Ex-Vivo Imaging

Ex-vivo imaging analysis of human like tissue materials provides greater insight into the true performance of the optical system. The samples for ex-vivo evaluation are phantom tissue structures, onion skin, and mouse tissue samples.

4.5.1 Tissue Phantom Materials

The PVA based phantom tissue structures, described in Chapter 3.5.1, were used as a system evaluation tool for the wavelength coded VHI endoscope. Polystyrene beads were randomly placed within the PVA material. The position of the microscope objective relative to the endoscope probe image plane was adjusted until the beads in the surface channel appear in focus. The beads in the depth channel are then known to be 100 μm from this position. Since the depth separation was larger in the WC-VHI than the reflectance configuration, it was easier to note when a bead was in an out of focus plane since there was not a clear middle-focus there was less overlap of bead images as in the reflectance endoscope system. The images taken using the WH-VHI, shown in Figure 4.8, provide in focus images of the surface beads and images of different beads for the depth channel. It should be noted however that the depth channel images have much lower contrast due to scattering through the 100 μm depth.

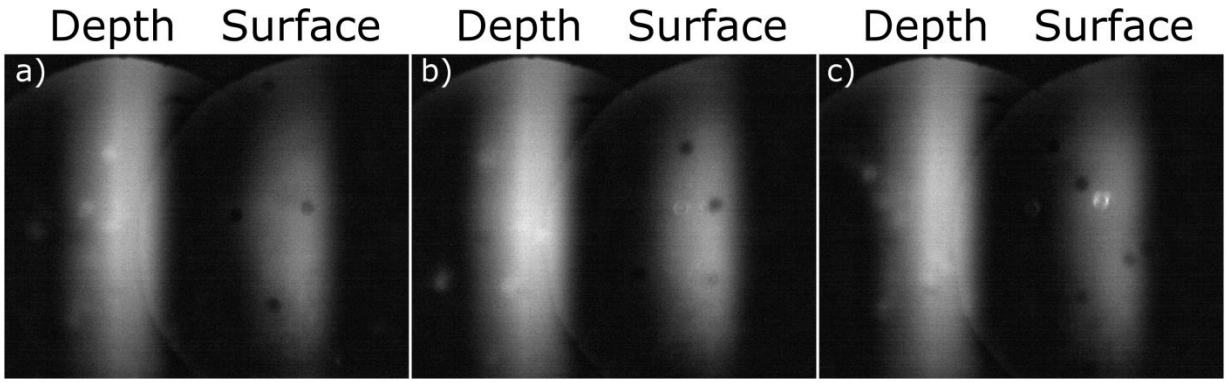

Figure 4.8: Three regions on the PVA sample with embedded polystyrene spheres. Each sub-image has been focus adjusted in order to have a clear in-focus plane at the surface. The depth images are 100 µm deeper into the sample. Although there is not a clear case of an in-focus bead in the depth channel due to the random nature of the bead arrangement, new beads are appearing in the depth channel which were not originally present in the surface channel.

The image of Figure 4.8a) was expanded and evaluated in Figure 4.9 to show how the in-focus bead from the surface is defocused in the depth image. When the surface bead is out of focus there is a lateral shift in position, as shown with the circles in the figure. This shift is a result of chromatic aberration of the GRIN probe focusing the different wavelengths of the LED spectrum at different depths essentially causing a spectral variation in the telecentric properties of the system.

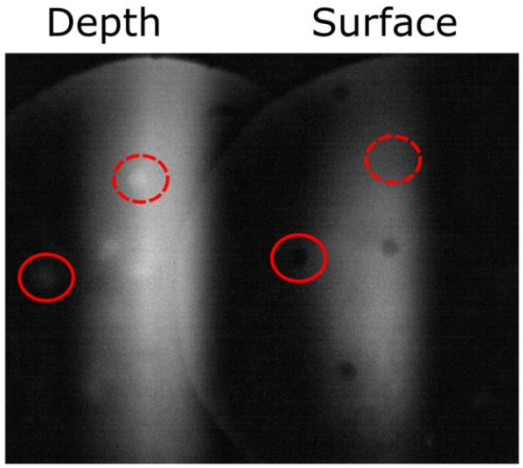

Figure 4.9: Tracking of the in-focus surface bead is shown in the non-dashed circled region. The dashed circle is showing the location of a bead that is appearing in the depth image which was not present in the surface image. Shift of the circles accounts for the shift occurring as an object is moving out of focus.

4.5.2 Plant Tissue Imaging

The WC-VHI endoscope images of onion skin show a clear difference in features between the surface and depth images as shown in Figure 4.10. The depth separation of 100 µm shows a greater change in cellular structure than what was seen with a depth separation of 50 µm in the reflectance endoscope. The images also show that the WC-VHI design had a better balance between the channel illumination intensity. This is possible since each channel corresponds to a different LED allowing the power to be separately adjusted. The depth image contains more scatter and less reflectivity, which requires a greater illumination power for that channel.

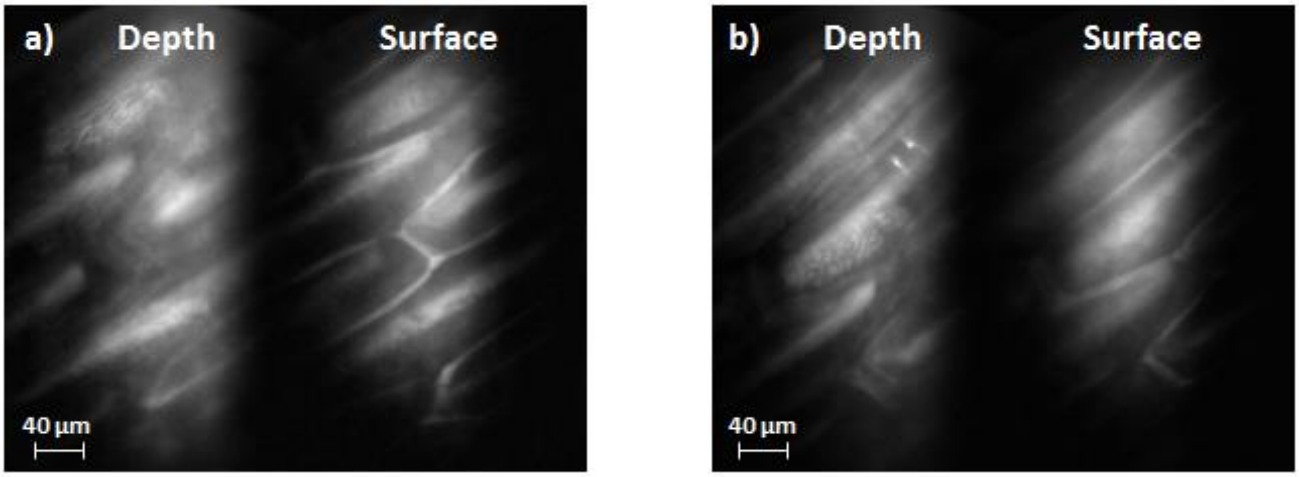

Figure 4.10: Onion imaging using the wavelength coded VHI endoscope. Sub-images a) and b) correspond to different areas on the sample. The surface images provide high detail information of the cellular structure. The depth images start to reveal texture within the cell and the outline of cells deeper into the sample.

Measurement of contrast along the y-axis of Figure 4.10a is shown in Figure 4.11. Contrast values of 26-28% for the selected peaks in the surface channel and 32-53% for the selected peaks in the depth channel were measured.

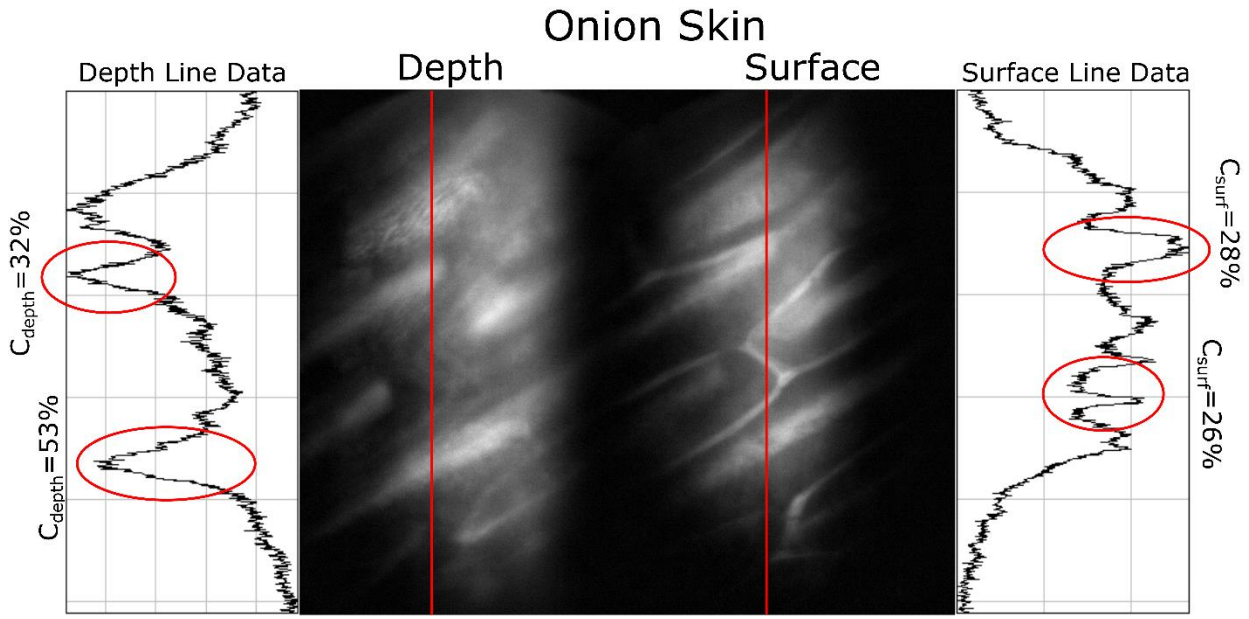

Figure 4.11: Contrast data for an onion sample through regions in the surface and depth channels.

4.5.3 Mouse Tissue Samples

The WC-VHI system was also used for ex-vivo imaging of mouse tissue samples. Below are imaging results for mouse fat, lung and intestine samples. Although other types of tissue types were imaged, including ovaries and fallopian tube samples, the contrast was very low and features were not identifiable.

Figure 4.12 shows the circular cellular structure of mouse fat cells in the surface channel and variation of the cellular structure in the depth image. The fat cells in this image are roughly 60 µm in diameter. Tissue variation from surface to depth is seen as a change of focus for the surface image with additional cellular edges and features coming into focus.

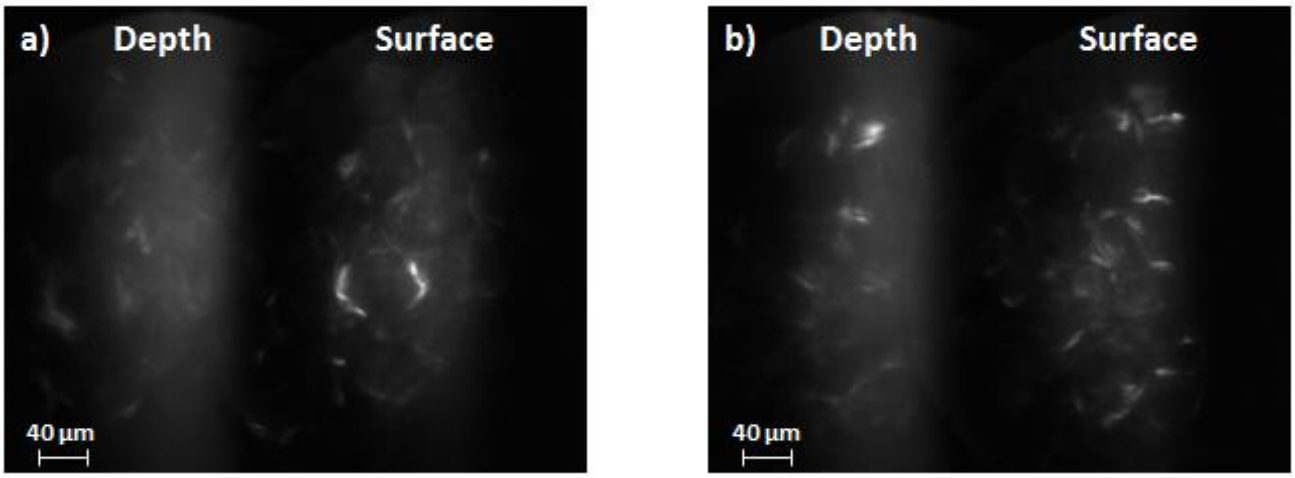

Figure 4.12: Two regions in a sample of mouse fat imaged through the wavelength coded VHI endoscope. Sub-images a) and b) correspond to different areas on the sample. The surface images provide high contrast information of the cellular structure. The depth images start to reveal texture within the cell and the outline of cells deeper into the sample, however a rise in the background light from scatter is seen.

The contrast of the image shown in Figure 4.12a is quantified in Figure 4.13. The red vertical line in each channel indicates a column of sampled pixel values. A contrast value of 67% was measured for the depth channel and 78% for the surface. A greater background intensity fluctuation level can also be seen for the depth channel due to a greater degree of scatter.

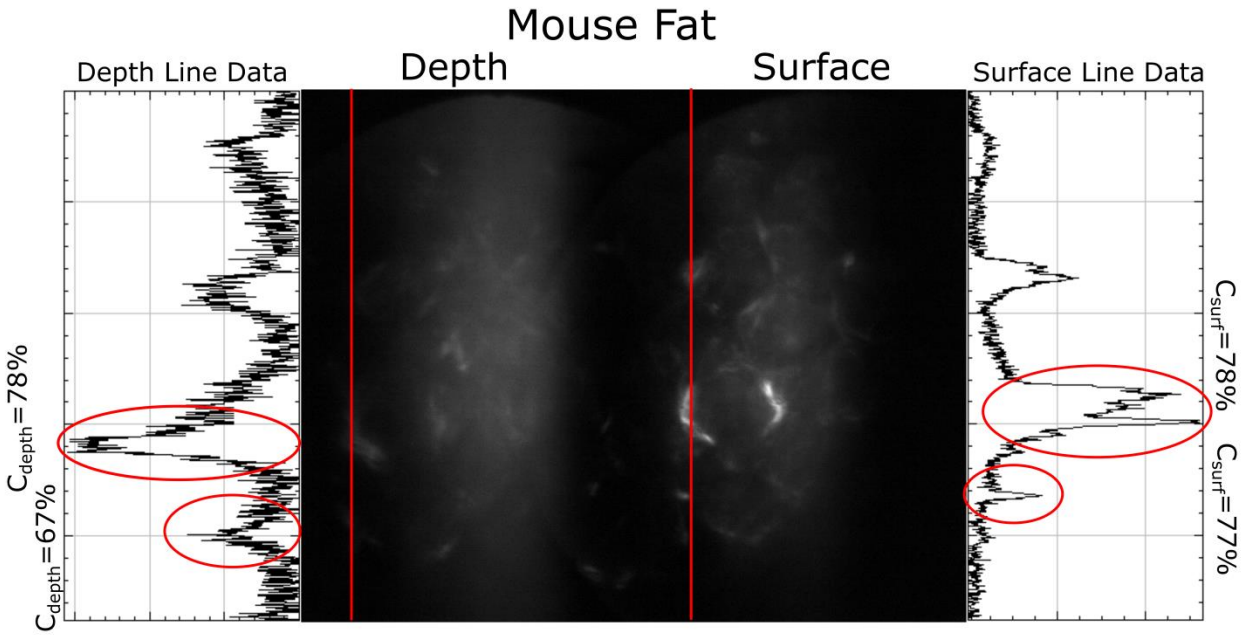

Figure 4.13: Contrast calculation for a y-axis slice in a mouse fat image. The selected peaks demonstrate contrast values between 67% and 78%.

The next sets of images evaluated were from biopsied mouse lung and intestine samples. From these images we were able to see surface structure which was not present in any of the imaging experiments performed for the reflectance endoscope system. The surface channel shows tissue structure in some detail while the depth channel shows features which are significantly reduced. It should be recalled that the depth channel is imaging at a 100 µm depth which is twice that of the reflectance mode system. Significant scatter occurs and is not filtered by the volume hologram which is still operating in the degenerate mode.

Figure 4.14 shows the lung sample imaged at two locations on the sample. The two regions show bright area encircled by darker edges. This is the reverse pattern from that seen in the fat cells, where the cell walls were bright and the inner structures were dark. The organization of the features seen in the image are not as clear as that seen in the onion or fat images, there is more randomness in the features and more reflected light from the central areas of the cells.

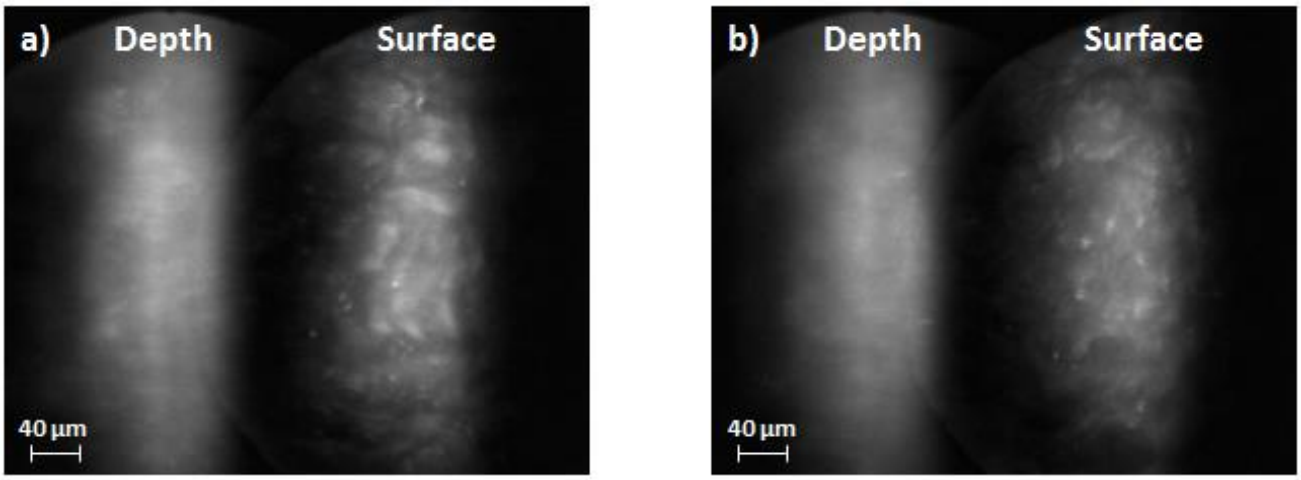

Figure 4.14: Mouse lung imaging using the wavelength coded VHI endoscope. Sub-images a) and b) correspond to different areas on the sample. The surface images begin to show surface structure while the depth images contain more background and backscatter causing the fine details to be washed out.

Figure 4.15 shows the images obtained from two different regions of a mouse intestine sample. A dark cell wall pattern is again seen in this sample. The structures here are less organized in nature with little overlap compared to the fat samples and have lower reflectance from within the center of the cell which is reverse of what was seen in the lung images.

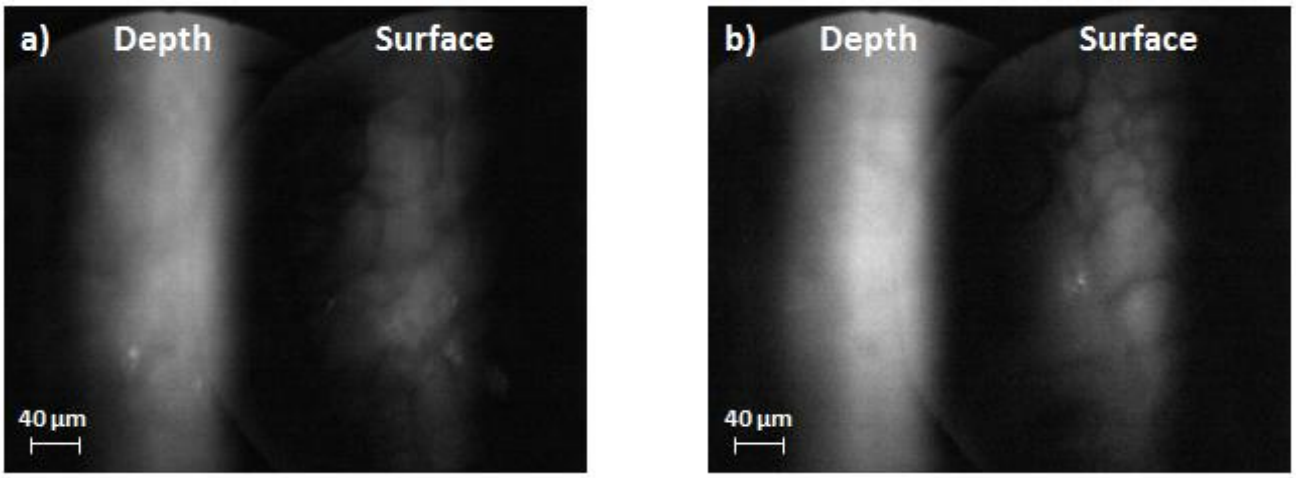

Figure 4.15: Mouse intestine imaging using the wavelength coded VHI endoscope. Sub-images a) and b) correspond to different areas on the sample. The surface images begin to show surface structure, with the cell features having dark edges. The depth images contain more background and backscatter causing the fine details to be washed out.

The contrast measurements of the mouse lung and intestine samples are shown in Figure 4.16 and Figure 4.17 below. The surface slice data in both cases show peak values which exceed the noise, giving contrast values of 20% for the lung and 35% for the intestine images. The depth images, though providing contrast values of 19-20%, cannot be taken as significant due to the noise levels in the images. There are many variations from pixel to pixel in the region which leads to errors when calculating the contrast value. Nonetheless, some features can be observed visually.

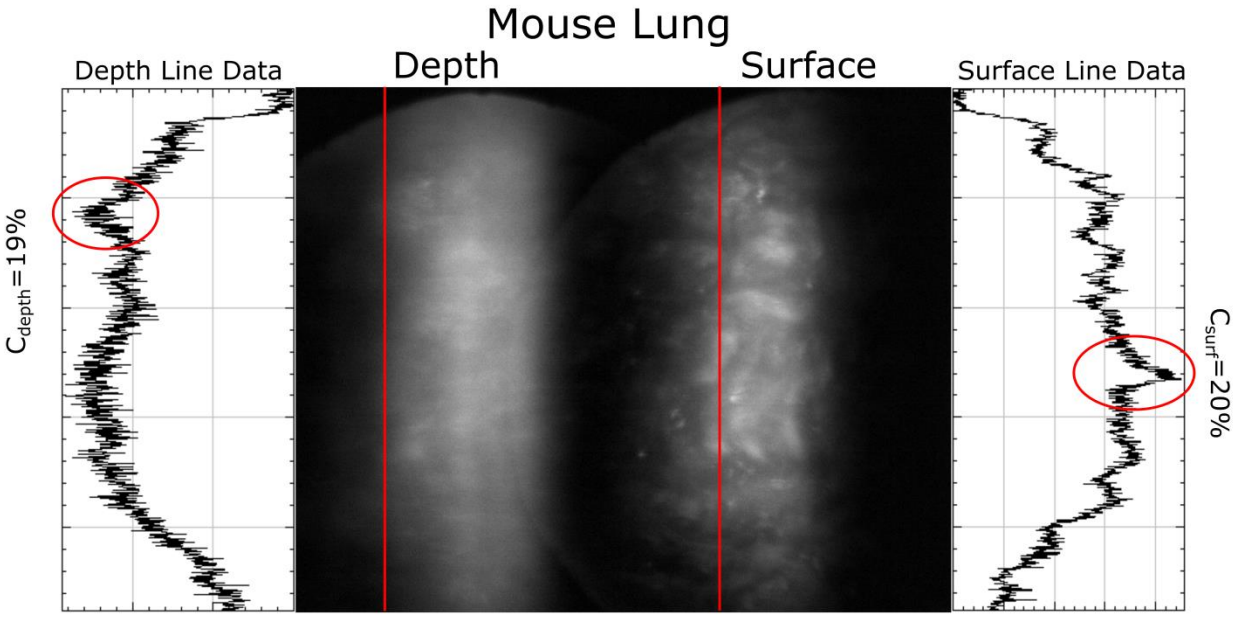

Figure 4.16: Contrast calculation for the surface and depth channel of a mouse lung image. The contrast of 20% in the surface corresponds to a peak near the center of the image (indicated with the oval in the figure). The contrast of 19% in the depth image is from a peak location seen near the top of the image (indicated by an oval in the figure) which may be affected by noise in the image caused by large jumps in the values from pixel to pixel.

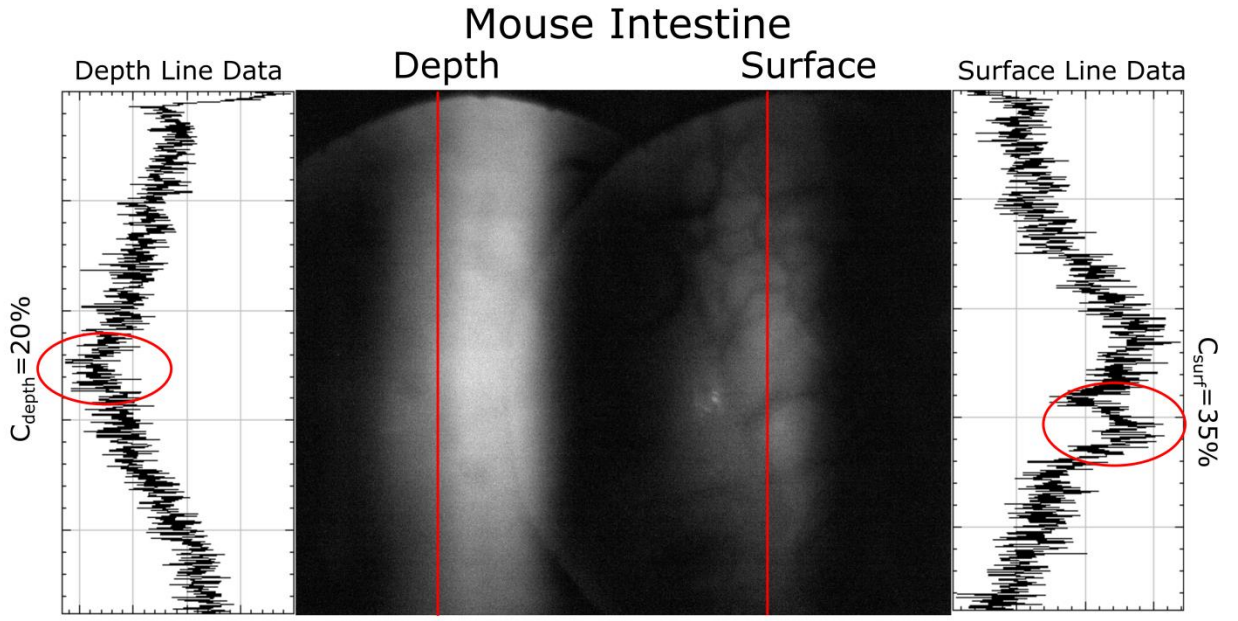

Figure 4.17: Contrast calculation for the surface and depth channel of a mouse intestine image. The contrast of 35% in the surface corresponds to a peak near the center of the image (indicated with the oval in the figure), noise in the image may result in a larger than expected contrast due to large pixel to pixel variations. The contrast of 20% in the depth image is from a peak location seen near the center of the image (indicated by an oval in the figure) which may also be affected by noise in the image.

4.5.4 System Limitations

Although improvements in the system could be seen in resolution and ability to image more tissue types, there are still some limitations on the system which need to be addressed for the VHI endoscope. The main limitation is the depth imaging channel contrast. Hologram Bragg degeneracy and tissue scatter properties are the major contributors to the reduced depth channel contrast.

4.6 Summary

In this chapter, a wavelength coded endoscope using axial chromatic aberration to determine imaging depth was described. The endoscope used in this test was the same endoscope used in the reflectance endoscope system. However instead of using a single 20 nm FWHM source, the wavelength coded system utilizes two 20 nm FWHM sources with peaks separated by 70 nm. The separate sources allowed a longer wavelength to be used for the depth channel and individual power adjustments for surface and depth. This provides significant improvement to the two image channels compared to the reflectance mode system.

The system used a volume holographic element designed with two multiplexed planar holograms for each source. This simplifies the hologram and eliminates the aberration resulting from using different construction and reconstruction sources with curved grating holograms. The images from the system show that each channel is capable of imaging 3.10 μm/lp targets, an improvement from reflectance VHI system.

This system also showed an improved imaging contrast, compared to the standard reflectance endoscope, when imaging lung and intestine samples. The images collected by the

wavelength coded system showed surface structures of these two sample types, with the cell walls appearing as dark regions and the central cell material being bright. These types of tissue had previously showed little to no feature recognition in the standard reflectance endoscope system. The depth channel for the WC-VHI system was sampled at twice the depth of the reflectance VHI endoscope. As a result, the depth channel had more scattering effects which reduced the amount of usable information in the image. The increased background levels lowered the ability to quantify the contrast since the pixel to pixel values varied so quickly.

The surface imaging characteristics provide promising results and bring forward some interesting imaging behavior for the depth images. Additional work to correct the hologram Bragg degeneracy and overlap of wavelengths on the sample may provide improved depth imaging. These are discussed in Chapter 5.

Chapter 5
Discussion

5.1 Summary of Results

The previous chapters outlined the characteristics of a reflection VHI endoscope and a wavelength coded VHI endoscope. In this chapter the performance differences between the two systems are compared using different objects and summarized.

5.1.1 Comparison of Camera Settings

The reflectance VHI system is able to be operated with a camera exposure time of 5 ms for the collection of the bar target images and 15 ms to 30 ms when imaging soft tissue samples. The wavelength coded VHI system required 10 ms exposure time for the bar target images and 60 ms exposure for the soft tissue samples. This difference in the exposure time is due to the illumination configurations for the two systems. The reflectance VHI endoscope LED is able to be in close contact with the fiber connection into the handle, thus having more power delivered to the sample. The wavelength coded VHI system required two lenses to reimage the source through a beam splitter and into the fiber. This method created a light loss on the order of 90% in the wavelength coded system since less light is able to be collected and the pellicle beam splitter coating is designed for a wavelength of 635nm. The power at the object is measured with a power meter, while the power at the microscope objective (MO) is calculated based on the endoscope reflectance values. The power values are included in

Table 5.1.

5.1.2 Comparison of Image Resolution

The reflectance VHI endoscope system was designed to operate at 660 nm with a multiplexed holographic element acting as a wavefront filter for curved wavefronts. The recorded hologram provided a depth separation of 50 µm. The wavelength coded VHI endoscope system was designed to operate at 660 nm and 730 nm with a multiplexed holographic element acting as a wavefront filter for planar wavefronts. The change in the hologram recording was made possible by the axial chromatic dispersion of the endoscope probe. The separation of focal points for the two wavelengths due to axial chromatic aberration is 100 µm.

The resolution of the reflectance VHI endoscope was evaluated using a USAF resolution chart and found to be 2.2 µm. The wavelength coded VHI endoscope was able to resolve 1.55 µm line features for both wavelengths. In terms of line pair per mm (lp/mm) this relates to a change from 228.1 lp/mm for the reflectance system to 322.5 lp/mm for the wavelength coded system. The increased resolution ability is due to the reduction in aberrations caused by the hologram. The reflectance VHI system utilized curved holographic gratings adding more aberration to the system than the wavelength coded VHI planar holographic gratings.

Table 5.1 contains a summary of system design parameters for the two systems.

Table 5.1: Summary of Key Parameters of both Endoscope Systems

	Reflectance Endoscope	**Wavelength Coded Endoscope**
Wavelength (λ)	660 nm	660 nm and 730 nm
Resolution	228.1 lp/mm	322.5 lp/mm
FOV	394 µm x 246 µm	394 µm x 246 µm
Power on Object	1 mW @ 660 nm	0.14 mW @ 660 nm, 0.1 mW @ 730 nm
Power at MO	1 µW @ 660 nm	0.14 µW @ 660 nm, 0.1 µW @ 730 nm
Imaging Depth (ΔZ)	50 µm	100 µm

5.1.3 Tissue Phantom Image Comparison

A comparison of imaging performance of both systems, using the PVA substrate with embedded polystyrene spheres, indicated the capability of the endoscope systems to image through scattering media. In Figure 5.1, the depth channel of both endoscopes shows a higher level of background and scattering. The depth separation is 50 µm for the reflectance system and 100 µm for the wavelength coded system. The reflectance VHI system shows a small amount of change between the beads displayed in the surface and depth channels. The wavelength coded system is able to show more detail and differences in beads in the each channel.

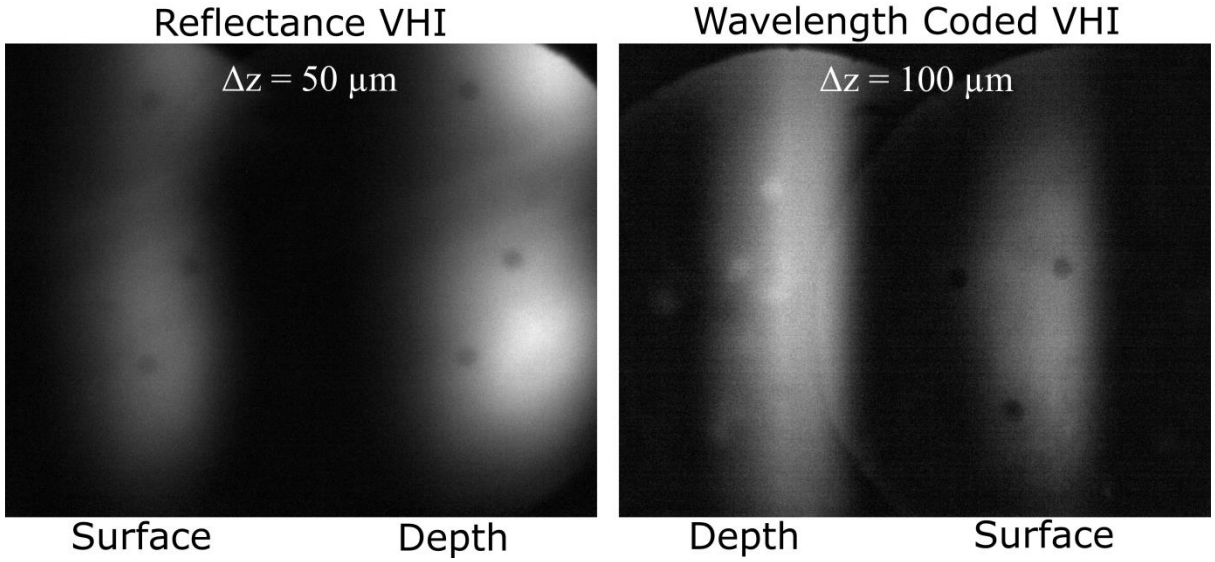

Figure 5.1: Comparison of the images obtained for bead phantoms using the Reflectance VHI and the Wavelength Coded VHI systems

As discussed in the Chapter 3, the reflectance VHI endoscope system did not perform well with a depth separation of 50 µm. The 15 µm diameter polystyrene spheres are non-uniformly placed in the PVA substrate and are not easy to distinguish with the 50 µm depth separation. This has a consequence when viewing biological cells that have a diameter of approximately 20 µm and indicates that a practical depth separation should be more than two cell

diameters to clearly distinguish features. The increased depth separation of the wavelength coded system provides improved surface vs depth detail since the depth separation is 100 μm.

5.1.4 Soft Tissue Image Comparison

To further compare the two systems, a side-by-side comparison of onion skin images are provided in Figure 5.2. The wavelength coded VHI system shows an overall larger illuminated area in the FOV as compared to the reflectance VHI system which may be caused by the curved nature of the hologram used in the reflectance VHI system. The reflectance system also does not show any significant detail in the surface channel for these images. The surface channel in the reflectance VHI has a 42% efficiency, which can be seen in the intensity variation between the surface and depth channels. This can be corrected for by changing the recording parameters to improve the hologram diffraction efficiency for the surface channel to further balance the illumination. However, the wavelength coded VHI system appears to have similar surface and depth intensity. The WC-VHI is able to show well defined cell walls in the surface channel while the depth image starts to reveal some structure within the cells which are not present in the surface image.

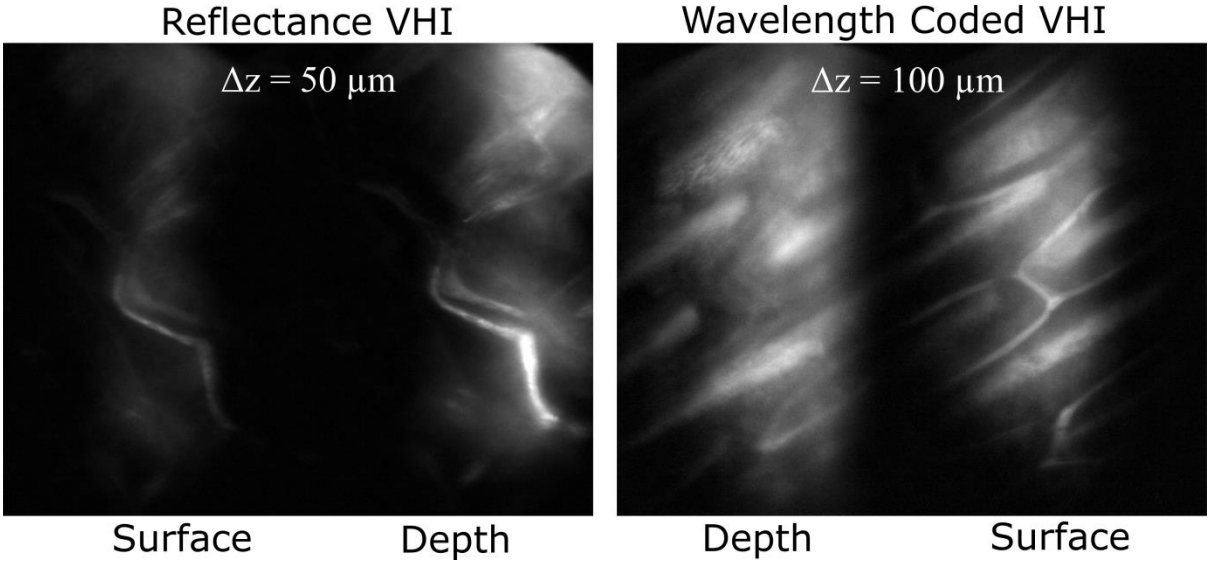

Figure 5.2: Comparison of the images obtained for onion skin using the Reflectance VHI and the Wavelength Coded VHI systems.

5.2 Further Improvements

The main problem in both the reflectance and wavelength coded systems is that the volume hologram is operating with degenerate Bragg selectivity. Different wavelengths illuminate all spatial locations so that multiple or degenerate Bragg matching conditions exist. Without truly separating wavelengths the background light from other depths will pass through the system and degrade the contrast. In addition, using common path illumination results in weak reflections from each optical surface that are comparable to the signal levels even when AR coatings are used on the optics. In the following sections several methods of improving image contrast and rejecting the background levels are discussed.

5.2.1 Structured Illumination

The Bragg degeneracy can be removed in two ways:

1. Use a dispersive grating to spatially separate the wavelengths from a broadband source across the object [14,15]

2. Use a Swept Source Laser and a grating in the illumination path

The first method does not require scanning but has lower power at each spatial location across the object. The optical set-up would be similar to those shown in Figure 2.6 for external illumination or Figure 2.7 and Figure 2.8 for common-path illumination. The light source could be an LED or another extended source. The chromatic aberration behavior of the endoscope probe may lead to unwanted image shifts for this configuration.

The second method requires scanning but has greater power at the object. The illumination for this configuration would be similar to that shown in Figure 2.6 for external illumination or Figure 2.8 for common-path illumination with the extended source being substituted in by a Swept Source Laser. Again, the current design of the endoscope probe may lead to unwanted chromatic aberration effects.

5.2.2 Fluorescence Imaging

Many of the currently used ovarian cancer imaging techniques, such as OCT and Confocal microscopy, use fluorescent imaging methods. Fluorescent imaging is a process of using one wavelength in the illumination path to excite a dye or stain which then emits light at a different wavelength for imaging. This is beneficial in common-path illumination systems since a filter can be used to eliminate the excitation wavelength from reaching the camera, thus reducing unwanted signal in the image.

Fluorescence imaging was performed in the benchtop version of the reflectance endoscope system; however it was not applied to the endoscope system. The reason for this is the availability of clinically approved dyes and stains with an excitation wavelength near 660 nm.

Modifications to the reflectance VHI and wavelength coded VHI in terms of illumination wavelengths used, may provide a usable wavelength range for the approved dyes. However, even if this change in illumination wavelength was able to be used for fluorescence imaging, more design work will be needed in order to improve the depth imaging as many of the fluorescent markers work best for the surface layers of the tissue. This can be improved through the use of intravenous application of the dye.

The main adaptation for the system would be a high pass filter to block the excitation wavelength. Potential dyes for imaging are provided in Table 5.2, however not all are currently approved for in-vivo human studies. A schematic of the updated system is shown in Figure 5.3, where a longpass filter is placed between the hologram and the camera lens.

Table 5.2: Three possible fluorescent dyes with the accompanying excitation and emission wavelengths

Dye	Excitation	Emission	Ref.
Fluorescein Sodium	494 nm	521 nm	10,59
Cy5.5	675 nm	694 nm	60
Acridine Orange	502 nm (DNA) 460 nm (RNA)	525 nm (DNA) 650 nm (RNA)	10

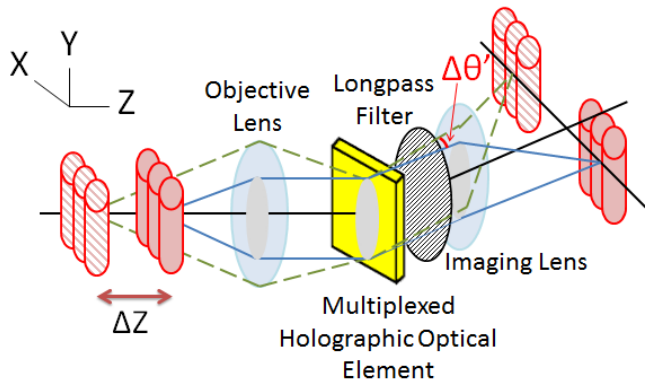

Figure 5.3: Schematic of a VHI system for fluorescence imaging with a longpass filter to block the excitation wavelength

A recent publication by Y. Lv et. al. presented a multispectral fluorescence imaging technique utilizing volume holographic gratings[18]. This system used a multiplexed, 4 channel, volume holographic element corresponding to the wavelengths of 620 nm, 590 nm, 530 nm, and

488 nm. The emission wavelength is narrowband 480 nm source and a 500 nm longpass filter is used to block the source for fluorescence imaging. The schematic of the system is provided in Figure 5.4.

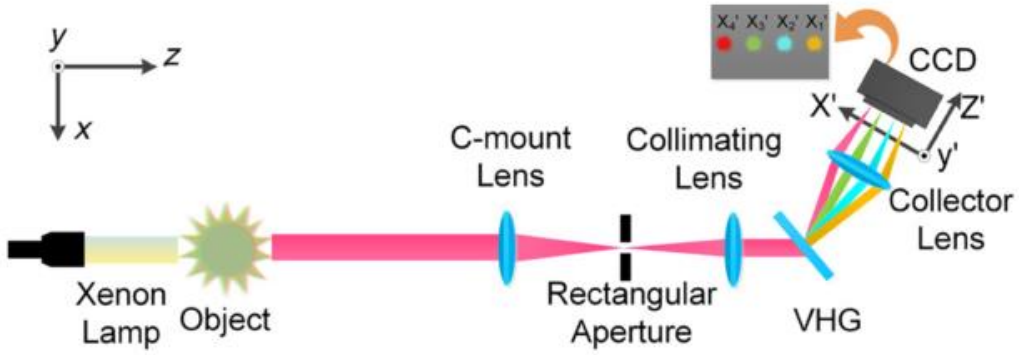

Figure 5.4: The schematic of the multispectral fluorescence imaging VHI system as provided by Y. Lv et. al. [18]

The sample for this test was an anesthetized mouse with two subcutaneously embedded fluorescent beads. The results from this paper showed the potential for VHI systems to be used for multispectral fluorescence imaging. This paper was used as a benchtop model and required the fluorescent markers to be placed near the surface the mouse epidermis. There is a potential to modify this system into an endoscopic form to further the development and imaging performance of the VHI endoscope systems.

5.2.3 Contrast Enhancement of Soft Tissues Using Acetic Acid and Citric Acid

The last of the improvement methods suggested is a test of non-fluorescence dyes or stains to improve image contrast. Acetic acid has previously been used as a contrast enhancement method in optical imaging and spectroscopy systems[61,62]. These previous methods have utilized 3% and 6% acetic acid solutions for both confocal and OCT systems for evaluation of contrast changes. Since acetic acid acts as a dehydrating fluid a change in the amount of light reflected from the

tissue surface cells occurs. This section proposes the use of acetic acid and citric acid for ex-vivo evaluation of mouse fat, lung, and intestine to compare to the soft tissue imaging discussed 4.5.

Procedure Details:

1. Before collecting of tissue samples, verify the system alignment and illumination conditions.
2. Prepare each syringe by filling with 2 mL of the appropriate acid type. The syringe will allow for easy application during the test.
3. Obtain two samples of each tissue specimen to be imaged (i.e. fat, lung, intestine). Samples should be stored in saline and kept on ice. Imaging should take place during the first hour after collection.
4. Image first the fat sample. This sample is chosen first since this sample typically has a high rate of success.
5. After imaging for this sample, apply a small amount of acetic acids to the sample and allow the sample to sit for 5 minutes.
6. During the down time, image the second fat sample without acid. After imaging apply a small amount of citric acid and allow the sample to sit for 5 minutes.
7. Re-image the sample treated with acetic acid.
8. Re-image the sample treated with citric acid.
9. Repeat steps 4-8 for the other tissue types.

The method described above will test if acetic acid and citric acid sample treatment can improve image contrast. Although this method was performed on two samples, the results of the imaging have not provided enough data to confirm the hypothesis. Continued imaging tests are required to fully assess the use acetic acid and citric acid for contrast enhancement. Based on the

prior studies of acetic acid in confocal and OCT systems[61,62] and the amount of scattering seen in the WC-VHI depth imaging it is predicted that this process will improve the images for the surface channel; however the tissue scattering and source bandwidth may still cause issues for the depth channel.

Chapter 6
Conclusions

The aim of this research was to miniaturize benchtop volume holographic imaging systems into devices capable for endoscopic use. Specific goals for the endoscope design include:

1) Design and fabricate a handheld system capable of use in a standard operating room. This specification has requirements on system weight, diameter of the endoscope section, and the ability to be surgically sterilized.

2) A system capable of imaging with lateral resolution ≤ 2 μm corresponding to sub-cellular features.

3) Simultaneously image both surface and subsurface (multiple cell depths) features in biological tissue samples with sufficient contrast and resolution to distinguish changes indicative of early stage cancer.

The final version of the handheld system met the weight, diameter and sterilization requirements. The system was portable and light weight such that a clinical physician was able to use and guide the probe to the imaging site during a surgical procedure. The endoscope probe has a diameter of 3.8 mm, which easily fits into the 5 mm trocar used during the clinical procedure. Lastly, the system was certified by the hospital clinical engineering staff for meeting power output guidelines and sterilization compatibility with hydrogen peroxide vapor and ethyl alcohol processes.

During imaging evaluation of high contrast bar targets the reflectance and wavelength coded systems performed well. Although the reflectance VHI system did not meet the 2 μm

feature imaging goal, the system was able to resolve 2.2 μm features (228.1 lp/mm) which is relatively close to the design specification. The wavelength coded VHI system is able to image 1.55 μm features (322.5 lp/mm). The improvement in the resolution of the wavelength coded system is attributed to the planar grating hologram fabrication and control of the separate sources used in the illumination system. The reflectance VHI system uses holograms with curved fringes across the aperture. Image aberration results in this case since the holograms were formed and reconstructed at different wavelengths. In addition, the reflectance VHI system uses the same 660 nm source for both the surface and the depth channels which leads to higher background levels and hologram crosstalk. The wavelength coded VHI uses two planar gratings which can be formed and reconstructed at different wavelengths and not induce image aberrations. The two planar gratings in the WC-VHI system are designed to operate at two separate wavelengths separated by 70 nm. This illumination separation eliminated channel crosstalk through the Bragg selectivity of the volume holograms.

When imaging soft target samples, both systems were able to image onion skin and fat tissue which have relatively high index of refraction changes that lead to higher contrast features. When looking at lower contrast samples such, intestine and lung however, the reflectance VHI system was not able to provide enough contrast to distinguish features. The wavelength coded VHI was however able to provide enough detail in the surface channel for the intestine and lung samples types. The depth channel in the wavelength coded system suffered from high background levels which washed out any image features which may have been present. It should be noted however that the WC-VHI depth channel was sampling at twice the depth of the reflectance VHI endoscope. The greater depth was dictated by the axial chromatic dispersion of

the GRIN probe. If the sample depth for the WC-VHI was reduced, the background level would also be reduced.

Overall, reflectance and wavelength coded VHI systems have shown the feasibility of endoscopic versions that can function in surgical operating settings. Future work to reject the background noise and increase the contrast of low contrast samples will improve depth imaging. The primary cause for the high background level is degeneracy in the Bragg matching condition of the volume holograms that results from the randomized spatial distribution of wavelengths in the tissue sample. This can be achieved using structured illumination and will allow the VHI method to image similar to slit-scanning confocal systems but at a much lower cost. This in turn will lead to greater availability of imaging tools for the detection of cancer.

APPENDICES

A. Publications

A.1 Reflectance VHI Endoscope Journal Paper - Published

The manuscript titled "Volume holographic imaging endoscopic design and construction techniques," was accepted for publication in the Journal of Biomedical Optics in May 2017.

- Howlett, I.D., Han, W., Gordon, M., Rice, P., Barton, J.K., and Kostuk, R.K., "Volume holographic imaging endoscopic design and construction techniques," Journal of Biomedical Optics 22(5), (2017).

A.2 Wavelength Coded VHI Endoscope Journal Paper - Submitted

The manuscript titled "Wavelength coded volume holographic imaging endoscope for multi-depth imaging," was submitted for review in the Journal of Biomedical Optics in July 2017:

- Howlett, I.D., Han, W., Gordon, M., Rice, P., Barton, J.K., and Kostuk, R.K., "Wavelength coded volume holographic imaging endoscope for multi-depth imaging," Journal of Biomedical Optics (Submitted July 2017).

B. MATLAB Code for Gaussian Beam Modeling of the Triplet GRIN Design

Discussed in Chapter 3.2.2, the design and modeling was partially done through the use of a Gaussian beam modeling MATLAB code. The original code, useful to design fiber based OCT systems, is modified to trace rays through the entire GRIN reflectance endoscope. The method allows for the Gaussian beam parameters to be propagated through the use of ABDC matrices. The functions called, as written by Tyler Tate, were not modified and can be found in the cited dissertation work in Chapter 3.

```
%% ABCD matrix Gaussian beam propagation
% Based on design from Handbook of Coherent-Domain Optical Methods
% Needle Probes in Optical Coherence Tomography
% Chapter 25.3.4 Optical Design of OCT Needle Probes, R. A. McLaughlin et al

% Base code provided by Dr. Tyler Tate to propagate Gaussian beams through
% optical systems. The code calculates the q-factor after each element and
% plots the Gaussian beam waist through the system.

% Dr. Tate's code: 'ABCD_*.m' functions to generate ABCD matrices for the
% indicated surface types. The 'BeamWaist.m' function generates the beam
% waist through z given the q factor for a give space.
%
% This code is for the case of a 3 GRIN probe with two optical windows
% All lengths are microns. Distances must be integers
%
% Last updated: 01/20/2017
% Author: Isela D. Howlett, based on code from Tyler Tate
clear all;
close all;
clc
%% Set Wavelength

lambda = 0.66; %microns

%% Set number of mediums light propagates through including SM fiber

num_spaces = 8; %number of spaces for calculation
% This code uses 8: beam waist, water, window, GRIN lens, Grin Rod,
% Grin lens, window, air.

%% Code initializes various vectors for the creation of the matrices

num_mats = num_spaces*2-1; %num ABCD matrices (spaces plus interfaces)
M = zeros(2,2,num_mats); %init 3D vector of ABCD mats.
n = ones(num_spaces,1); %init index vector
d = zeros(num_spaces,1); %init dist traveled vector
```

```
w0 = ones(num_spaces,1); %init beam waist vector
z_loc = zeros(num_spaces,1); %init vector of distance from current pos to beam waste
z_shift = zeros(num_spaces,1); %init vector to track beam waste axis shifts
q = zeros(num_spaces,1); %init vector of q factor after each mat
space_name = cell(num_spaces,1); %init vector of space names

%% Define each propagation space

% SPACE 1: Where the beam starts.
% This takes into account the NA of the probe to calculate a beam waist

s = 1; %current space number
space_name(s) = cellstr('Source'); %set name of space, used in plotting
z_loc(s) = 0; %beam waist located at z=0
z_shift(s) = z_loc(s); %set shift for Gaussian equations
system_dia = 2.7*1000; %mm to microns, set based on largest diameter
w0(s) = 0.5105; %beam waist exiting fiber, calculated with NA & Wavelength
% from http://www.marcuswinter.de/archives/1685
MFD = w0(s)*2; % sets a Mode Field Diameter based on the Beam Waist, this
% parameter is from the original OCT values for a fiber.

n(s) = 1.333; %index of material 1 for air, n=1.333 for water
d(s) = 0; %Length of propagation. This should be zero for this application

%Calculates the q factor exiting the fiber using the above values
q(s) = 1i*n(s)*pi*w0(s)^2/lambda; %q factor exiting fiber

% SPACE 2: Propagation from Beam waist to Distal Window
s=2;
space_name(s) = cellstr('Water'); %Name used for Plotting
n(s) = 1.333; % n=1.333 for water
d(s) = 0; %physical length in microns [0 = surface, 100 = depth]

%SPACE 3: Propagation through Distal Window
s=3;
space_name(s) = cellstr('Window D');
n(s) = 1.517; % n = 1.517 for N-BK7
d(s) = 0.800*1000; %physical length in microns; converts 0.8 mm to microns

%SPACE 4: Propagation through Imaging Lens
%Grin Lens - Distal
s=4;
space_name(s) = cellstr('GRIN Lens D'); %Name used for Plotting
ap_GRIN(s) = 2.700*1000; %clear aperture diameter of GRIN (2.7 mm to um)
n(s) = 1.643; %reference index for GRIN - center index
% Note that pitch p=2*pi/g. For every multiple of p,  the same ending
% parameters result, but image flips. (p, 2p, 3p, 4p, etc)
g(s) = .222/1000; %GRIN profile in reciprocal microns
d(s) = 5.780*1000; %physical length in microns, converts 5.780 mm to um

%SPACE 5: Propagation through GRIN Rod
```

```
%GRIN Rod parameters
s = 5;
space_name(s) = cellstr('GRIN Rod'); % Used for Plotting
ap_GRIN(s) = 2.700*1000; %clear aperture diameter of GRIN (2.7 mm to um)
n(s) = 1.610; %reference index for GRIN - center index
% Note that pitch p=2*pi/g. For every multiple of p,  the same ending
% parameters result, but image flips. (p, 2p, 3p, 4p, etc)
g(s) = .0446/1000; %GRIN profile in reciprocal microns
d(s) = 281.4*1000; %physical length in microns, converts 281.4 mm to um

%SPACE 6: Propagation through Coupling Lens
%Grin Lens - Proximal
s=6;
space_name(s) = cellstr('GRIN Lens P'); %Name used for Plotting
ap_GRIN(s) = 2.700*1000; %clear aperture diameter of GRIN (2.7 mm to um)
n(s) = 1.643; %reference index for GRIN - center index
% Note that pitch p=2*pi/g. For every multiple of p,  the same ending
% parameters result, but image flips. (p, 2p, 3p, 4p, etc)
g(s) = .222/1000; %GRIN profile in reciprocal microns
d(s) = 5.720*1000; %physical length in microns, converts 5.720 mm to um

%SPACE 7: Propagation through Proximal Window
s=7;
space_name(s) = cellstr('Window P'); % Name used for Plotting
n(s) = 1.517; % n = 1.517 for N-BK7
d(s) = 0.800*1000; %physical length in microns; converts 0.8 mm to microns

%SPACE 8: Propagation through air to Microscope Objective
s=8;
space_name(s) = cellstr('Air P'); %Name used in plotting
n(s) = 1; %n = 1 for air
d(s) = 3.6*1000; %physical length to plot prop to objective, (mm to um)

%% Define ABCD matrices
% This code will generate the ABCD matrices for each of the spaces and
% interfaces.

% you will have (s*2)-1 Matrices to account for each interface
M(:,:,1) = ABCD_Prop(d(1)); %prop in space 1. ID mat is d(1)=0
M(:,:,2) = ABCD_FlatRef(n(1),n(2)); %Interface 1 (source to air)
M(:,:,3) = ABCD_Prop(d(2)); %prop in space 2
M(:,:,4) = ABCD_FlatRef(n(2),n(3)); %Interface 2 (air to window)
M(:,:,5) = ABCD_Prop(d(3)); %prop through distal window
M(:,:,6) = ABCD_FlatRef(n(3),n(4)); %Interface 3 (Window to GRIN Lens)
M(:,:,7) = ABCD_GRIN(g(4),d(4)); %prop through distal GRIN
M(:,:,8) = ABCD_FlatRef(n(4),n(5)); %Interface 4 (GRIN Lens to GRIN Rod)
M(:,:,9) = ABCD_GRIN(g(5),d(5)); %prop through GRIN Rod
M(:,:,10) = ABCD_FlatRef(n(5),n(6)); %Interface 5 (GRIN Rod to GRIN Lens)
M(:,:,11) = ABCD_GRIN(g(6),d(6)); %prop through Proximal GRIN
M(:,:,12) = ABCD_FlatRef(n(6),n(7)); %Interface 6 (GRIN LENS to Window)
M(:,:,13) = ABCD_Prop(d(7)); %prop through window
M(:,:,14) = ABCD_FlatRef(n(7),n(8)); %Interface 7 (Window to Air)
```

```
%M(:,:,15) = ABCD_Prop(d(8)); %propagation to MO

% Tyler's Note: the final air propagation matrix isn't actually used to
% plot the beam waist as the final interface gives the q-factor with
% sufficient information to plot the waist any distance beyond the final
% interface. It is included here for completeness.

%% Transfer Gaussian beam through each ABCD matrix
% This code starts the matrix transfer calculation through the system.
% GRIN lenses will have an additional trace later which shows the beam
% changing for the gradient index.

% Defines the distance vector that tracks total traveled distance of beam
d_cum = zeros(length(d),1);
d_cum(1) = d(1);
for k=2:length(d_cum)
    d_cum(k) = d_cum(k-1)+d(k);
end

% Loop does a propagation and the following interface on each iteration
for k=1:num_spaces-1
    in = [q(k);1]; %input
    Msys = M(:,:,2*k)*M(:,:,2*k-1); %ABCD mat for prop then interface
    out = Msys*in; %output
    q(k+1)= out(1)/out(2); %generate new normalized q factor
    z_loc(k+1) = real(q(k+1)); %beam waist location is real part of q factor
    z_shift(k+1) = d_cum(k)-z_loc(k+1); %track beam waist loc relative to each space
    w0(k+1) = sqrt(imag(q(k+1))*lambda/(n(k+1)*pi)); %calc beam waist for each space
end

%% Generate plot of beam waist size through system
% This section of code plots the beam for each of the elements.
% Tyler's note: q-factor gives beam waist and location. The Gaussian
% equations are defined such that the beam waist is located at z=0. Z_shift
% is used to shift the output from Gaussian equations to the global
% coordinate system.

% Defines axes for PLOT 1: Source, Water, Window, Grin 1
xmin = -700; %distance left of fiber face to plot for visual clarity
xmax = sum(d(1:4)); % distance to plot right of zero
ymax = system_dia/2; % height of plot limited to GRIN radius
ymin = -ymax; % optical axis is center of plot
z = linspace(z_loc(1),xmax,xmax-z_loc(1)+1); % define z axis (1 sample/um)
h = figure('Position', [20, 200, 750, 450]); %init figure loc and size
set(gcf, 'Color', [1,1,1]) % sets the background of the image to white
axis([xmin xmax ymin ymax]); %set fig axes
hold on %set so figure overlays each of the following plots

% Source
s = 1;
%add vertical line for interface
```

```
line([d_cum(s)+1 d_cum(s)+1], [-ymax ymax],'Color','k');
%add text box for specifications
str = {char(space_name(s)), 'n =', num2str(n(s),'%.4f\n'), 'Spot Dia =', [num2str(MFD,'%.2f') '\mum']};
text((xmin+d(s))/2,ymax*.2,str,'HorizontalAlignment','center','VerticalAlignment','top');

% Water
s = 2;
domain2 = z(d_cum(s-1)+1:d_cum(s)+1); %it exists in this range
%calc beam waist over appropriate domain and z_shift
nc_beam = BeamWaist(domain2-z_shift(s),w0(s),lambda,n(s));
plot(domain2, nc_beam, domain2, -nc_beam, 'LineWidth', 2, 'Color', 'b')
%add vertical line for interface
line([sum(d(1:s)) sum(d(1:s))], [-ymax ymax],'Color','k');

% Window
s = 3;
domain3 = z(d_cum(s-1)+1:d_cum(s)+1); %it exists in this range
%calc beam waist over appropriate domain and z_shift
nc_beam3 = BeamWaist(domain3-z_shift(s),w0(s),lambda,n(s));
plot(domain3, nc_beam3, domain3, -nc_beam3, 'LineWidth', 2, 'Color', 'r')
%add vertical line for interface
line([sum(d(1:s)) sum(d(1:s))], [-ymax ymax],'Color','k');
%add text box for specifications
str = {char(space_name(s)), 'n =', num2str(n(s),'%.4f\n'), 'L =', [num2str(d(s),'%.0f') '\mum']};
text((d_cum(s-1)+d_cum(s))/2,ymax,str,'HorizontalAlignment','center','VerticalAlignment','top');

% GRIN
s = 4;
%add vertical line for interface
line([d_cum(s)+1 d_cum(s)+1], [-ymax ymax],'Color','k');
%add text box for specifications
str = {char(space_name(s)), 'n =', num2str(n(s),'%.4f\n'), 'L =', [num2str(d(s),'%.0f')
'\mum'],'g=',[num2str(g(s)*1000,'%.2f'), '']};
text((d_cum(s-1)+d_cum(s))/2,ymax*.25,str,'HorizontalAlignment','center','VerticalAlignment','top');
%This code creates an additional ABCD prop through GRIN, using short
% intervals to plot the sinusoidal pattern of the GRIN.
int = 15; % interval width between points plotted in GRIN
domain4 = d_cum(s-1):int:d_cum(s); %domain in GRIN
domain4 = domain4(2:end); %Don't want first coordinate as its on boundary
dom_size = length(domain4); %having length of vector is useful
waistheight4 = zeros(dom_size,1); %init vector for waist height inside GRIN
Mtemp = ABCD_GRIN(g(s),int); %This is the prop vector in the GRIN with interval width
z_loc_GRIN = zeros(dom_size,1); %init vector of distance from current pos to beam waist
z_shift_GRIN = zeros(dom_size,1); %init vector to track beam waist axis shifts
w0_GRIN = zeros(dom_size,1); %init vector to track min waist through GRIN
qtemp = q(s); %set initial q factor in GRIN
%loop to calc q factor at each interval location through GRIN
for k=1:dom_size
   in = [qtemp;1]; %input vector
   out = Mtemp*in; %output vector
   qtemp = out(1)/out(2); %generate new normalized q factor
   z_loc_GRIN(k) = real(qtemp); %dist to waist
```

```
    z_shift_GRIN(k) = d_cum(s-1)+k*int-z_loc_GRIN(k); %shift loc to global coordinates
    w0_GRIN(k) = sqrt(imag(qtemp)*lambda/(n(s)*pi)); %waist for current beam shape
    waistheight4(k) = BeamWaist(domain4(k)-z_shift_GRIN(k),w0_GRIN(k),lambda,n(s)); %find waist height at current location
end
%plot results on graph
plot(domain4,waistheight4, ':', 'LineWidth', 2, 'Color', 'b');
plot(domain4,-waistheight4, ':', 'LineWidth', 2, 'Color', 'b');
%plot line representing max beam height in GRIN (clear aperture)
line([d_cum(s-1) d_cum(s)],[ap_GRIN(s)/2 ap_GRIN(s)/2],'Color','k','LineStyle',':');

% Plot labeling and axis ticks
hold off
title('Propagation Through VHI GRIN Optics');
xlabel('Distance in microns');
ylabel('Beam radius in microns');
if d(2) == 0
xticks([xmin sum(d(1:2)) sum(d(1:3)) xmax])
xticklabels([xmin/10^5 sum(d(1:2))/10^5 sum(d(1:3))/10^5 xmax/10^5])
else
    xticks([xmin d(1) sum(d(1:2)) sum(d(1:3)) xmax])
    xticklabels([xmin/10^5 d(1)/10^5 sum(d(1:2))/10^5 sum(d(1:3))/10^5 xmax/10^5])

end
xtickangle(70)

%%
% Define axes for PLOT 2: GRIN Rod
xmin = sum(d(1:4)); %distance left of fiber face to plot for visual clarity
xmax = sum(d(1:5)); %distance to plot right of zero
ymax = system_dia/2; %height of plot limited to SM fiber radius
ymin = -ymax; %optical axis is bottom of plot
z = linspace(z_loc(1),xmax,xmax-z_loc(1)+1); %define z axis (1 sample/micron)
h = figure('Position', [20, 200, 750, 450]); %init figure loc and size
set(gcf, 'Color', [1,1,1]) % sets the background of the image to white
axis([xmin xmax ymin ymax]); %set fig axes
hold on %set so figure overlays each of the following plots

% GRIN ROD
s = 5;
%add vertical line for interface
line([d_cum(s)+1 d_cum(s)+1], [-ymax ymax],'Color','k');
%add text box for specifications
str = {char(space_name(s)), 'n =', num2str(n(s),'%.4f\n'), 'L =', [num2str(d(s),'%.0f') '\mum'],'g=',[num2str(g(s)*1000,'%.2f'), ''']};
text((d_cum(s-1)+d_cum(s))/2+8000,ymax*.25,str,'HorizontalAlignment','center','VerticalAlignment','top');
%This code creates an additional ABCD prop through GRIN, using short
% intervals to plot the sinusoidal pattern of the GRIN.
int = 15; %interval width between points plotted in GRIN
domain5 = d_cum(s-1):int:d_cum(s); %domain in GRIN
domain5 = domain5(2:end); %Don't want first coordinate as its on boundary
dom_size = length(domain5); %having length of vector is useful
```

```
waistheight5 = zeros(dom_size,1); %init vector for waist heigh inside GRIN
Mtemp = ABCD_GRIN(g(s),int); %This is the prop vector in the GRIN with interval width
z_loc_GRIN = zeros(dom_size,1); %init vector of distance from current pos to beam waist
z_shift_GRIN = zeros(dom_size,1); %init vector to track beam waist axis shifts
w0_GRIN = zeros(dom_size,1); %init vector to track min waist through GRIN
qtemp = q(s); %set initial q factor in GRIN
%loop to calc q factor at each interval location through GRIN
for k=1:dom_size
   in = [qtemp;1]; %input vector
   out = Mtemp*in; %output vector
   qtemp = out(1)/out(2); %generate new normalized q factor
   z_loc_GRIN(k) = real(qtemp); %dist to waist
   z_shift_GRIN(k) = d_cum(s-1)+k*int-z_loc_GRIN(k); %shift loc to global coordinates
   w0_GRIN(k) = sqrt(imag(qtemp)*lambda/(n(s)*pi)); %waist for current beam shape
   waistheight5(k) = BeamWaist(domain5(k)-z_shift_GRIN(k),w0_GRIN(k),lambda,n(s)); %find waist height at
current location
end
%plot results on graph
plot(domain5, waistheight5, ':', 'LineWidth', 2, 'Color', 'k');
plot(domain5, -waistheight5,':', 'LineWidth', 2, 'Color', 'k');
%plot line representing max beam height in GRIN (clear aperature)
line([d_cum(s-1) d_cum(s)],[ap_GRIN(s)/2 ap_GRIN(s)/2],'Color','k','LineStyle',':');

% Plot labeling and axis ticks
hold off
title('Propagation Through VHI GRIN Optics');
xlabel('Distance in microns');
ylabel('Beam radius in microns');
xticks([xmin sum(d(1:5))/4 2*sum(d(1:5))/4 3*sum(d(1:5))/4 xmax])
xtickangle(70)

%%
% Define axes for PLOT 2: GRIN Lens, Window, Air
xmin = sum(d(1:5)); %distance left of fiber face to plot for visual clarity
xmax = sum(d(1:8))+700; %distance to plot right of zero
ymax = system_dia/2; %height of plot limited to SM fiber radius
ymin = -ymax; %optical axis is bottom of plot
z = linspace(z_loc(1),xmax,xmax-z_loc(1)+1); %define z axis (1 sample/micron)
h = figure('Position', [20, 200, 750, 450]); %init figure loc and size
set(gcf, 'Color', [1,1,1]) % sets the background of the image to white
axis([xmin xmax ymin ymax]); %set fig axes
hold on %set so figure overlays each of the following plots

% GRIN - Coupling Lens
s = 6;
%add vertical line for interface
line([d_cum(s)+1 d_cum(s)+1], [-ymax ymax],'Color','k');
%add text box for specifications
str = {char(space_name(s)), 'n =', num2str(n(s),'%.4f\n'), 'L =', [num2str(d(s),'%.0f')
'\mum'],'g=',[num2str(g(s)*1000,'%.2f'), "]};
text((d_cum(s-1)+d_cum(s))/2,ymax*.25,str,'HorizontalAlignment','center','VerticalAlignment','top');
%This code creates an additional ABCD prop through GRIN, using short
```

```
% intervals to plot the sinusoidal pattern of the GRIN.
int = 15; %interval width between points plotted in GRIN
domain6 = d_cum(s-1):int:d_cum(s); %domain in GRIN
domain6 = domain6(2:end); %Don't want first coordinate as its on boundary
dom_size = length(domain6); %having length of vector is useful
waistheight6 = zeros(dom_size,1); %init vector for waist height inside GRIN
Mtemp = ABCD_GRIN(g(s),int); %This is the prop vector in the GRIN with interval width
z_loc_GRIN = zeros(dom_size,1); %init vector of distance from current pos to beam waist
z_shift_GRIN = zeros(dom_size,1); %init vector to track beam waist axis shifts
w0_GRIN = zeros(dom_size,1); %init vector to track min waist through GRIN
qtemp = q(s); %set initial q factor in GRIN
%loop to calc q factor at each interval location through GRIN
for k=1:dom_size
    in = [qtemp;1]; %input vector
    out = Mtemp*in; %output vector
    qtemp = out(1)/out(2); %generate new normalized q factor
    z_loc_GRIN(k) = real(qtemp); %dist to waist
    z_shift_GRIN(k) = d_cum(s-1)+k*int-z_loc_GRIN(k); %shift loc to global coordinates
    w0_GRIN(k) = sqrt(imag(qtemp)*lambda/(n(s)*pi)); %waist for current beam shape
    waistheight6(k) = BeamWaist(domain6(k)-z_shift_GRIN(k),w0_GRIN(k),lambda,n(s)); %find waist height at
current location
end
%plot results on graph
plot(domain6, waistheight6,':', 'LineWidth', 2, 'Color', 'b');
plot(domain6, -waistheight6,':', 'LineWidth', 2, 'Color', 'b');
%plot line representing max beam height in GRIN (clear aperture)
line([d_cum(s-1) d_cum(s)],[ap_GRIN(s)/2 ap_GRIN(s)/2],'Color','k','LineStyle',':');

%Window
s = 7;
domain7 = z(d_cum(s-1)+1:d_cum(s)+1); %it exists in this domain
%calc beam waist over appropriate domain and z_shift
nc_beam7 = BeamWaist(domain7-z_shift(s),w0(s),lambda,n(s));
plot(domain7, nc_beam7, domain7, -nc_beam7, 'LineWidth', 2, 'Color', 'r')
%add vertical line for interface
line([d_cum(s)+1 d_cum(s)+1], [-ymax ymax],'Color','k');
%add text box for specifications
str = {char(space_name(s)), 'n =', num2str(n(s),'%.4f\n'), 'L =', [num2str(d(s),'%.0f') '\mum']};
text((d_cum(s-1)+d_cum(s))/2,ymax*-.5,str,'HorizontalAlignment','center','VerticalAlignment','top');

% Air
s = 8;
domain8 = z(d_cum(s-1)+1:d_cum(s)+1);
%calc beam waist over appropriate domain and z_shift
air_beam = BeamWaist(domain8-z_shift(s),w0(s),lambda,n(s));
plot(domain8, air_beam, 'LineWidth', 1, 'Color', 'b')
plot(domain8, -air_beam, 'LineWidth', 1, 'Color', 'b')
w0_loc = d_cum(s-1)+1-z_loc(end);
line([w0_loc w0_loc], [0 w0(s)],'Color','r');
%add Rayleigh range to plot
zr = w0(s)^2*pi*n(s)/lambda;
line([w0_loc-zr w0_loc-zr],[0 sqrt(2)*w0(s)],'Color','g');
```

```
line([w0_loc+zr w0_loc+zr],[0 sqrt(2)*w0(s)],'Color','g');
%add text box for specifications
str = {char(space_name(s)), ['n =' num2str(n(s),'%.4f\n')],...
   ['WD=' num2str(-z_loc(s),'%.0f\n') '\mum'],...
   ['Spot Dia=' num2str(2*w0(s),'%.2f') '\mum'],...
   ['\lambda=',num2str(lambda*1000,'%.0f'),'nm']};
text((d_cum(s-1)+d_cum(s))/2+1000,ymax*.25,str,'HorizontalAlignment','center','VerticalAlignment','top');

%final graph formatting
hold off
title('Propagation Through VHI GRIN Optics');
xlabel('Distance in microns');
ylabel('Beam radius in microns');
xticks([xmin sum(d(1:6)) sum(d(1:7)) xmax])
xtickangle(70)
```

REFERENCES

[1] Adie, S.G., and Boppart, S.A., [Optical Imaging of Cancer] , E. Rosenthal and K. R. Zinn, Eds., Springer New York, New York, NY (2010).

[2] Paddock, S.W., Ed., [Confocal Microscopy] , Springer New York, New York, NY (2014).

[3] Orsinger, G. V, Watson, J.M., Gordon, M., Nymeyer, A.C., de Leon, E.E., Brownlee, J.W., Hatch, K.D., Chambers, S.K., Barton, J.K., et al., "Simultaneous multiplane imaging of human ovarian cancer by volume holographic imaging.," Journal of biomedical optics 19(3), 36020 (2014).

[4] Greivenkamp, J.E., [Field guide to geometrical optics] , SPIE Press (2004).

[5] "ZEISS Microscopy Online Campus | Microscopy Basics | Reflected Light Microscopy," <http://zeiss-campus.magnet.fsu.edu/articles/basics/reflected.html>.

[6] MacAulay, C., Lane, P., and Richards-Kortum, R., "In vivo pathology: microendoscopy as a new endoscopic imaging modality."

[7] Liang, R., [Optical design for biomedical imaging] , Spie, 1000 20th Street, Bellingham, WA 98227-0010 USA (2010).

[8] Knittel, J., Schnieder, L., Buess, G., Messerschmidt, B., and Possner, T., "Endoscope-compatible confocal microscope using a gradient index-lens system," Optics Communications 188, 267–273 (2001).

[9] Sabharwal, Y.S., Rouse, A.R., Donaldson, L., Hopkins, M.F., and Gmitro, A.F., "Slit-scanning confocal microendoscope for high-resolution in vivo imaging.," Applied optics 38(34), 7133–7144 (1999).

[10] Tanbakuchi, A.A., Udovich, J.A., Rouse, A.R., Hatch, K.D., and Gmitro, A.F., "In vivo imaging of ovarian tissue using a novel confocal microlaparoscope.," American journal of obstetrics and gynecology 202(1), 90.e1-9 (2010).

[11] Kogelnik, H., "Coupled wave theory for thick hologram gratings," Bell Syst. Tech. J. 48, 2909–2947 (1969).

[12] Luo, Y., de Leon, E., Castro, J., Lee, J., Barton, J.K., Kostuk, R.K., and Barbastathis, G., "Phase-contrast volume holographic imaging system.," Optics letters 36(7), 1290–2 (2011).

[13] Oh, S.B., Lu, Z.-Q.J., Tsai, J.-C., Chen, H.-H., Barbastathis, G., and Luo, Y., "Phase-coded volume holographic gratings for spatial–spectral imaging filters," Optics Letters 38(4), 477–479 (2013).

[14] Sun, W., and Barbastathis, G., "Rainbow volume holographic imaging.," Optics letters 30(9), 976–8 (2005).

[15] Castro, J.M., Gelsinger-Austin, P.J., Barton, J.K., and Kostuk, R.K., "Confocal-rainbow volume holographic imaging system.," Applied optics 50(10), 1382–8 (2011).

[16] de Leon, E.E., Brownlee, J.W., Gelsinger-Austin, P., and Kostuk, R.K., "Dual-grating

confocal-rainbow volume holographic imaging system designs for high depth resolution.," Applied optics 51(29), 6952–61 (2012).

[17] Luo, Y., Gelsinger-Austin, P.J., Watson, J.M., Barbastathis, G., Barton, J.K., and Kostuk, R.K., "Laser-induced fluorescence imaging of subsurface tissue structures with a volume holographic spatial-spectral imaging system.," Optics letters 33(18), 2098–2100 (2008).

[18] Lv, Y., Zhang, J., Zhang, D., Cai, W., Chen, N., and Luo, J., "In vivo simultaneous multispectral fluorescence imaging with spectral multiplexed volume holographic imaging system," Journal of Biomedical Optics 21(6), 60502 (2016).

[19] Luo, Y., Oh, S.B., and Barbastathis, G., "Wavelength-coded multifocal microscopy.," Optics letters 35(5), 781–783 (2010).

[20] Johnson, S.A., [Chapter 1 - Phase Contrast Microscopy BT - Biomedical Optical Phase Microscopy and Nanoscopy] , Academic Press, Oxford, 3–18 (2013).

[21] "Reflected Light DIC Microscopy | MicroscopyU," <https://www.microscopyu.com/techniques/dic/reflected-light-dic-microscopy>.

[22] Settles, G.S., [Basic Concepts BT - Schlieren and Shadowgraph Techniques: Visualizing Phenomena in Transparent Media] , G. S. Settles, Ed., Springer Berlin Heidelberg, Berlin, Heidelberg, 25–38 (2001).

[23] Goodman, J.W., [Introduction to Fourier Optics] , W. H. Freeman (2005).

[24] Langhorst, M.F., Schaffer, J., and Goetze, B., "Structure brings clarity: Structured illumination microscopy in cell biology," Biotechnology Journal 4(6), 858–865 (2009).

[25] Saxena, M., Eluru, G., and Gorthi, S.S., [Structured illumination microscopy] , in Adv. Opt. Photonics 7, 241–275 (2015).

[26] Liu, W., Psaltis, D., and Barbastathis, G., "Real-time spectral imaging in three spatial dimensions.," Optics letters 27(10), 854–6 (2002).

[27] Barbastathis, G., and Sinha, a, "Information content of volume holographic imaging.," Trends in biotechnology 19(10), 383–92 (2001).

[28] American Cancer Society, "Cancer facts & figures 2016" (2016).

[29] Hariri, L.P., Bonnema, G.T., Schmidt, K., Winkler, A.M., Korde, V., Hatch, K.D., Davis, J.R., Brewer, M. a, and Barton, J.K., "Laparoscopic optical coherence tomography imaging of human ovarian cancer.," Gynecologic oncology 114(2), 188–94 (2009).

[30] Wall, R.A., and Barton, J.K., "Fluorescence-based surface magnifying chromoendoscopy and optical coherence tomography endoscope," Journal of biomedical optics 17(8), (2012).

[31] Latrive, A., and Boccara, A.C., "In vivo and in situ cellular imaging full-field optical coherence tomography with a rigid endoscopic probe.," Biomedical optics express 2(10), 2897–904 (2011).

[32] Cernat, R., Zhang, Y.Y., Bradu, A., Tatla, T., Tadrous, P.J., Li, X.D., and Podoleanu, a.

G., “Ex vivo Optical Coherence Tomography Imaging of Larynx Tissues Using a Forward-viewing Resonant Fiber-optic Scanning Endoscope,” in Proc. SPIE Opt. Coherence Tomogr. Coherence Domain Opt. Methods Biomed. XVI 8213, J. A. Izatt, J. G. Fujimoto, and V. V. Tuchin, Eds., 82133M–82133M–6 (2012).

[33] Gmitro, A.F., Rouse, A.R., and Kano, A., “In vivo fluorescence confocal microendoscopy,” in Proc. IEEE Int. Symp. Biomed. Imaging, 277–280 (2002).

[34] Tanbakuchi, A. a, Rouse, A.R., Udovich, J. a, Hatch, K.D., and Gmitro, A.F., “Clinical confocal microlaparoscope for real-time in vivo optical biopsies.,” Journal of biomedical optics 14(4), 44030 (2014).

[35] Tresserra, F., Grases, P.J., Labastida, R., and Ubeda, A., “Histological Features of the Contralateral Ovary in Patients with Unilateral Ovarian Cancer: A Case Control Study,” Gynecologic Oncology 71(3), 437–441 (1998).

[36] Thorlabs, “Thorlabs, Inc.,” <https://www.thorlabs.com/> (5 December 2012).

[37] Jung, J.C., and Schnitzer, M.J., “Multiphoton endoscopy,” OPTICS LETTERS 2858103880(170), 170–1790 (2003).

[38] Li, X., and Yu, W., “Deep Tissue Microscopic Imaging of the Kidney with a Gradient-Index Lens System.,” Optics communications 281(7), 1833–1840 (2008).

[39] Kim, J.K., Lee, W.M., Kim, P., Choi, M., Jung, K., Kim, S., and Yun, S.H., “Fabrication and operation of GRIN probes for in vivo fluorescence cellular imaging of internal organs in small animals.,” Nature protocols 7(8), 1456–69 (2012).

[40] Rector, D., Rogers, R., and George, J., “A focusing image probe for assessing neural activity in vivo,” Journal of neuroscience methods 91, 135–145 (1999).

[41] GoFoton, “SELFOC® Lenses,” 2017, <https://welcome.gofoton.com/passive-optics/selfoc-lenses/> (1 September 2013).

[42] McLaughlin, R.A, Lorenser, D., and Sampson, D.D., [Needle Probes in Optical Coherence Tomography] , 2nd ed., in Handb. Coherent-Domain Opt. Methods, 2nd ed., V. V. Tuchin, Ed., Springer New York, New York, NY, 1066–1102 (2013).

[43] Tate, T.H., “DUAL MODALITY OPTICAL COHERENCE TOMOGRAPHY AND MULTISPECTRAL FLUORESCENCE IMAGING FOR OVARIAN CANCER DETECTION by A Dissertation Submitted to the Faculty of the COLLEGE OF OPTICAL SCIENCES In Partial Fulfillment of the Requirements For the Degree of DOCTO,” University of Arizona (2017).

[44] “the Gaussian beam (interactive) – Nerd Rage,” <http://www.marcuswinter.de/archives/1685>.

[45] “EPO-TEK ® 301 Technical Data Sheet For Reference Only Spectrally Transparent Epoxy,” 2015, <http://www.epotek.com/site/administrator/components/com_products/assets/files/Style_Uploads/301 Rev IX.pdf> (23 March 2017).

[46] MDDI, “Compatibility of Medical Devices and Materials with Low-Temperature Hydrogen Peroxide Gas Plasma | MDDI Medical Device and Diagnostic Industry News Products and Suppliers,” 1997, <http://www.mddionline.com/article/compatibility-medical-devices-and-materials-low-temperature-hydrogen-peroxide-gas-plasma> (14 September 2014).

[47] Boreman, G.D., [Modulation Transfer Function in Optical and Electro-Optical Systems] , SPIE Press, Bellingham, Washington USA (2001).

[48] Schneider, C. a, Rasband, W.S., and Eliceiri, K.W., “NIH Image to ImageJ: 25 years of image analysis,” Nature Methods 9(7), 671–675 (2012).

[49] Pogue, B.W., and Patterson, M.S., “Review of tissue simulating phantoms for optical spectroscopy, imaging and dosimetry.,” Journal of biomedical optics 11(4), 41102 (2014).

[50] Wang, W., and Li, C., “Measurement of the light absorption and scattering properties of onion skin and flesh at 633 nm,” Postharvest Biology and Technology 86, 494–501 (2013).

[51] Gausman, H., Allen, W., and Escobar, D., “Refractive index of plant cell walls,” Applied Optics 13(1), 109–111 (1974).

[52] Dunn, a K., Smithpeter, C., Welch, a J., and Richards-Kortum, R., “Sources of contrast in confocal reflectance imaging.,” Applied optics 35(19), 3441–3446 (1996).

[53] Smithpeter, C.L., Dunn, a K., Welch, a J., and Richards-Kortum, R., “Penetration depth limits of in vivo confocal reflectance imaging.,” Applied optics 37(13), 2749–2754 (1998).

[54] Wilson, B.C., and Jacques, S.L., “Optical Reflectance and Transmittance of Tissues: Principles and Applications,” IEEE Journal of Quantum Electronics 26(12), 2186–2199 (1990).

[55] Cheong, W.-F., Prahl, S.A., and Welch, A.J., “A Review of the Optical Properties of Biological Tissues,” Ieee Journal of Quantum Electronics 26(12), 2166–2185 (1990).

[56] Luo, Y., Zervantonakis, I.K., Oh, S.B., Kamm, R.D., and Barbastathis, G., “Spectrally resolved multidepth fluorescence imaging,” Journal of Biomedical Optics 16(9), (2011).

[57] Lane, P.M., Elliott, R.P., and MacAulay, C.E., “Confocal Microendoscopy with Chromatic Sectioning,” Spectral Imaging: Instrumentation, Applications, and Analysis II 4959, 23–26 (2003).

[58] Olsovsky, C., Shelton, R., Carrasco-Zevallos, O., Applegate, B.E., and Maitland, K.C., “Chromatic confocal microscopy for multi-depth imaging of epithelial tissue.,” Biomedical optics express 4(5), 732–40 (2013).

[59] Nguyen, N.Q., Biankin, A. V, Leong, R.W.L., Chang, D.K., Cosman, P.H., Delaney, P., Kench, J.G., and Merrett, N.D., “Real time intraoperative confocal laser microscopy-guided surgery.,” Annals of surgery 249(5), 735–7 (2009).

[60] Liu, Z., Miller, S.J., Joshi, B.P., and Wang, T.D., “Wide-field near-infrared fluorescence

endoscope for real-time in vivo imaging," in Proc. SPIE Endosc. Microsc. VII 8217, G. J. Tearney and T. D. Wang, Eds., 82170G–82170G–8 (2012).

[61] Gallwas, J., Stanchi, A., Dannecker, C., Ditsch, N., Mueller, S., Mortensen, U., and Stepp, H., "Effect of acetic acid on optical coherence tomography (OCT) images of cervical epithelium," Lasers in Medical Science 29(6), 1821–1828 (2014).

[62] Agrawal, A., Drezek, R., Pitris, C., Smithpeter, C., Utzinger, U., Brookner, C., and Program, B.E., "Acetic Acid: A Contrast Agent in Optical Imaging and Spectroscopy of Tissue," Reprinted from Biomedical Optical Spectroscopy and Diagnostics,(512), 64–66 (1998).